UNIVERSITY OF SOUTHAMPTON
Faculty of Physical and Applied Sciences
School of Electronics and Computer Science
Nano Research Group

Integration of electrodeposited PdNi alloys with Silicon and Carbon nanotube electronics

by

Ashwin R. Usgaocar

A thesis submitted for the degree of
Doctor of Philosophy

April 2011

Supervisor: Dr. C. H. de Groot

UNIVERSITY OF SOUTHAMPTON

ABSTRACT

FACULTY OF PHYSICAL AND APPLIED SCIENCE
SCHOOL OF ELECTRONICS AND COMPUTER SCIENCE

A thesis submitted for the degree of Doctor of Philosophy

Integration of electrodeposited PdNi alloys with Silicon and Carbon nanotube electronics

by Ashwin Usgaocar

This thesis investigates the electrodeposition of PdNi films with controllable composition and their suitability as electrical contacts in electronic and spintronic devices based on Silicon and Carbon nanotubes (CNTs). The electrodeposition process and characterisation of the electrical and magnetic properties of the deposited PdNi films are described. PdNi films with a wide composition range can be deposited from the same bath by changing the deposition potential. Electrical characterisation shows the formation of high quality PdNi-Si Schottky barriers while magnetic measurements prove the ferromagnetic nature of the PdNi films. Electrodeposited PdNi films are thus shown to be suitable contacts for electronic and spintronic devices.

Hydrogen sensors comprising back to back electrodeposited PdNi-Si Schottky barriers are fabricated and characterised. The back to back architecture ensures low current operation at all biases. Palladium causes the Hydrogen molecules to dissociate and be absorbed by the film, while Nickel makes the sensor resistant to repeated cycling in the Hydrogen environment. The sensors exhibit extremely low idle currents, large percentage current increases on Hydrogen exposure and high selectivity for Hydrogen. These factors, in addition to the simplicity of fabrication and easy integration with conventional electronics show that electrodeposited PdNi-Si Schottky barriers are well suited for use as Hydrogen sensors.

The workfunction change in PdNi films exposed to Hydrogen is used to characterise CNTs contacted by electrodeposited PdNi. The PdNi contacted CNTs exhibit ohmic characteristics, which change on exposure to Hydrogen. Examining this change allows differentiation between semiconducting and metallic CNTs. Raman spectroscopy is used to characterise the same CNTs and the results are compared with the electrical characterisation in Hydrogen. The electrical and Raman analysis experimentally verify the theoretically assigned CNT Raman features.

The fabrication and electrical characterisation of CNT transistors incorporating electrodeposited PdNi contacts are presented. The CNTs are spin coated from a 1,2-dichlorobenzene dispersion and contacted with electrodeposited PdNi. The PdNi-Si Schottky barrier is used to suppress the current through the Silicon substrate during electrical characterisation. The operating restrictions imposed by the direct PdNi-Si contact and methods to overcome the same are discussed. The characteristics of the CNT transistor in a changing magnetic field at room temperature are presented.

CONTENTS

DECLARATION OF AUTHORSHIP

I, Ashwin Usgaocar, declare that the thesis entitled:

"Integration of electrodeposited PdNi alloys with Silicon and Carbon nanotube electronics"

and the work presented in it are my own. I confirm that:

- this work was done wholly or mainly while in candidature for a research degree at this University;
- where any part of this thesis has previously been submitted for a degree or any other qualification at this University or any other institution, this has been clearly stated;
- where I have consulted the published work of others, this is always clearly attributed;
- where I have quoted from the work of others, the source is always given. With the exception of such quotations, this thesis is entirely my own work.
- where the thesis is based on work done by myself jointly with others, I have made clear exactly what I have contributed by myself and for the integrality of projects, I have made clear what was done by others
- parts of this work have been published in research journals. A list of publications is provided with this manuscript.

Signed:

Date:

LIST OF PUBLICATIONS

Journal papers

Electrodeposited PdNi as possible ferromagnetic contacts for Carbon nanotubes

A.R. Usgaocar, C.H. de Groot, Physica Status Solidi(b), Vol 247 Iss 4, Pg 888-891, 2010.

Electrodeposition, composition control and characterisation of PdNi Alloys

A.R. Usgaocar, C.H. de Groot, Submitted to Journal of Electroanalytical Chemistry, Sept 2010.

Low power Hydrogen gas sensors using PdNi-Si Schottky barriers

A.R. Usgaocar, C.H. de Groot, Cedric Boulart, Alain Castillo, Valérie Chavagnac, submitted to Sensors and Actuators B, Sept 2010.

Low Power Hydrogen Sensors using Electrodeposited PdNi-Si Schottky diodes

A.R. Usgaocar, C.H. de Groot, Cedric Boulart, Alain Castillo, Valérie Chavagnac, European Patent application EP10290469.5.

Electrical and Raman characterisation of Carbon nanotubes using Hydrogen

A.R. Usgaocar, Harold M. Chong, C.H. de Groot, submitted to Journal of Applied Physics, January 2010.

Conference Presentations

Electrodeposited PdNi as possible ferromagnetic contacts for Carbon nanotubes

A.R. Usgaocar, C.H. de Groot, E-MRS, Strasbourg, France, June 2009.

Low power Hydrogen gas sensors using PdNi-Si Schottky barriers

A.R. Usgaocar, C.H. de Groot, Cedric Boulart, Alain Castillo, Valérie Chavagnac, Eurosensors 2010, Linz, Austria, Sept 2010.

Low power Hydrogen gas sensors using PdNi-Si Schottky barriers.

A.R. Usgaocar, C.H. de Groot, Cedric Boulart, Alain Castillo, Valérie Chavagnac, Procedia Engg. Vol 5, Pg 143-146, 2010.

ACKNOWLEDGEMENTS

A PhD should encapsulate an individual's contribution to scientific knowledge, but in my case, it would have been impossible without help from many of my colleagues. I would like to express my thanks to everyone who have a stake in the completion of the work described in this thesis.

First of all, I would like to like to express my deep gratitude to my supervisor, Dr. Kees de Groot, for his excellent guidance during the course of my PhD. His methodical approach to science and especially in experimental science was extremely educational and the trust and freedom he offered served as a huge confidence boost. This PhD was started before the university's cleanroom facilities had completely recovered from a devastating fire and he was responsible for setting a course that was minimally inconvenienced by the lack of a fully functional cleanroom. I am also very thankful for his support for my post doctoral plans. A special thanks to Dr. Harold M. Chong for his help with the Raman spectroscopy and Prof. Hiroshi Mizuta for all his assessments and contributions during my internal vivas. I would also like to thank the School of Electronics and Computer Science in the University of Southampton for fully funding my PhD.

I would like to thank Dr. Muhammed Khaled Hussain, Dr. David Gonzalez and Dr Xiaoli Li for the electrodeposition and electrical characterisation training. Their inputs and tips for improving my work have been most valuable. I also have to thank Sun Kai, Yu Dong, Marek Schmidt and Kanad Mallik for their help with photolithography, Raman spectroscopy and furnace use. Prof Peter de Groot and Dr. Daowei Wang very generously allowed me to use the VSM and for this, I am thankful. I also thank Dr. Shuncai Wang for his training and help in SEM and EDX usage. This work would have remained a pipe dream without the cleanroom staff Dave Sager, Neil Sessions, Katie Chamberlain, Richard Kean, Denny Jack and Peter Ayliffe who did their best to accomodate all strange requests for training, equipment and processes. A big thank you to the nano group secretaries Glenys and Luch, who very effectvely shielded me from all administrative issues.

The Nano research group is the most cosmopolitan places I have worked in and meeting people from all over the world has been both enjoyable and enriching. Surprising facts and

busted myths defined this “cultural exchange” and I feel I am finishing the PhD as a wiser person. For this, I would like to thank every member of the Nano group for making it such a fantastic workplace.

On the extra-curricular front, I would like to thank Kamal and Ananth for being so proactive in organising potlucks and movie outings, and Rama, Sonali and Johnny for making said events so enjoyable. Big thanks to Ananth, Belal, John, Luis and Maral for the heart stopping, lung bursting squash and tennis games. Chasing a ball around till you drop dead may not sound very logical, but life would have been a lot poorer without it. I also have to thank the huge group from the FESM skills training course (you know who you are) for the dinner outings sampling international fayre in Southampton.

Finally, a HUGE thank you to my parents, grandparents and my family from across the pond for always supporting me in whatever choices I have made. The constant phone calls, emails and personal visits, especially during the last year of my PhD, helped overcome many of the stresses that cropped up unbidden and unwelcome. I hope I make you proud.

1. INTRODUCTION

One of the defining features of the last few decades is the explosive growth in the capability and use of electronics and information technology (IT). Since the invention of the transistor in 1947 and the integrated circuit (IC) in 1958, the electronics industry has been on a relentless drive of miniaturisation, driven by Moore's law, which predicts the doubling of transistor density in an IC every two years. The rising device density is accompanied by a growth in capability and speed and has put electronics at the heart of most human endeavours today. This impressive record has been built primarily using a small collection of inorganic semiconductors (Si, Ge, GaAs) and a multitude of manufacturing processes that are continuously refined to reliably achieve increasingly smaller feature sizes. Most commercial innovation has therefore used one of these semiconductors as the substrate.

Recent trends suggest that future innovation may aim for goals other than miniaturisation and performance. Scaling has brought electronic devices close to fundamental limits in size beyond which it may be impossible or impractical to satisfy Moore's law any more. The growth of fast and reliable networks and new applications such as smart clothing, distributed sensing, large scale photovoltaics and thermoelectrics have also started to make niche attributes like mobility, low power consumption, flexibility and high energy conversion efficiencies more valuable. The limits in Silicon scaling and the new demand for electronics for niche applications has led researchers to study new materials such as Carbon nanotubes (CNTs), Graphene and semiconducting polymers as well as new paradigms, such as spintronics, where the electronic spin is used instead of charge for information transmission and storage. These research avenues may involve fundamental shifts in the materials, structures and physics of electronic devices and are a good opportunity to investigate new or previously disregarded processes as well.

This PhD focusses on electrodeposited Palladium Nickel contacts to Silicon and CNTs and their use in Hydrogen sensing and CNT field effect transistors (CNTFETs). The choice of the PdNi alloy was primarily due to previous reports on the formation of high quality and reproducible Pd-CNT contacts. In addition, Palladium catalyses the dissociation of Hydrogen molecules and exhibits property changes on exposure to Hydrogen. Pure Palladium experiences mechanical stresses on Hydrogen exposure which are alleviated by alloying with Nickel. The high quality Pd-CNT contact and the presence of ferromagnetic Nickel also make PdNi alloys especially suitable for CNT based spintronic devices. Thus PdNi alloys are a good contacting material for the fabrication and study of Hydrogen sensors as well as CNT based electronic and spintronic devices.

Electrodeposition has many attractive features compared with competing metallisation processes such as evaporation and sputtering. It is a simple and inexpensive process that does not require any vacuum conditions for its operation. As it is not a line-of-sight process, it is capable of depositing conformal films as in the Damascene process [1], developed by IBM to deposit conformal Copper interconnects in circuits. Deposition from a solution also enables deposition of three dimensional structures, such as the inverse sphere magnetic nanoarrays deposited using polystyrene nanospheres [2]. Electrodeposition was chosen for this work because previous studies have demonstrated that electrodeposited Ni-Si Schottky diodes exhibited lower reverse bias currents and higher on/off ratios compared to evaporated Schottky diodes. The quality of the contacts play an extremely important role in CNT based electronics and therefore any improvement in contact quality or controllability is beneficial. In this thesis, electrodeposited PdNi-Si and PdNi-CNT contacts were fabricated and electrically characterised to investigate their quality and properties.

Chapter 2 describes the development of a process to electrodeposit PdNi alloys with controllable compositions. The compositions of the deposited films were found using Energy dispersive X-Rays (EDX) and were correlated with the deposition parameters used. The magnetic properties of the deposited films were studied using vibrating sample magnetometry (VSM) to gauge the suitability of electrodeposited PdNi as ferromagnetic contacts in spintronic devices. The electrodeposition process requires that the PdNi film be deposited directly on exposed Silicon and therefore a PdNi-Si contact is always formed. In a device where the PdNi films also contact a CNT, the PdNi-Si contacts can form a leakage path through the Silicon substrate, as shown in Fig. 1.1(a). It is therefore important to study the PdNi-Si electrical characteristics to judge whether the leakage current can be suppressed by reverse biasing the PdNi-Si Schottky diodes as shown in Fig. 1.1(b). In addition, the presence of a Schottky barrier is also necessary for spin injection from PdNi into Silicon. The properties of electrodeposited PdNi-Si contacts are therefore an important part of this PhD and their electrical characterisation is presented in this chapter.

Palladium and Palladium Nickel alloys are widely used as Hydrogen sensors, due to Palladium's ability to catalyse the dissociation of Hydrogen molecules and exhibit changes in its properties on Hydrogen absorption. Alloying with Nickel makes the Palladium film more

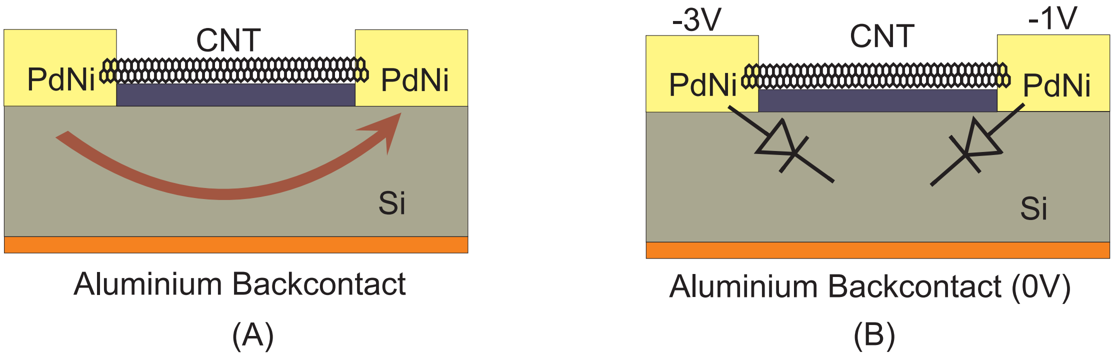

Fig. 1.1: *Schematic of the CNT transistor incorporating electrodeposited PdNi alloy source and drain contacts. (a)The parasitic conductance path through the Si substrate present due to the direct contact between electrodeposited films and the Silicon substrate. (b) A biasing scheme for reducing the leakage current by reverse biasing the two front side Schottky barriers.*

robust in handling multiple Hydrogen exposures. The low reverse bias currents of PdNi-Si Schottky barriers were used to fabricate low power Hydrogen sensors, which were characterised in different Hydrogen pressures. The sensor was designed as a back to back Schottky diode pair which draws very low idle current and exhibits large percentage increases in current on Hydrogen exposure. The fabrication process and the electrical characterisation of this sensor are presented in Chapter 3.

CNTs have sparked tremendous research interest due to their unique properties and they are being investigated for use in a wide variety of applications ranging from nanocomposites to transistors. The interest in employing them in electronics stems from their high mobilities, a possibility of ballistic transport and their occurrence in semiconducting and metallic forms. The electronic properties of CNTs are usually studied by using them as a transistor channel and modulating their band structure via an electrostatically coupled gate. An alternative method of electrically characterising CNTs is possible in devices with PdNi-CNT contacts and involves modulation of the PdNi workfunction by exposure to Hydrogen. PdNi contacted CNTs were electrically characterised in air and in Hydrogen and their nature (semiconducting or metallic) was deduced from the electrical characteristics. Raman spectroscopy was also performed on the same CNTs and the conclusions from both methods were compared. A brief overview of CNT electronic properties and the results of electrical characterisation in air and Hydrogen are reported in Chapter 4.

Chapter 5 presents a brief overview on the use of CNTs as transistors. The processes used to fabricate CNTFETs by spin coating CNTs onto a Silicon substrate and contacting them with electrodeposited PdNi electrodes are described. The CNTFETs are electrically characterised and the contact resistance of the PdNi-CNT is compared to those reported for other contacting metals. The importance of the gate in suppressing the leakage current through the PdNi-Si interface and possible improvements to the transistor are discussed.

The work presented in this thesis forms the foundation for subsequent research into electrodeposition and the advantages it can bring to micro/nanofabrication. The PdNi-Si Schottky barrier based Hydrogen sensors, CNTFETs with electrodeposited PdNi contacts and the study of CNT properties using Hydrogen modulated contacts all offer new avenues for research. A summary of the results of this work and the possible research problems that arise from it are outlined in Chapter 6.

2. ELECTRODEPOSITION OF PALLADIUM NICKEL ALLOYS

This chapter describes the development of an electrodeposition process for PdNi films with controllable compositions. The electrodeposition theory and the experimental techniques used to deposit and characterise PdNi films are discussed. PdNi films are deposited at different deposition potentials from baths with different Nickel and Palladium salt concentrations. The compositions of the deposited films were measured using Energy dispersive X-rays (EDX) and correlated with the electrodeposition process parameters. The ability to predict the composition of the deposited PdNi films from the deposition potential and currents in individual Nickel and Palladium baths is demonstrated. The electrical and magnetic characteristics of the PdNi films are examined. High quality PdNi-Si Schottky barriers and ferromagnetic character are observed, making the electrodeposited PdNi films suitable for use as contacts in electronic and spintronic devices.

Part of this chapter is published in Physica Status Solidi (b), **247**, 888, 2010. Part of this work is submitted to Journal of Electroanalytical chemistry.

2.1 Introduction

Electrodeposition has been used as a metallisation technique for close to two centuries, primarily as a means of coating other metals to protect against corrosion or to improve appearance. This simple and mature technology is now being investigated for a variety of applications requiring single metal or alloy depositions. The primary advantages of using this technique in electronics is the ability to deposit metal layers without a vacuum and the ability to deposit conformal and 3D metallic structures. Moreover, metal electrodeposition is a low energy process and when used to form a metal-semiconductor interface, it can suppress intermixing and form superior contacts.

This chapter reports on the development of an electrodeposition process for PdNi alloys. An overview of the electrodeposition theory is presented, followed by a description of the electrodeposition technique used and the results from trials to deposit good quality alloy films with controllable composition. The electrical and magnetic properties of the deposited alloy films are studied using current voltage (I-V) and vibrating sample magnetometry (VSM) to gauge their suitability for use in CNT transistors and as ferromagnetic contacts in spintronic devices. The process developed in this chapter is used in subsequent chapters as a fabrication technique for Hydrogen sensors and CNT devices with electrodeposited PdNi contacts.

2.2 Electrodeposition Theory

2.2.1 Deposition of metals

The underlying principle of metal electrodeposition is the reduction of metal ions from a salt solution to form a solid metal. When an electrode made of any material is immersed in an electrolyte, a charge transfer occurs till the Fermi level of the electrode and the redox potential of the electrolyte are equal. For metallic electrodes, the charge transfer causes a thin layer of charge to develop on the electrode surface [3], whose polarity depends on the difference between the metal Fermi level and the redox potential of the solution. For semiconducting electrodes, the lower carrier density leads to the formation of a depletion layer at the electrode surface. An equilibrium is soon reached, wherein the net charge transfer across the electrode-electrolyte interphase drops to zero and a potential develops across it. This potential can be measured by connecting the electrode to a Pt/H_2 electrode, also called the standard Hydrogen electrode and arbitrarily assigned a potential of zero to act as a reference for all other electrode potentials. The measured potential is termed the equilibrium potential (E) and depends on the electrode material and the activity of the ionic species in the electrolyte. For standardisation, the equilibrium potential for each metal electrode is measured in an electrolyte of its salt with activity 1. This potential is termed the relative standard electrode potential (E°) of the particular material. The relation between the equilibrium potential, relative standard electrode potential and the solution activity is given by the Nernst equation [4].

$$E = E^\circ + \frac{2.303RT}{zeN_A} \log a(M^{z+}) \tag{2.1}$$

where R is the gas constant, T is the absolute temperature, e is electronic charge, N_A is Avogadro's Number, z is the valency of the ionic species involved in the reduction reaction and $a(M^{z+})$ is the activity of the ionic species in the electrolyte.

The equilibrium potential is the potential across the electrode-electrolyte interphase when no current flows between the electrodes. In order to induce a current flow, an external potential has to be applied to the system. If the potential required to drive a current I through the cell is $E(I)$, then the overpotential η is defined as

$$\eta = E(I) - E \tag{2.2}$$

A negative overpotential is required for reduction of ions at the cathode, i.e the external applied potential has to be more negative than the equilibrium potential. For metals and n-type Si, this causes accumulation of electrons at the electrode surface, from where they can easily reduce the ions in the electrolyte. Similarly, a positive overpotential can be used to initiate an oxidation reaction at a metal or n-type Silicon electrodes, as it favours the transfer of electrons from the electrolyte to the electrode.

For large negative overpotentials, the current density (current per unit area of the electrode) through the electrochemical system varies exponentially as described in Ref. [4]

$$i = i_o \exp \frac{(-\alpha z \eta e N_A)}{RT} \tag{2.3}$$

where i_o is the exchange current density, which is the unidirectional current flow between electrode and electrolyte or vice versa at equilibrium (the *net* current is zero) [5] and α is called the transfer coefficient.

At even more negative overpotentials, the current density is limited by the mass transport of metal ions that carry the current through the solution between the electrodes. The value of the limiting current density is given by

$$i_L = \frac{neN_A D}{\delta} C_b \tag{2.4}$$

where n is the number of electrons involved in the reaction, D is the diffusion constant for the particular metallic species, δ is the thickness of the diffusion layer and C_b is the concentration of the metal ion in the bulk of the solution [4].

The dependence of the current density in the electrochemical bath on the overpotential is shown in Fig. 2.1. As the potential increases, the magnitude of current density first increases linearly till the equilibrium potential of the metal is exceeded, then rises exponentially and finally saturates when the current density is restricted by the total mass transport ability of the solution [3]. Since the current in the cell basically denotes the

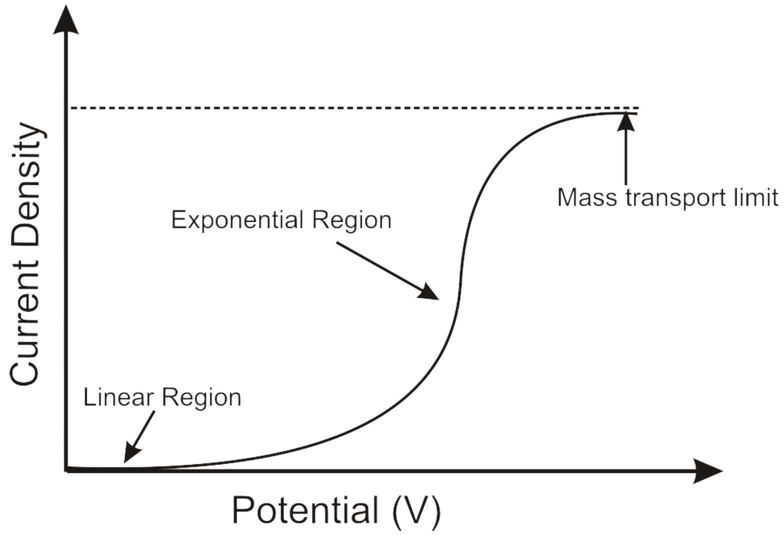

Fig. 2.1: *Variation of current with applied potential during the electrodeposition process. The linear region corresponds to the potentials below the equilibrium potential of the ionic species. The exponential region corresponds to the unhindered electrodeposition and the mass transport limit is when the current flow is saturated by the mass transport ability of the bath.*

transfer of electrons between the electrode and the ions in the bath, the rate of metal deposition is correlated with the current density. As the metal ions are consumed in the reduction reaction, the ion concentration in the bath is reduced. To counter this concentration reduction, an anode of the same material as the ions can be chosen. The anode then progressively dissolves over the lifetime of the bath and replenishes the ions lost in the cathodic process.

2.2.2 Film thickness control

The thickness of the electrodeposited film is controlled by measuring the current through the system and integrating with time to give the total charge deposited in each trial. Consider that the total charge consumed at the cathode is denoted by Q_T. This represents the charge consumed at the cathode by all reactions that require a transfer of electrons (metal deposition, Hydrogen evolution etc). If the charge consumed purely by the metal ion reduction process is denoted by Q_M, then we can model this charge as

$$Q_M = \alpha . Q_T \tag{2.5}$$

where α is called the current efficiency.

Since Q_M is consumed purely for metal reduction, it can be equated to

$$Q_M = \alpha.Q_T = n.z.N_A.e \tag{2.6}$$

where n is the number of moles of the metal ion deposited on the substrate, z is the valency of each metal ion and therefore the number of electrons consumed during reduction of one ion, N_A is Avogadro's number and e is the electronic charge.The mass of the film that contains these number of moles is

$$M_{film} = n.M_{Metal} \tag{2.7}$$

where M_{Film} is the mass of the film and M_{Metal} is the atomic mass of the metal being deposited. Since density is a characteristic property of the deposited metal, it is possible to calculate the thickness of the film from the mass and density. The equation relating the metal thickness to the measured charge is therefore

$$t_{Film} = \frac{\alpha.Q.M_{Metal}}{z.N_A.e.\rho_{Metal}.A_{Film}} \tag{2.8}$$

where t_{Film} is the thickness of the deposited film, ρ_{Metal} is the density of the deposited metal and A_{Film} is the area of the deposited metal film.

The value of α is not known at the outset and is calculated by experimentally measuring the thickness of a deposited film using a profiler or other techniques like vibrating sample magnetometry for magnetic materials. The value of α can vary largely depending on the strength of parasitic reactions such as Hydrogen evolution. For controlled electrodeposition conditions however, α usually lies between 0.7 to 0.9 and a representative value from a few trials can be chosen to calculate the charge required to deposit a specific film thickness.

2.2.3 Deposition of alloys

To deposit an alloy instead of a single metal, the electrochemical solution has to contain salts of all metals to be alloyed. However, differences between metal equilibrium potentials mean that their deposition potentials can be quite different from each other. This presents a problem because the applied overpotential will cause the alloy constituents to be deposited at markedly different rates, leading to poor composition control and deleterious effects on the film quality if deposition rates are too high. The deposition potentials of the constituent metals therefore have to be as close to each other as possible and ideally equal. Eq. 2.1

shows that the deposition potential depends on the relative standard electrode potential (characteristic of a metal) and the activity of the metal ion, which has a concentration dependence. The difference between equilibrium potentials of the constituent metals can therefore be reduced by changing the concentration or by using chelating agents to bind the metal ions in solution and control their activity [4].

Once the deposition potentials are adjusted, it is necessary to analyse the current density vs. potential curves of each individual metal solution as well as the alloy solution to find the deposition potentials and the deposition rates. A hypothetical set of current density-potential curves for two separate metals M_1 and M_2 plotted in the same graph are shown in Fig. 2.2. This figure shows that at potential V_1, the metal M_1 and M_2 are deposited at a rate proportional to i_1 and i_2 respectively. An alloy film deposited at potential V_1 can therefore be expected to contain metals M_1 and M_2 in the ratio $i_1 : i_2$. The current density-potential curve for the alloy solution should be used to choose the optimum current density range for depositing alloy films, while the data from the individual solutions are used to predict the composition of the films.

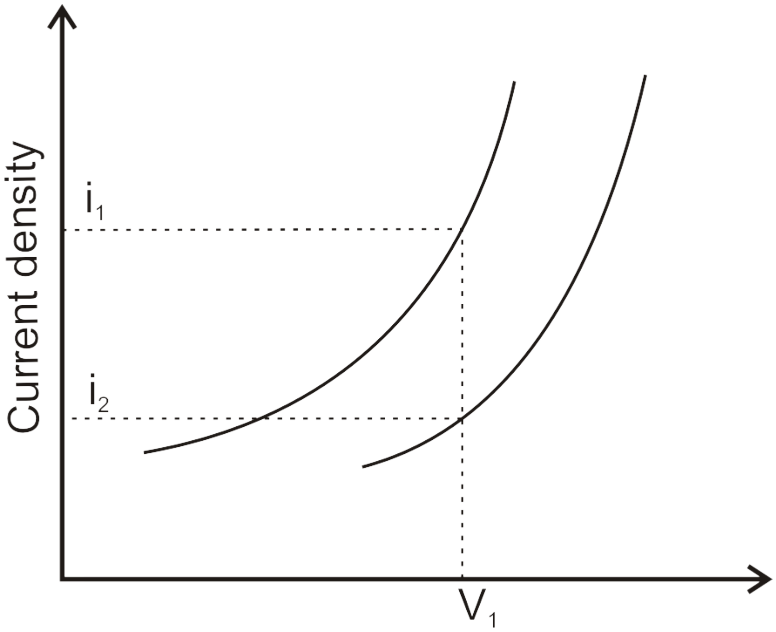

Fig. 2.2: *Relationship between alloy composition and current density-voltage curves of individual metallic species in the electrochemical bath. An alloy deposited at* V_1 *can be expected to have metals* M_1 *and* M_2 *in the ratio* $i_1 : i_2$*.*

The film thickness for single metal depositions is calculated as described in Section 2.2.2 using the characteristic properties of the metal. In the case of an alloy, the density and effective atomic weight have to be calculated based on the fractions of the constituent metals. The expressions for the effective density and atomic weight of the alloy can be derived by assuming that mass and volume are conserved in the alloying process. The expressions for the effective alloy density and atomic weight are

$$\frac{1}{\rho_{Alloy}} = \frac{x_{Ni}}{\rho_{Ni}} + \frac{x_{Pd}}{\rho_{Pd}} \tag{2.9}$$

$$\frac{1}{M_{Alloy}} = \frac{x_{Ni}}{M_{Ni}} + \frac{x_{Pd}}{M_{Pd}} \tag{2.10}$$

where x_{Ni} and x_{Pd} are the mass percentages of the Nickel and Palladium in the film, ρ_{Ni} and ρ_{Pd} are the Nickel and Palladium densities respectively and M_{Ni} and M_{Pd} are the atomic weights of Nickel and Palladium respectively. The mass percentages used in Eq. 2.9 and Eq. 2.10 were obtained from Energy dispersive X-Ray measurements.

2.2.4 Hydrogen Evolution

A parasitic reaction that may occur during electrodeposition is the reduction of Hydrogen ions to form Hydrogen gas at the cathode. While some of the evolved Hydrogen escapes as gas, some may get embedded in the metal film. Incorporation of Hydrogen can stress and embrittle the metal film, which is a major problem during metal electrodeposition [6, 7]. It can cause especially large stresses in Palladium deposits due to the large volume difference between the pure Palladium and Palladium hydride lattices. A very memorable quote from Schlesinger [4] on Hydrogen embrittlement describes how Zinc plated steel springs destroyed themselves with audible “shrieks” in order to release trapped Hydrogen.

The general technique of inhibiting Hydrogen evolution and codeposition is to electrodeposit the metal or alloy at low overpotentials. The Hydrogen reduction reaction therefore also sees a low overpotential, which suppresses the Hydrogen evolution. A second method is to use neutral or alkaline solutions, which contain a lower number of Hydrogen ions and consequently result in lower Hydrogen evolution. Alloying with Nickel makes the Palladium films more resistant to the deleterious effects of Hydrogen incorporation and can thus improve film robustness. In this project, all the solutions were made slightly alkaline (pH 7-7.5) and the film deposition was performed at potentials as low as possible. Hydrogen incorporation may have occurred during the pretreatment pulse, but no harmful effects were observed.

2.3 Analytical Techniques

2.3.1 Energy Dispersive X-Ray Spectroscopy

Energy dispersive X-Ray spectroscopy (EDX or EDS) is an analytical technique used to study the chemical composition of a material. It is usually used in conjunction with a scanning electron microscope and therefore allows elemental analysis of areas or features with lateral dimensions as small as 1 μm^2. The EDX signal includes data collected from a depth of up to 1 μm from the surface of the sample and due to backscattering of electrons the actual volume of the sample over which data is collected may be significantly larger than 1 μm^3. For characterisation of thin surface films however, it is possible to simply ignore the substrate response to obtain the film composition. The accuracy of elemental proportions also depends on a number of factors such as material, accelerating voltage etc, but is typically around 0.1% for elements above atomic number 10 and less accurate for smaller atoms.

During the EDX analysis, the sample is bombarded with a collimated, high energy electron beam, which knocks out some of the inner shell electrons in the atoms of the material being analysed. The vacancies left behind in the inner shells are ultimately filled by outer shell electrons. The energy lost by the outer shell electrons in this transition is released as X-Rays which are collected by a detector and transformed into a voltage proportional to the X-Ray energy. These energies are dependent on the energy differences between the atomic orbitals and thus provide a unique signature for each element. By studying the number of emitted X-Rays of each energy, it is possible to find the elements present in the material and their relative proportions. Fig. 2.3(a) shows the possible electronic transitions between different energy levels in the atom after bombardment by an electron beam. Each of the L,M and N orbitals are in fact composed of subshells with finer energy separations. The large number of possible transitions give rise to a number of line series, which are classified on the basis of the energy orbital the electron is transitioning to. As shown in Fig. 2.3(b), the low atomic number elements predominantly emit X-Rays in the K series while elements with higher atomic numbers emit lines in the L and M series [8]. Electronic transitions to the K orbitals also produce the highest percentage of characteristic X-Rays compared to the L and M series, with the rest of the electrons emitted as Auger electrons. Comprehensive tables and graphs for all elemental X-Ray lines are available in the literature and are used to identify the elements from the X-Ray data.

A typical plot of the EDX measurement is shown in Fig. 2.4 with the peak assignments

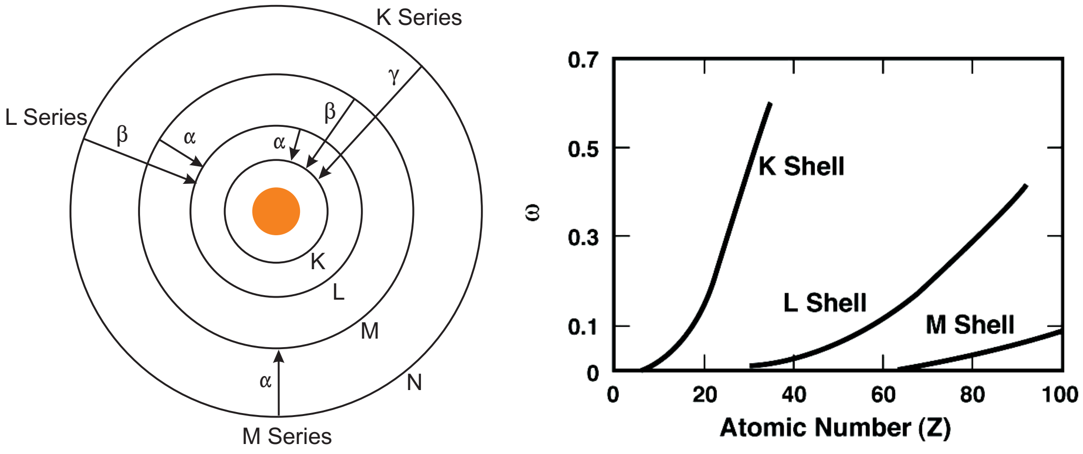

(a) (b)

Fig. 2.3: *(a) The possible electronic transitions that can lead to X-Ray emission from an individual atom. The different series are identified based on the desitination orbital of the electrons. (b) Dependence of the fraction of ionisation events that produce characteristic X-Rays [8]. The remainder produce Auger electrons.*

based on data from Ref. [8]. It is seen that there are multiple peaks for Nickel and Palladium. The Nickel lines are in the K series and the L series, while the Palladium lines are in the L series. The multiple peaks for Palladium are due to electrons transitioning from two different higher energy subshells to the L orbital.

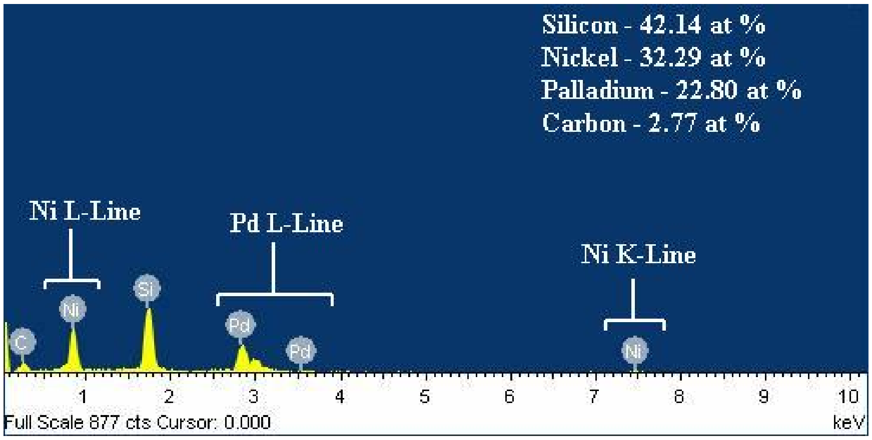

Fig. 2.4: *A typical EDX measurement plot. The peak positions are characteristic to the element and intensity is proportional to the quantity.*

2.3.2 Vibrating Sample Magnetometry

Vibrating sample magnetometry (VSM) is an analytical technique used to measure the magnetisation of materials and operates on the principle that a changing magnetic field induces an electrical current in the detection coils. The VSM equipment consists of an electromagnet to create a controllable magnetic field, a vibration unit to drive the sample oscillations and Hall sensors used as detection coils. A schematic of the VSM setup is shown in Fig. 2.5.

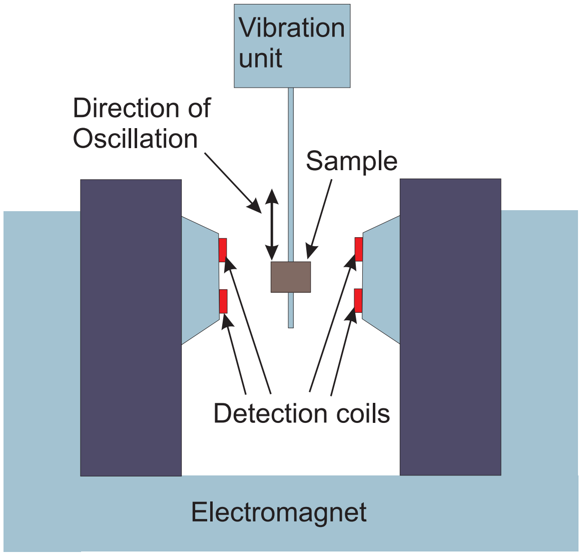

Fig. 2.5: *Schematic representation of a vibrating sample magnetometry system. The sample is positioned in the field of the electromagnet and subjected to vertical oscillations. The changing magnetic field induces a current in the detection coils proportional to the sample magnetisation.*

The sample to be measured is mounted in a holder and positioned in a constant magnetic field created by the electromagnet. The position of maximum response is selected by measuring the sample magnetisation at a range of vertical positions and angles for a fixed magnetic field. The field from the electromagnet magnetises the sample and creates a stray magnetic field that is proportional to the sample magnetisation. The sample is kept stationary till the magnetisation is complete, after which vertical oscillations are started as shown in Fig. 2.5. The movement of the sample and the stray magnetic field induce a current in the detection coils that is proportional to the sample magnetisation. Since the field created by the electromagnet is not varying, it will not contribute to the induced current in the coils and the only signal measured is due to the magnetised sample [9]. Once a measurement is complete, the field of the electromagnet is changed and the measurement repeated. No measurements are taken till the electromagnet field has stabilised in order to eliminate the effect of the electromagnet field and also to eliminate any lag between the change in field and the change in sample magnetisation. The M-H curve for the material is thus obtained by measuring the magnetisation over the desired range of positive and negative magnetic fields.

2.4 Experimental details

A three electrode electrochemical cell, as shown in Fig. 2.6, has been used during this work to electrodeposit PdNi films. The external potential (E_{Ext} in Fig. 2.6) causes the Nickel and Palladium ions to migrate to the cathode, where they get reduced and attach themselves as solid metal to the cathode surface, forming the film. Choosing an anode to replenish the ions in the alloy electrolyte is not feasible because the anode will have to reflect the exact composition of each bath. A Platinum mesh was chosen for the anode, as it allows oxidation reactions to proceed without producing any contaminants. Since a Silicon chip acts as the cathode, there is no mechanism to replenish the ions consumed in the reduction reaction. However, it was calculated that for the typical bath composition and charge consumption in each trial (≈ 100mC), it would require about 170 trials before the concentration of the

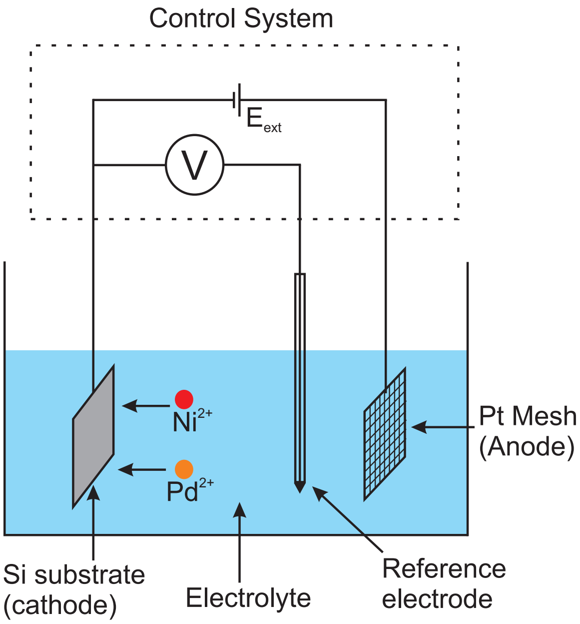

Fig. 2.6: *Schematic representation of a three terminal electrodeposition cell. Application of an external potential drives metal ions to the cathode where they get reduced and are deposited as films.*

rarer salt drops to 90% of its original value. This figure is much higher that the number of trials performed with any one solution and thus the problem of a reduction in the amount of metallic species can be safely ignored. The control system shown in Fig. 2.6 was an Autolab PGSTAT30 electrochemical system and all electrodepositions were performed at room temperature using a calomel reference electrode.

Before electrodepositing metal films, cyclic voltammetry (CV) is used to characterise the combination of the electrochemical bath and deposition substrate. Cyclic voltammetry gives the relationship between the current generated in the bath and the applied potential and is useful in identifying potentials that give rise to the optimum current density. The applied potential is varied as a triangular wave between two switching values, as shown in Fig. 2.7(a).

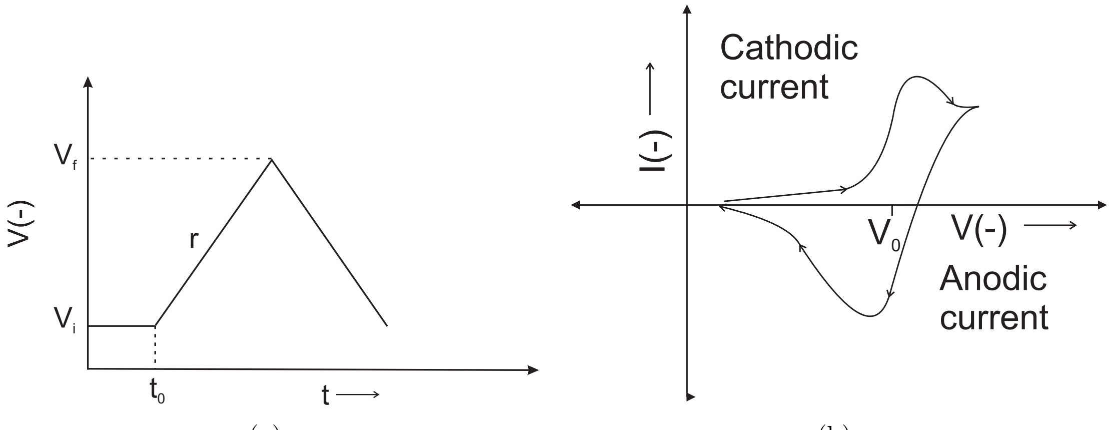

(a) (b)

Fig. 2.7: *(a)Variation of applied potential with time during cyclic voltammetry. The switching potentials V_i and V_f, the rate of potential change r and the start time of the ramp t_0 are process parameters.(b) Variation of current with applied potential during cyclic voltammetry. The cathodic and anodic peaks are formed due to imbalances between the consumption and replenishment of ions near the cathode and anode respectively.*

An illustrative curve showing the dependence of current on applied potential during cyclic voltammetry is shown in Fig. 2.7(b). The locations and magnitudes of the anodic and cathodic peaks can be used to extensively characterise the electrochemical system. In this study, cyclic voltammetry was used only to find the potentials at which Nickel and Palladium deposition started and to choose deposition potentials such that the desired current densities were obtained.

After choosing the deposition potential from the cyclic voltammetry data, a few high potential and short duration (≈ 0.1 s) pretreatment pulses are applied to the cell. Paunovic and Schlesinger [3] show that the critical number of atoms required to form a cluster during deposition is inversely dependent on the overpotential. A high negative pulse potential was therefore chosen to facilitate formation of a large number of small clusters on the electrode surface while the short duration of the pulse ensured that the clusters did not grow and form a continuous film. These clusters then serve as anchors and growth sites [10] during the subsequent deposition at lower potentials, improving film adhesion and smoothness.

The final step is the use of DC amperometry to deposit the film. DC amperometry involves the application of a constant deposition potential to the cell. The deposited charge is measured in real time via the deposition current and the amperometry is stopped when the desired charge has been deposited. The deposition potential was chosen from the range of potentials that yielded a current density between 3 to 5 mA/cm^2. This current density range was chosen after multiple trials comparing the deposition current densities and the quality of the resultant films. Current densities below this value formed slow growing, discontinuous and grainy films, while higher current densities formed powdery and brittle films as shown in Fig. 2.8. These results are similar to those observed in previous work examining the dependence between film quality and current density [5].

A recipe for the electrochemical PdNi bath used in this work was found from the literature [11] and is listed in Table 2.1. The pure Nickel and pure Palladium baths were derived from the PdNi bath by removing the Palladium and Nickel salts respectively, while keeping all other constituents the same. Nickel sulphate ($NiSO_4$) and Palladium ethylenediamine dichloride ($Pd(en)Cl_2$) are the Nickel and Palladium ion sources respectively. Ethylenediamine is a complexing agent that reduces the difference between the Palladium and Nickel equilibrium potentials by controlling the activity of the Palladium ions in solution. Deionised (DI) water was used as the solvent and the pH of the solution was adjusted between

Table 2.1: *PdNi electrodeposition constituents from Ref [11]. The individual metal solutions were prepared by using only one metal salt and keeping the concentration of the other constituents the same. Nickel and Palladium baths were used to obtain the cyclic voltametry curves for the individual metals.*

Chemical	**Pd Bath (g/L)**	**Ni Bath(g/L)**	**PdNi Bath(g/L)**
$Pd(en)Cl_2$	16.7	0	16.7
$NiSO_4$	0	33.3	33.3
$(NH_4)_2SO_4$	16.7	16.7	16.7
NH_3(35%)	45 ml/L	45 ml/L	45 ml/L

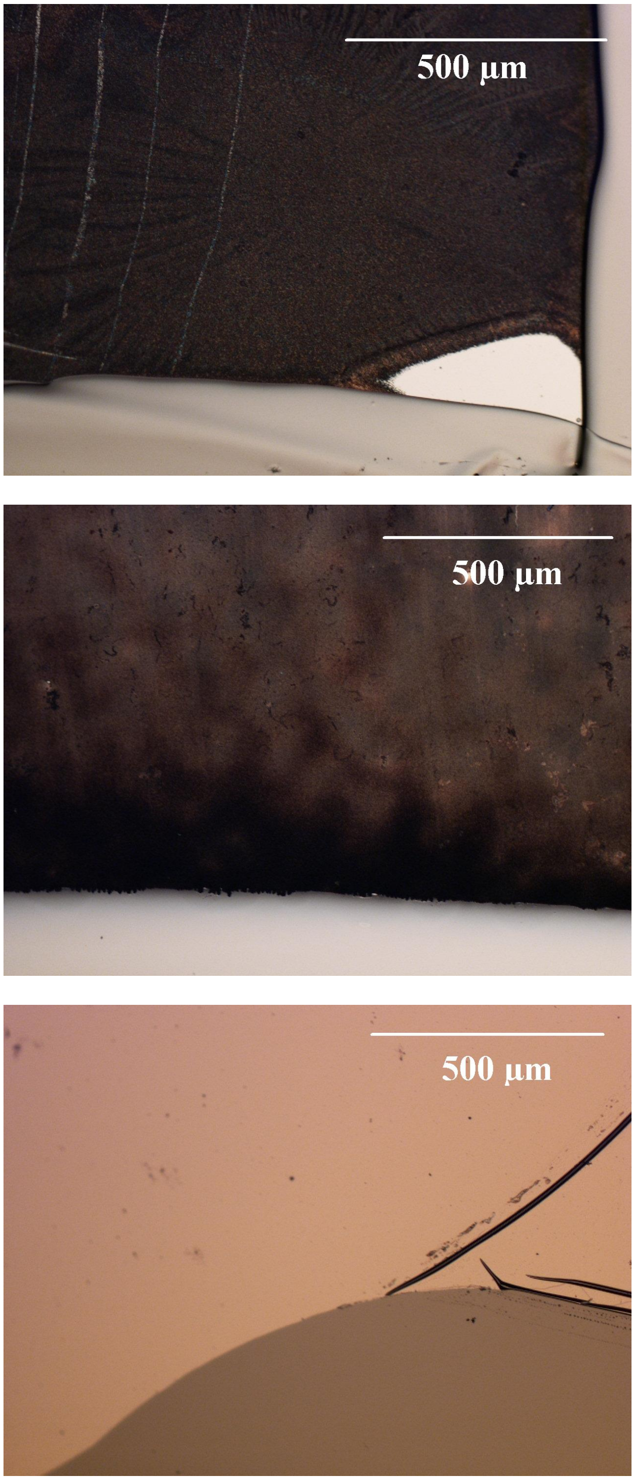

Fig. 2.8: *Optical images of PdNi alloy films electrodeposited at (a) low current densities (<3 mA/cm^2). (b) High current densities (>5 mA/cm^2) and (c) Current density in the 3-5 mA/cm^2 range. The low current density films tended to be discontinuous and took a long time to form. The high current density films were powdery and brittle with a "burnt" appearance. Films deposited at the right current density range were found to be continuous and formed relatively quickly.*

7 to 7.5 by using Sulphuric acid and Ammonia as required. The three baths were prepared with the constituents as listed in Table 2.1 to allow deposition using purely Nickel, purely Palladium and PdNi electrolytes. An n-type, ⟨100⟩ Silicon wafer of resistivity 0.019-0.021 Ω.cm was cleaved into 1.5 × 0.5 cm^2 chips, washed with Acetone and Isopropyl alcohol (IPA) and coated with an insulating varnish to define a 1 × 0.5 cm^2 window. The native oxide in the window was etched by dipping in 20:1 HF followed by a quick rinse in DI water. The chip was then immersed into the proper electrochemical bath and the metal was deposited into the window.

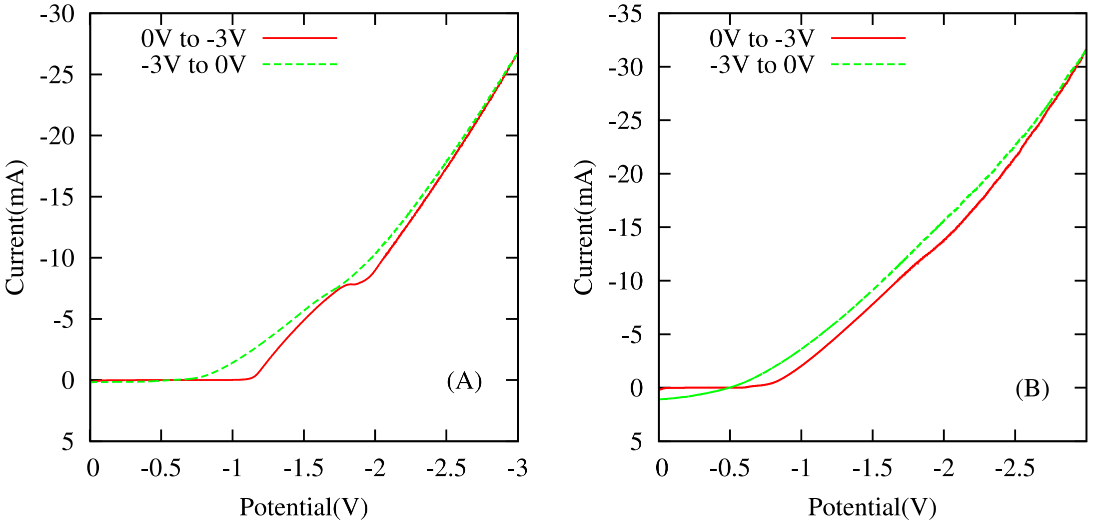

Fig. 2.9: *Cyclic voltametry curves for (a)27.75 g/L Nickel and (b)27.75 g/L Palladium solution showing the forward and reverse scans. The deposition potentials for Nickel and Palladium are seen to be around -1.2 V and -0.8 V respectively.*

Typical cyclic voltammetry curves for Nickel and Palladium solutions are shown in Fig. 2.9. It is seen that the Nickel and Palladium currents increase drastically at around -1.2 V and -0.8 V respectively, which are their deposition potentials from these baths. The currents observed during the reverse sweep in Fig. 2.9(b) are higher than those during the forward sweep. This is because the first potential scan increases the substrate conductivity by depositing a layer of metal on the Silicon and hence enhances the deposition current.

Cyclic voltammetry curves were similarly measured for the PdNi bath and deposition potentials were chosen so as to yield current densities between 3 to 5 mA/cm^2. Between 1 to 3 high potential pretreatment pulses (≈ -2.5 V) were applied for about 0.1 s to improve film adhesion and quality [12]. The PdNi films were then deposited at the chosen potentials. The pretreatment pulses did improve film adhesion, but most PdNi films started peeling off when their thickness exceeded about 100nm, as estimated from the deposited charge. For this project, film thicknesses of upto 100nm were sufficient and therefore no effort was made to improve the adhesion of thicker films. The deposited films were then analysed using EDX and VSM measurements to study their composition and magnetic characteristics.

2.5 Compositional Analysis

The composition of the deposited film was studied using a JEOL 6500 EDX system. The EDX data were measured at multiple points on the film and the measured Nickel and Palladium percentages were normalised to 100% as they were the only contributors from the film while the measured Silicon content originated from the substrate. The average of the normalised Nickel and Palladium contents was taken to be representative of the film's composition. The locations of the points where EDX data were collected for two samples are shown in Fig. 2.10 and Fig. 2.11 and the associated EDX data are tabulated in Table. 2.2 and Table. 2.3

The EDX measurement reports both the atomic and weight percentages of the constituent elements. The properties which are of interest in this project e.g magnetism, metal-CNT junction characteristics depend more on the number of atoms of each metal present in the film than their weights. For this reason the atomic percentage was chosen for all further analysis. The EDX data listed in Table. 2.2 have a lower standard deviation compared to that in Table 2.3. This shows that the deposited film in Fig. 2.10 is more uniform compared to that in Fig. 2.11. The non-uniformity in Fig. 2.11 is borne out by the EDX spectra no. 5,6 and 7 which were measured in the lighter areas of the film and showed a higher percentage of Nickel and Palladium relative to Silicon as compared to the values recorded in the darker areas. The primary difference between these samples is that the sample in Fig. 2.10 has an ohmic Aluminium back contact while that in Fig. 2.11 does not. The ohmic back contact constitutes a low resistance current path to all areas of the chip and thus improves the uniformity of the deposited film. The data in this chapter has a mixture of samples with and without back contacts but the devices fabricated in subsequent chapters all used an ohmic back contact to improve film uniformity.

Further depositions and EDX measurements were performed using solutions with different Nickel and Palladium concentrations. The recipe listed in Table. 2.1 was modified by varying the $NiSO_4$ concentration from 16.65 g/L to 49.95 g/L and by varying the $Pd(en)Cl_2$ concentration from 38.85 g/L to 5.55 g/L such that the numerical total of the two was always 55.5 g/L. The Ammonium sulphate concentration was kept the same in all solutions.

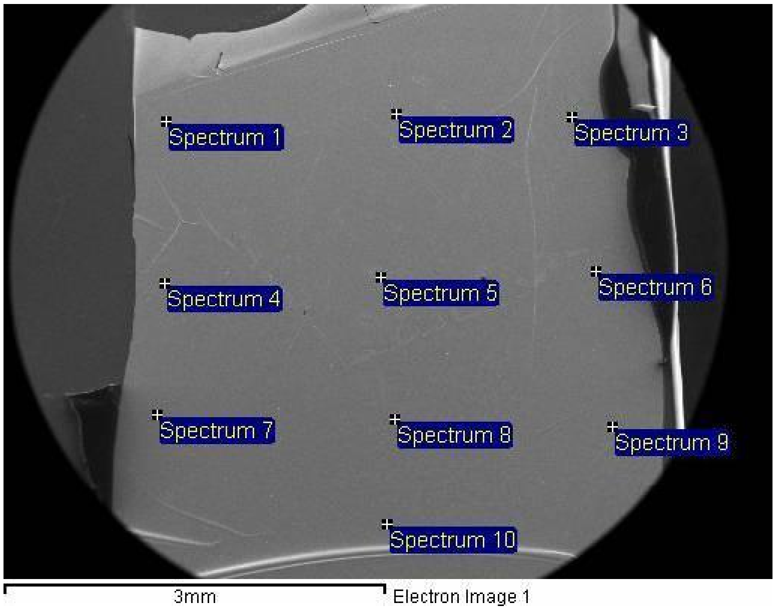

Fig. 2.10: *Points on a section of electrodeposited* $Pd_{0.63}Ni_{0.37}$ *film where the composition was measured by EDX. This film is deposited on a Silicon substrate with an Aluminium back contact.*

Table 2.2: *EDX data obtained from points marked in Fig. 2.10. The mean of the normalised Nickel percentage represents the film composition.*

Spect. No.	Ni		Pd		Si		Ni (Norm)	
	(Wt %)	(At %)	(Wt %)	(At %)	(Wt. %)	(At %)	(Wt. %)	(At %)
1	18.32	17.10	59.43	30.61	18.84	36.75	23.56	35.84
2	17.01	15.01	56.64	27.58	22.80	42.07	23.10	35.24
3	19.76	17.56	55.59	27.25	20.87	38.76	26.22	39.18
4	19.00	19.21	58.12	32.42	22.88	48.37	24.64	37.20
5	17.48	14.08	54.10	24.05	22.23	37.44	24.42	36.92
6	19.19	16.84	54.56	26.43	22.77	41.77	26.02	38.91
7	17.58	14.72	54.15	25.02	23.66	41.42	24.51	37.04
8	16.06	11.61	51.06	20.37	23.82	36.00	23.93	36.30
9	18.05	16.6	56.7	28.76	22.86	43.93	24.15	36.59
10	18.73	15.96	52.87	24.87	24.81	44.21	26.16	39.08
						Mean	**24.67**	**37.24**
						Std. Dev	**1.05**	**1.32**

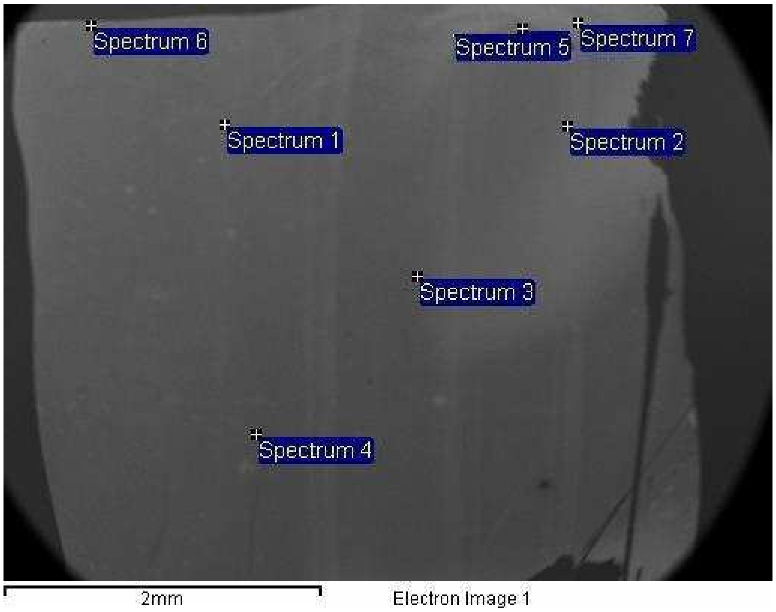

Fig. 2.11: *Points on a section of electrodeposited* $Pd_{0.79}Ni_{0.21}$ *film where the composition was measured by EDX. This film is deposited on a Silicon substrate without an Aluminium back contact.*

Table 2.3: *EDX data obtained from points marked in Fig. 2.11. The mean of the normalised Nickel percentage represents the film composition. The absence of an Aluminium back contact makes this film less uniform than that shown in Fig. 2.10.*

Spect.	Ni		Pd		Si		Ni (Norm)	
No.	(Wt %)	(At %)	(Wt %)	(At %)	(Wt. %)	(At %)	(Wt. %)	(At %)
1	5.87	5.31	59.97	29.98	34.17	64.71	8.92	15.05
2	7.86	6.10	52.80	22.61	35.92	58.29	12.96	21.25
3	7.42	6.23	55.48	25.69	35.81	62.82	11.80	19.52
4	7.15	6.43	61.93	30.72	29.04	54.56	10.35	17.31
5	13.42	15.81	73.50	47.80	11.83	29.14	15.44	24.85
6	11.41	14.37	76.20	52.99	12.39	32.64	13.02	21.33
7	14.04	18.30	76.05	54.69	9.91	27.01	15.58	25.07
						Mean	**12.58**	**20.63**
						Std. Dev	**2.285**	**3.420**

While Ammonia was used to adjust the solution pH, its concentration differed from the value listed in Table. 2.1 by at most 1 ml/L. A summary of the EDX results obtained from samples deposited from different solutions is shown in Table. 2.4. The Nickel content of the solution is calculated as the percentage of Nickel atoms to the total of Nickel and Palladium atoms in the solution.

Table 2.4: *PdNi film compositions for different deposited films calculated by averaging EDX data at multiple locations. The deposition potentials of some of these samples was changed during deposition to restrict the current density to 3-5 mA/cm*^{2}.

Sample Number	Norm. Ni At % (Solution)	Norm. Ni At% (Film)	Norm. Ni Wt% (Film)	Dep. Potential (V)
1	78.33	20.63	12.58	-1.1
2	78.33	13.04	7.67	-1.1
5	84.47	29.30	18.61	-1.0
16	94.23	75.29	62.84	-1.6
17	94.23	66.90	52.73	-1.2
20	87.88	24.75	15.36	-1.2
21	87.88	47.16	33.04	-1.5
22	87.88	47.34	33.19	-1.2
74	43.95	0	0	-0.9
73	43.95	0	0	-0.9
81	64.45	11.31	6.81	CV
82	64.45	0	0	-0.8
67	100.00	100.00	100.00	-1.2

Table 2.4 shows that while the Nickel content of the film generally increased with increasing Nickel content in solution, significant variations were observed between some samples deposited from the same bath. Notable examples of this variation are samples 20 and 21, deposited from the same bath, but with one having double the Nickel content of the other and samples 81 and 82, where one film recorded no Nickel content. This suggests that the film's Nickel content depends on a second factor, possibly the deposition potential.

In order to investigate the dependence on deposition potential, it was assumed that the composition of the deposited alloy depends on the ratio of currents in the individual baths at the deposition potential, as described in Sec. 2.2.3. The currents in the individual baths at the chosen deposition potential were measured from the individual cyclic voltammetry curves and the ratio of the Nickel current to the total current was calculated. Fig. 2.12 shows sections of the cyclic voltammetry curves for three different sets of Nickel and Palladium baths near the PdNi deposition potentials. For each curve in Fig. 2.12, a PdNi film was deposited using the same deposition potential and salt concentrations used in the figure. The nominal values of Nickel concentration in the film were calculated as

$$Ni_{Nom} = \frac{I_{Ni}}{I_{Ni} + I_{Pd}} \tag{2.11}$$

where Ni_{Nom} is the nominal Nickel content of the film, I_{Ni} and I_{Pd} are the currents measured from the individual Nickel and Palladium baths at the PdNi alloy deposition potential. The EDX data and the deposition conditions for the devices fabricated from these solutions are listed in Table. 2.5.

Table 2.5: *Currents in the individual Nickel and Palladium baths at the deposition potentials used and a comparison between the nominal and EDX values of the Nickel content in the deposited film. The nominal value is calculated from the measured currents in the Nickel and Palladium baths.*

Sample Number	Dep. Potential (V)	Fig.	I_{Ni} (mA)	I_{Pd} (mA)	Ni % (nominal)	Ni % (EDX)
16	-1.60	2.12(a)	1.09	0.42	72	75.29
22	-1.24	2.12(b)	0.15	0.21	42	47.34
73	-0.89	2.12(c)	0.0018	0.46	0	0

Table. 2.5 shows that the nominal and measured values of the film composition are close to each other, which bears out the assumption of the film composition being governed by the individual Nickel and Palladium currents at the deposition potential. The role of the deposition potential also explains the discrepancy between samples 81 and 82 listed in Table. 2.4. While both these films were deposited from the same bath, sample 81 was deposited by cyclic voltammetry with the deposition potential was swept from 0 to -2 V. The more negative potentials would have deposited Nickel as well as Palladium, resulting in a Nickel content of 11.31%. Sample 82 on the other hand was deposited at -0.75 V, which is not negative enough to deposit Nickel.

However, the nominal and measured values still have some differences and this could be due to the pretreatment pulses applied to the samples during deposition. No pretreatment pulses were applied before cyclic voltammetry, while 1 to 3 pulses were applied prior to deposition. These differences in the initial conditions can also result in different Nickel contents. To rigorously study the relationship between deposition potential and film com-

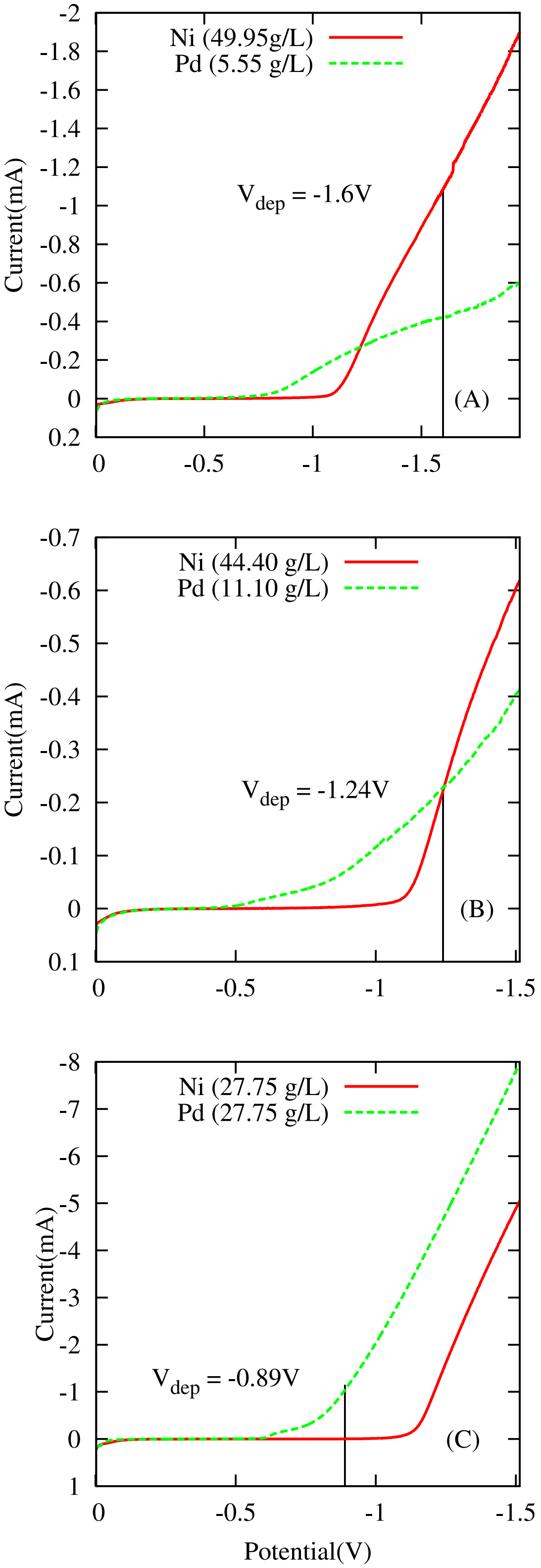

Fig. 2.12: *Sections of cyclic voltametry curves for Nickel and Palladium baths of different concentrations. The deposition potentials used in PdNi deposition are shown with black vertical lines. The currents at the deposition potential are used to calculate the nominal Nickel content.*

position, it is necessary to use the same initial conditions for the cyclic voltammetry as well as the deposition.

To accomplish this, three pretreatment pulses of -2.5 V were applied for 0.1 s prior to both cyclic voltammetry and deposition. The nominal values of the film compositions were computed from cyclic voltammetry curves of the Nickel-only and Palladium-only solutions. The PdNi films were deposited from a 44.4 g/L $NiSO_4$ and 11.1 g/L $Pd(en)Cl_2$ bath using different deposition potentials. The nominal composition values were then compared with those measured using EDX and their dependence on deposition potential is plotted in Fig. 2.13. It is seen that the nominal and measured compositions show good agreement for potentials more negative than -1 V, as beyond this potential both Nickel and Palladium start depositing. The differences in film composition at lower deposition potentials could be due to Nickel deposition from the pretreatment pulses. The high potential facilitated the deposition of some Nickel, while predominantly Palladium was deposited in the subsequent deposition step.

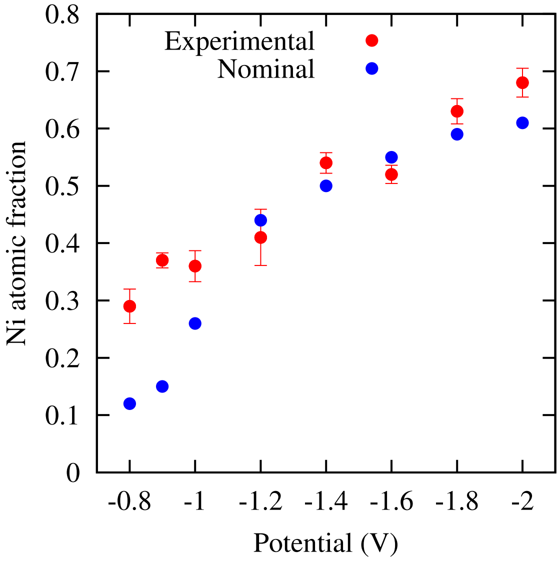

Fig. 2.13: *Nominal and EDX measured compositions of films deposited at different potentials using a PdNi bath with 44.4 g/L* $NiSO_4$ *and 11.1 g/L Palladium (equivalent to 80% Nickel content).*

It is thus possible to predict the composition of the deposited film by examining the currents at the deposition potential from the cyclic voltammetry curves of the solutions of the constituent metals. The final composition of the film depends more on the deposition potential than the bath composition. Sartorelli *et al.* [7] have also demonstrated alloy composition control via the deposition potential, though the relationship between the currents in the constituent baths and the alloy composition was not established. For high Nickel concentrations, the pure Nickel and pure Palladium baths showed a cross over point as seen in Fig. 2.12(a) and 2.12(b), allowing deposition of films that are Nickel rich, Palladium rich or with similar Nickel and Palladium concentrations simply by using the appropriate deposition potential. Low Nickel concentration baths such as the one in Fig. 2.12(c) did not exhibit this crossover point and can therefore deposit only Palladium rich films.

2.6 Electrical Characterisation of PdNi-Si Schottky barriers.

To study the PdNi-Si contacts, a 1-2 Ω.cm, ⟨100⟩ Silicon wafer with 20 nm thermal oxide and an Aluminium back contact was used. The wafer was sawed into chips and circular and square patterns ranging in size from 1.5 mm down to 0.2 mm were described on each chip. The thermal oxide from the patterns was etched away to form an oxide mask that restricted the electrodeposition to only the patterned areas. The back contact and sides of the chip were coated with an electrically insulating varnish to prevent metal deposition in any unwanted areas. After the electrodeposition of a PdNi film, the I-V characteristics of the contact were measured at room temperature using an Agilent 4155C semiconductor parameter analyser.

Fig. 2.14 shows the variation of current density (J) with applied potential for $\mathrm{Pd_xNi_{1-x}}$-Si Schottky diodes. It can be seen that the Schottky diodes exhibit very low reverse bias currents and high on/off current ratios with the forward bias current at least four orders of magnitude higher than the reverse bias current. The reverse bias currents of the diodes are in the range of 1 - 15 $\mu\mathrm{A/cm^2}$ and no breakdown is observed till biases of -3 V. It is seen that the PdNi Schottky barriers showed superior characteristics (lower reverse bias current and higher forward bias current) compared to pure Nickel or pure Palladium Schottky diodes. The differences in the forward bias region are essentially due to differences in series resistance, while those in the reverse bias region could be due to a difference in the contact area or the barrier height, both of which depend on the individual interface properties. Previous investigations on electrodeposited Ni-Si Schottky barriers [12] have reported Ni-Si Schottky barriers with on and off currents differing by about seven orders of magnitude while a difference of four orders of magnitude is observed in this work. This suggests that the electrodeposition parameters used to deposit films in this work are better suited to forming PdNi-Si Schottky barriers than Ni-Si or Pd-Si ones.

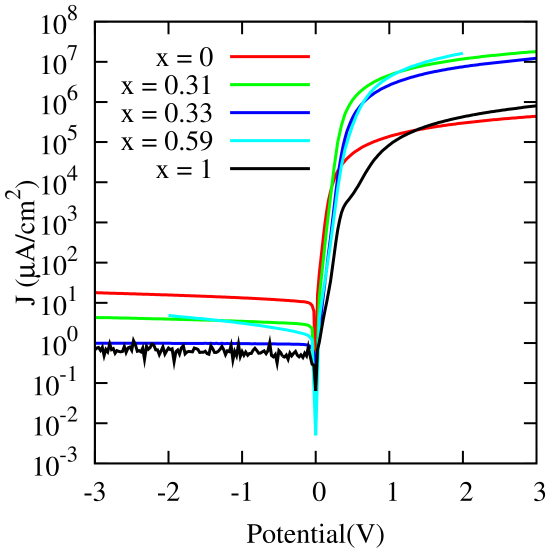

Fig. 2.14: *Current density (J) vs voltage (V) characteristics of electrodeposited* Pd_xNi_{1-x}*-Silicon Schottky barriers. The Schottky barriers have very low reverse bias currents and large on/off current ratios.*

At room temperature, thermionic emission is usually the dominant current conduction mechanism in the Schottky diode as some electrons possess enough energy to scale the barrier [13]. Since all measurements were performed at room temperature, the thermionic emission model is used to extract the Schottky barrier parameters. The current through the Schottky barrier due to thermionic emission is given by

$$I = I_s(\exp{(qV/\eta kT)} - 1) \tag{2.12}$$

where I is the current measured at applied voltage V, I_s is the reverse saturation current, q is the electron charge(1.6×10^{-19} C), η is the ideality factor of the diode, k is the Boltzmann constant and T is the absolute temperature. The reverse saturation current is further expressed as

$$I_s = AA^*T^2. \exp{(-q\phi_B/kT)} \tag{2.13}$$

where A is the active area of the Schottky diode, ϕ_B is the barrier height and A^* is the effective Richardson constant. The value of the effective Richardson constant is given by

$$A^* = 4\pi m^* qk^2/h^3 = 1.2 \times 10^2 (m^*/m)\ AK^{-2}cm^{-2} \tag{2.14}$$

where m^* is the semiconductor effective electron mass and m is the electron mass (9.11×10^{-31}kg).

For some semiconductors, the effective Richardson constant is independent of the direction of the lattice, but in Silicon, it has a direction dependence. The value of the effective Richardson constant is 246 $\mathrm{AK^{-2}cm^{-2}}$ and 258 $\mathrm{AK^{-2}cm^{-2}}$ for the $\langle 100\rangle$ and the $\langle 111\rangle$ directions respectively. Since $\langle 100\rangle$ wafers were used to fabricate the Schottky barriers, the Richardson constant value for the $\langle 100\rangle$ direction is used.

In the linear low forward bias region of the Schottky barrier characteristic, when the applied potential is much greater than $3kT/q$, the exponential part of Eq. 2.12 dominates the diode current. Eq. 2.12 can therefore be written as

$$\begin{aligned} I &= I_s . \exp\left(qV/\eta kT\right) \\ \Rightarrow \ln I &= \ln I_s + \frac{qV}{\eta kT} \end{aligned} \tag{2.15}$$

The plot of the natural logarithm of the current with the voltage is therefore linear and the y-intercept gives the value of $\ln I_s$. Using this value, the active area and Eq. 2.13, the Schottky Barrier height can be calculated.

$$\phi_B = -\frac{\ln\left(J_s/A^*T^2\right)kT}{q} \tag{2.16}$$

The ideality factor η can be calculated from the slope of the $\ln(\mathrm{I}) - \mathrm{V}$ curve.

$$\eta = \left[\frac{q}{kT}\right] \cdot \left[\frac{dV}{d(\ln I)}\right] \tag{2.17}$$

The ideality factor value generally lies between 1 and 2. A value close to 1 signifies a good fit of the thermionic emission model to the I-V data and consequently that thermionic emission is the dominant current conduction mechanism in the Schottky barrier. Values of the ideality factor above 2 indicate that the thermionic emission model does not fit the I-V data well and could be due to thermionic emission not being the dominant conduction mechanism.

The Schottky barrier characteristics were analysed using the thermionic emission model as described. A linear fit of the low forward bias region of the J-V plot was done and the slope and intercept of the line were used to extract the Schottky barrier height Φ_{B} and ideality factor η.

A representative subset of the data from all measured Schottky barriers is presented in Table. 2.6. This table shows that the leakage current at a reverse bias of -1 V (J_{rev}) is extremely small. The ideality factor η is between 1 and 2 for all the listed devices, showing

Table 2.6: *Schottky barrier characteristics measured from different Pd_xNi_{1-x} films. The reverse bias current density is defined as the current density at -1 V.*

Film. Ni % (EDX)	η	Φ_B (eV)	J_{rev} (μA/cm^2)
0	1.71	0.70	-1.72
41.60	1.26	0.84	-8.21
67.12	1.14	0.83	-0.80
68.92	1.02	0.80	-0.69
100	1.07	0.75	-0.91

that the assumption of thermionic emission being the dominant current conduction mechanism is valid. Fig. 2.15 shows the dependence of the Schottky barrier height with the Nickel percentage in the metal films that formed the Schottky barrier. The data does not show a strong correlation between the Nickel content of the film and the measured barrier height. This could be due to the similarity of the Nickel (5.15 eV) and Palladium (5.12 eV) workfunctions, which means the Schottky diode characteristics should not change significantly with film composition. In addition, planar Schottky barrier heights are primarily determined by Fermi level pinning rather than the metal work functions and therefore the properties of the metal-Si interface play a more important role in determining the Schottky

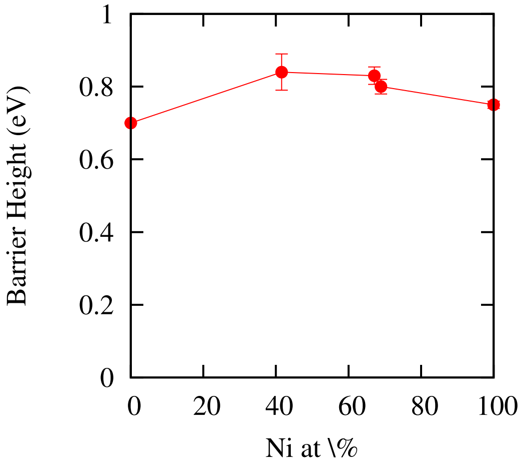

Fig. 2.15: *Dependence of Schottky barrier height on the Nickel atomic percentage in Pd_xNi_{1-x} films.*

barrier heights.

2.7 Magnetic characterisation of PdNi alloy films.

An aim of this project was also to gauge the suitability of the PdNi alloys as ferromagnetic contacts in spintronic devices. For this purpose, it is important to study the magnetic properties of the alloys, to verify that they exhibit ferromagnetism and to investigate the strength of the ferromagnetism for different Nickel contents. The magnetic character of the films was studied using an Oxford instruments Aerosonic 3001 Vibrating Sample Magnetometer (VSM) with measurements performed at room temperature.

Fig. 2.16 shows results from VSM measurements on different PdNi alloy films with varying Nickel content. Fig. 2.16(a) depicts the raw data recorded by the VSM for $\mathrm{Pd_xNi_{1-x}}$ alloys with x <0.5. This figure highlights the effect of the different film masses on the perceived magnetisation of the alloys by suggesting that the $\mathrm{Pd_{0.25}Ni_{0.75}}$ alloy has a higher magnetisation compared to pure Nickel, which is counter intuitive. The magnetisations per unit mass for the data in Fig. 2.16(a) were therefore calculated and are plotted in Fig. 2.16(b). This figure shows that after compensating for the film mass, the pure Nickel film has the highest saturation magnetisation. Fig. 2.16(c) and Fig. 2.16(d) show the raw data and magnetisation per unit mass respectively for $\mathrm{Pd_xNi_{1-x}}$ alloys with x >0.5. A comparison of Fig. 2.16(b) and Fig. 2.16(d) shows that the saturation magnetisation per unit mass of the alloy decreases with Nickel content, as expected. On the whole, Fig. 2.16 shows that well defined hysteresis is observed even in samples with a Nickel atomic percentage of 35%, in agreement with previous studies showing ferromagnetic properties in PdNi alloys for low Nickel concentrations [14, 15].

The saturation magnetisation and remnant magnetisation per unit mass were calculated in order to account for the large variation in the film masses. The mass of the alloy film was computed from the electrodeposited charge using the method described in Sec. 2.2.2. It can be seen from Fig. 2.16(b) that the response of the pure Palladium sample is close to linear, as expected from a paramagnetic material. However, the mass magnetic susceptibility of Palladium as calculated from the slope of the linear fit to the Palladium response was 1.37×10^{-4} m^3/kg, four orders of magnitude higher than the value of 6.57×10^{-8} m^3/kg listed in the literature [16]. The magnetisation value measured by the VSM has contributions from the metal film, the Silicon substrate and also from the sample holder and Carbon tape used to secure the sample. The Silicon substrate and Carbon tape are diamagnetic and have mass magnetic susceptibilities of (-1.6×10^{-9} m^3/kg) and (-6.2×10^{-9} m^3/kg)

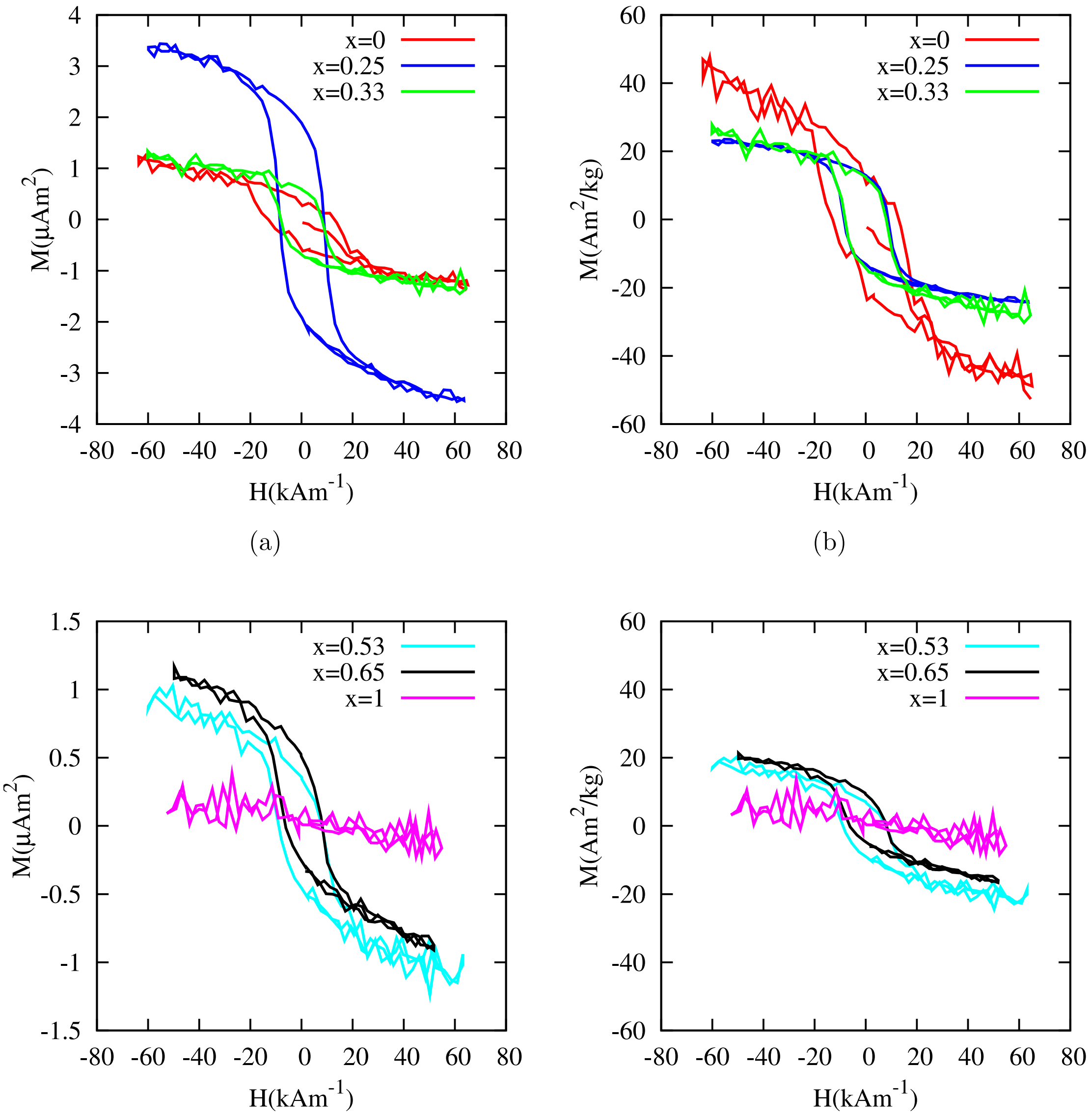

(a) (b)

(c) (d)

Fig. 2.16: *MH loops from VSM studies on Pd_xNi_{1-x} films.(a) Raw data from VSM measurements of alloys with $x < 0.5$. This data highlights the effect of different film thickness by causing the $Pd_{0.25}Ni_{0.75}$ alloy to show stronger magnetisation than the pure Nickel film (b) Magnetisation per unit mass for Pd_xNi_{1-x} alloys with $x < 0.5$. The compensation for mass shows that the pure Nickel film has the highest magnetisation. (c) Raw data from VSM measurements on Pd_xNi_{1-x} alloys with $x > 0.5$. (d) Magnetisation per unit mass for Pd_xNi_{1-x} alloys with $x > 0.5$. Comparing (b) and (d), it is seen that the saturation magnetisation increases with increasing Nickel content.*

respectively, an order of magnitude smaller than Palladium. This shows that the response of the pure Palladium sample is probably due in major part to the sample holder and constitutes the system response. The positive and negative values of the saturation magnetisation for the remaining samples were calculated by averaging six data points from the extremes of the magnetic field sweep. The remnant magnetisation and coercivities were extracted from the y and x-intercepts of the graphs respectively. The system response was compensated for by subtracting the saturation magnetisation of the pure Palladium sample from the data for other samples. The value of saturation magnetisation, remnant magnetisation and coercivity were then calculated as the average of their positive and negative values. The coercivity, saturation magnetisation and remnant magnetisations per unit mass at room temperature for all the measured samples are listed in Table. 2.7

Table 2.7: *Magnetic characteristics of* Pd_xNi_{1-x} *films as extracted from VSM, EDX and electrodeposition data.*

Ni (Norm at %)	Mass (g)($\times 10^{-5}$)	Ms/mass (Am^2/kg)	Mr/mass (Am^2/kg)	H_c (kA/m)
0	5.52	0	0	0
30.83	1.34	9.92	8.11	5.02
35.49	5.11	10.84	7.28	8.08
37.24	3.96	5.55	3.63	3.58
40.50	4.04	12.61	9.57	8.04
45.57	3.02	11.06	8.33	9.04
47.16	5.05	11.45	7.88	9.24
47.34	2.65	14.04	9.39	7.56
52.53	3.64	16.25	11.19	6.37
54.67	2.27	11.48	10.21	11.15
62.86	5.23	21.11	15.85	8.12
66.90	4.80	19.57	14.17	8.68
68.08	3.29	13.45	6.72	2.47
68.69	3.31	16.20	7.79	7.96
73.54	5.59	18.43	10.57	6.41
75.29	14.72	20.27	12.87	10.35
100	2.62	29.55	16.96	13.34

Fig. 2.17 plots the dependence of the saturation and remnant magnetisations per unit mass on the Nickel atomic percentages in the film, with the standard deviations used as error bars and a line connecting the points with 0 and 100% Nickel content. The fact that

most of the measured points are on or below this line shows that the magnetic moment per unit atom in the alloy is less than or equal to that of pure Nickel over the entire measured range of the alloy composition.

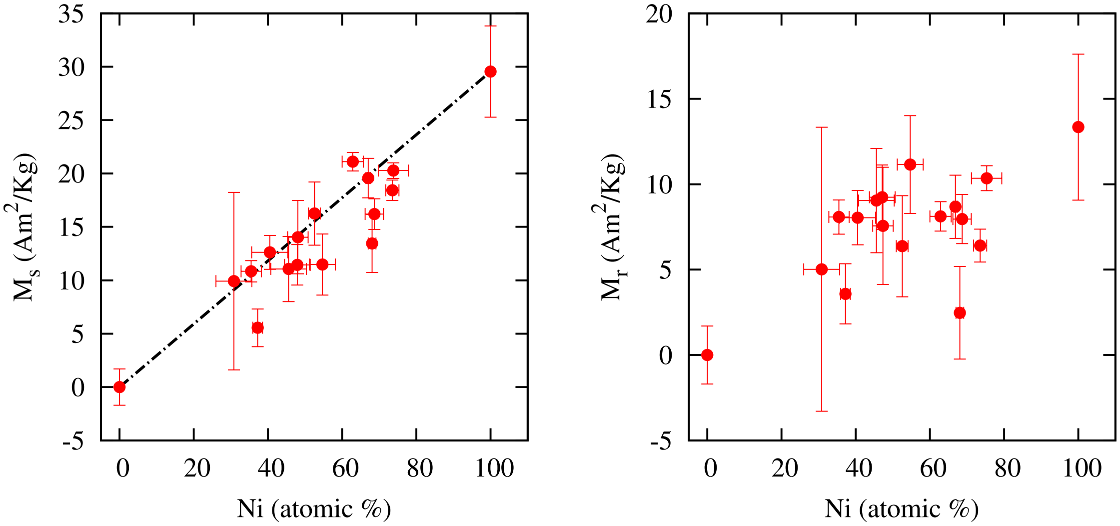

Fig. 2.17: *(a)Saturation and (b)Remnant magnetisation per unit mass as a function of Nickel content in* Pd_xNi_{1-x} *films, compensated for the Palladium response. Error bars are standard deviations in EDX and VSM measurements. The line in (a) is drawn between the pure Palladium and pure Nickel points.*

Fig. 2.17(a) shows that the saturation magnetisation increases with increasing Nickel content in the PdNi alloy. There is a wide scatter among the points, possibly due to the thinness of the films, which resulted in noisy VSM signals, as seen in Fig. 2.16. One way to reduce these errors is to use much thicker films, but in this project it has not been possible to reliably obtain films with thicknesses above 100 nm. The pure Nickel sample shows a saturation magnetisation per unit mass of about 30 Am^2/kg, which is about 55% of the actual Nickel value of 55 Am^2/kg [17]. This difference would primarily be due to the inefficiencies in the electrodeposition process [18], which were not accounted for when the film mass was calculated from the electrodeposited charge. It is possible that the noisy VSM signals also added an error. The remnant magnetisation, being a more complex magnetic property and not characteristic of a material like the saturation magnetisation per unit mass, did not exhibit any correlation with the Nickel content of the film. The coercivities of the films were found to be close to each other, probably due to similar film dimensions and the fact that Nickel is the major contributor to the magnetic response and therefore the Nickel component in all the films switch magnetisation at the same field. No strong dependence of the coercive field on the alloy composition is observed, as against previous studies [19]. This could possibly be due to formation of Nickel rich areas in the film which then determine the coercive field. A study of the film composition using a much larger set of data points will allow a more accurate estimation of the film uniformity.

Electrodeposited PdNi alloys, especially those with Nickel content above 40%, exhibit the saturation and remnant magnetisations required for fabricating ferromagnetic contacts in spintronic devices. The shape anisotropy will force the magnetisation to remain in the plane of the thin films and the coercive fields can be controlled by choosing appropriate planar dimensions. The formation of PdNi-Si Schottky barriers is also advantageous for use in Silicon spintronic devices, where Schottky barriers are necessary to overcome the conductivity mismatch problem [20, 21].

2.8 Conclusion

This chapter described the development of a process to electrodeposit PdNi alloys of varying Nickel content on Silicon. The electrochemical bath consists of Nickel and Palladium salts with concentrations adjusted to promote codeposition. Electrodeposition is possible on Silicon chips with and without back contacts, but the presence of a back contact improves the deposited film quality. A few high potential pretreatment pulses were applied to promote the growth of small metallic islands on the Silicon surface and the film was then grown by applying a lower potential to the cell. The film growth at lower potentials proceeds via deposition of material around the metal islands on the Silicon surface and good quality films are deposited at current densities between 3 to 5 $\mathrm{mA/cm^2}$. The composition of the deposited alloys can be controlled by changing the bath compositions or by using different deposition potentials with the same bath. Composition control using deposition potential also allows the deposition of multi layered stacks from the same electrochemical bath, with each layer having a different composition tailored for specific purposes. An example where this would be advantageous is in the construction of PdNi-Si Schottky diode Hydrogen sensors, as described in Chapter 3. The PdNi layer that forms the Schottky diode can be tailored to have a high Nickel content layer close to the Silicon surface for improved adhesion and a high Palladium content layer at the surface to improve the uptake of gaseous Hydrogen.

The electrical and magnetic properties of the deposited films were studied. Excellent PdNi-Si Schottky barriers are formed with very low reverse bias currents and large on/off ratios. All the alloy films are ferromagnetic with the saturation magnetisation increasing with Nickel content. These findings show that electrodeposited PdNi alloys can be used to fabricate contacts in electronic and also spintronic devices.

The results described in this chapter form the foundation for device fabrication using electrodeposited PdNi by providing a means for reliably depositing PdNi films with a specified composition. The subsequent chapters in this thesis will discuss the use of PdNi-Si Schottky barriers as Hydrogen sensors, analysis of CNTs contacted by electrodeposited PdNi and CNT transistors with electrodeposited PdNi contacts.

3. PALLADIUM BASED HYDROGEN SENSORS

This chapter describes the fabrication and characterisation of electrodeposited PdNi-Si Schottky barriers for use as low power Hydrogen sensors. The effects of Hydrogen absorption on the physical and electronic properties of Palladium films are described and the sensors based on these effects are reviewed. The fabrication process for back to back electrodeposited PdNi-Si Schottky diodes and their electrical characterisation in different Hydrogen pressures are described. The Palladium content causes the Hydrogen molecules to dissociate and be absorbed by the film, reducing the PdNi-Si Schottky barrier height and increasing the sensor current. The sensors exhibited extremely low idle currents, large percentage current increases on Hydrogen exposure and high selectivity for Hydrogen. These factors, in addition to the simplicity of the fabrication process and ability to easily integrate with conventional electronics proves the suitability of electrodeposited PdNi-Si Schottky barriers to low power Hydrogen sensors.

Results in this chapter have been submitted to Sensors and Actuators (b). The Hydrogen sensor described is the subject of European Patent application EP10290469.5.

3.1 Introduction

Research into Hydrogen production, storage and handling have picked up pace in recent years due to the potential of using Hydrogen as an alternative to fossil fuels in the future. As a fuel, Hydrogen is attractive due to its high calorific value and lack of any combustion byproducts other than water. However, the current methods of Hydrogen production are not suitable for small scale use which makes it difficult to consider it a replacement for transport fuels. Hydrogen is also an extremely flammable gas when mixed with Oxygen and this gives rise to safety concerns during storage and transport. For these reasons, any improvements in Hydrogen production, storage and detection techniques will boost the viability of Hydrogen as a fuel.

Platinum and Palladium are already used as catalysts in Hydrogen production and in fuel cells to improve the efficiency of electricity generation from Hydrogen and Oxygen. Palladium is also an interesting material for Hydrogen storage as it can absorb many times its own volume of Hydrogen gas. The Palladium surface catalyses the splitting of Hydrogen molecules into Hydrogen atoms, which then diffuse into the lattice and change the electrical properties of the metal. These changes can form the basis of a solid state Hydrogen gas sensor which can be used to monitor the quantity of Hydrogen or to detect Hydrogen leaks. The fact that it can play an important role in the production, storage and detection of Hydrogen makes Palladium an important material for designing the entire Hydrogen fuel supply chain.

Hydrogen sensors are also important tools in the study of deep sea vents, to understand conditions in their vicinity and to learn the effects of these conditions on the complex geochemical and biological processes at the sea bed. It is especially necessary to have sensors for gases like Hydrogen and Hydrogen sulphide as well as for pH to gather data in these environments [22]. Sensors for Methane [23] and Hydrogen sulphide [24] have already been developed but a Hydrogen sensor is still among the list of desirables. The sensor design is complicated further by the fact that these sensors usually operate as part of an automated submersible vehicle and have to function reliably at high pressures and temperatures. Current sensor designs make use of materials like Yittria-stabilized Zirconia ceramics [22, 25] but a simple sensor based on a Pd/Pd-alloy Schottky diode may also be useful in such environments. PdNi-Si Schottky diodes with extremely low reverse bias currents were described in the previous chapter. The property of Palladium to dissociate and absorb Hydrogen gas with an accompanying change in work function can be used to fabricate low power Hydrogen sensors from these Schottky diodes.

3.2 The Palladium Hydrogen system

Metals such as Palladium and Platinum facilitate the dissociation of Hydrogen molecules on their surfaces, following which the atomic Hydrogen gets absorbed into the metal film. the phase diagram of the Palladium Hydrogen mixture as described by Flanagan *et al.* [26] is shown in Fig. 3.1. Pure Palladium has an face centred cubic (FCC) structure with a lattice constant of 0.3890 nm at 298 K. Dissociation of Hydrogen molecules and diffusion of the newly formed Hydrogen atoms into the Palladium lattice changes the lattice constant of the crystal, with the degree of change depending on the quantity of absorbed Hydrogen. In dilute alloys where the Hydrogen concentration, defined as the ratio of Hydrogen to

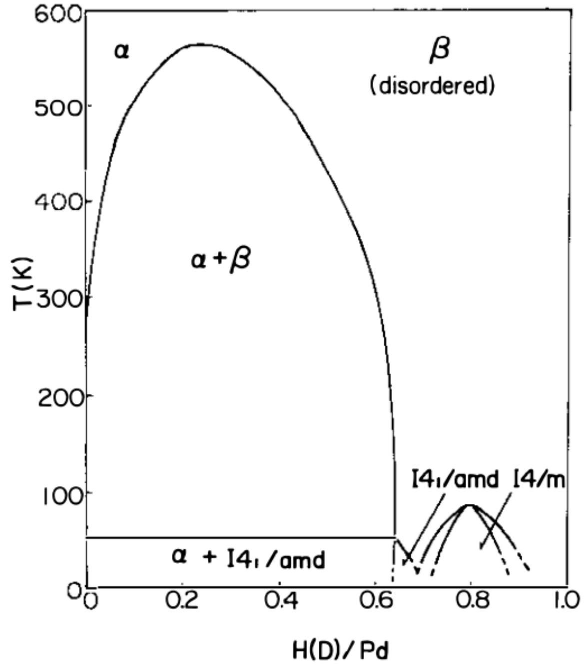

Fig. 3.1: *Phase diagram for the Palladium Hydrogen system showing the phases observed at different Hydrogen/Palladium atomic ratios (X-axis) and temperatures (Y-axis). Reproduced from [26]*

Palladium atoms (H/Pd), is about 0.0015, the Palladium lattice is in the α-phase with a marginally larger lattice constant of 0.3894 nm. At Hydrogen concentrations larger than 0.6, the lattice is in the β-phase with a lattice parameter of 0.4040 nm. For Hydrogen concentrations between 0.0015 and 0.6, co-existence of the α-PdH and the β-PdH phases is observed with a lattice parameter of about 0.4025nm. The transition from α to β phase is accompanied by a change in the lattice volume by around 10%. This large change stresses the Palladium film and can cause film embrittlement and fracture during Hydrogen absorption [27] as well as during electrochemical processes such as electrodeposition [4], as discussed in Chapter 2. In theory, the film should recover after removal from the Hydrogen atmosphere, but the phase change can be effectively "irreversible" if it causes physical damage of the Palladium film due to the volume change. The reliability of the sensor is therefore restricted to the pressure range where the film can withstand the physical stresses caused by Hydrogen absorption.

Everett *et al.* [28] studied the dissolution of Hydrogen into Palladium films as a function of the Hydrogen pressure and found a non linear hysteretic dependence as shown in Fig. 3.2. This figure summarises the curves from multiple experiments performed by cycling the Hydrogen pressure between different maximum and minimum limits. For the purposes of

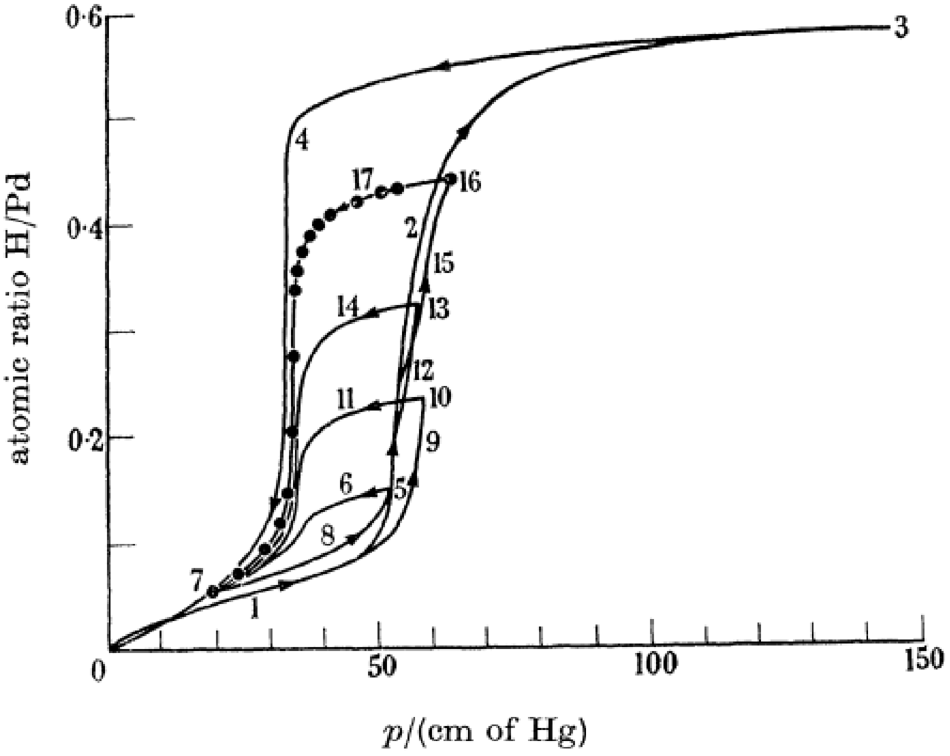

Fig. 3.2: *Dependence of the Hydrogen/Palladium atomic ratio on Hydrogen partial pressure in a Palladium sponge of mass 3 gm. The sudden increase in the Hydrogen/Palladium atomic ratio and the hysteresis between adsorption and desorption cycles is due to the α-PdH to β-PdH phase transitions. Reproduced from [28]*

this report, the largest hysteresis loop (points 0-1-2-3-4-0) is most relevant as it shows the variation of Hydrogen content in the Palladium for the widest pressure range. It can be seen from this loop that the Hydrogen concentration in Palladium shows a sudden increase at a pressure of around 50cm of Hg ($\approx$ 0.7 bar), which corresponds to the transition of the metal from α-phase to the β-phase. As the pressure is reduced, the reverse transition from the β to α phase is observed to occur at around 25 cm of Hg forming the hysteresis loop of Hydrogen concentration for the absorption and desorption processes. Everett *et al.* also observed that the time required for the Hydrogen content measurement varied with the location on the hysteresis curve. The data points on the steeply sloping part of the curve took upto 24 hours to reach equilibrium while the equilibrium was attained much faster (5 to 30 mins) in the saturated region of the curve above 90 cm of Hg.

The low Hydrogen pressure region in Fig. 3.2 (<20 cm Hg) is the most reliable as it avoids the hysteresis loop completely. At low Hydrogen pressures, the amount of Hydrogen dissolved in the Palladium metal is governed by Sievert's law, which states that the

Hydrogen concentration in the bulk of the film is proportional to the square root of the Hydrogen partial pressure in the system. This rule is used quite frequently to estimate the amount of gaseous Hydrogen dissolved in a metal film and to correlate the observed sensor signal with the dissolved Hydrogen concentration.

The effect of Hydrogen dissociation and dissolution on the electrical characteristics are explained by Wicke *et al.* [29]. The Palladium atom has unfilled 4d and 5s valence orbitals at the Fermi level with a higher density of 4d states than 5s ones. On entering the lattice, the Hydrogen electrons are delocalised by exchange interaction with the 4d states of the Palladium atoms and occupy the 4d electron states of the Palladium while the screened protons occupy the octahedral interstices of the Palladium lattice. The electrons fill the empty 4d and 5s states at the Fermi level and raise the Fermi level energy, reducing the Palladium work function. The rate of workfunction decrease is dependent on the concentration of Hydrogen in the Palladium, as the first Hydrogen electrons fill up the higher density 4d states, while the latter fill the lower density 5s states. The rate of workfunction decrease is therefore higher at high Hydrogen concentrations. This property, which would be desirable because it increases sensor speed, is counteracted by the phase change in Palladium that occurs at high Hydrogen contents. The screened protons exert an expansive strain on the surrounding Palladium atoms. This expansive strain creates a chemical potential for the screened protons that favours increased solubility at higher Hydrogen content in the metal, which explains the increase in absorbed Hydrogen for H/Pd ratios greater than 0.6.

The electrical characteristics of Palladium Hydride have been studied by incorporating Hydrogen into the Palladium film electrocatalytically via a solution [30] as well as via a gas phase [31]. The resistance of the Palladium hydride depends on its phase at the time of measurement and therefore on the Hydrogen concentration in the Palladium lattice. The resistance of the film increases almost linearly with increasing Hydrogen content throughout the α and $\alpha + \beta$ phase with a higher rate of increase in the α phase concentration range compared to the $\alpha + \beta$ phase. When the β-phase of the hydride is reached, the rate of change decreases further and for some samples, a decrease of resistance is observed with increasing Hydrogen concentration beyond this point. The hysteretic variation of Hydrogen content with Hydrogen pressure as shown in Fig. 3.2 results in the resistance characteristics also showing hysteresis [27, 31] as the Hydrogen desorbs from the Palladium film. This hysteresis in the electrical characteristics and the film embrittlement due to large volume changes during the α-PdH to β-PdH phase change restricts the pressure range over which pure Palladium sensors can function.

One way to overcome this limitation is to alloy Palladium with metals such as Silver, Lead, Nickel or Rhodium. The alloying metals have specific effects on the Palladium lattice due to their different atomic sizes and electronic configurations. Elements like Silver and Lead, with larger atomic sizes compared to Palladium, cause the Palladium lattice to expand, increasing the size of the octahedral interstices. The chemical potential of such a lattice favours a higher solubility of Hydrogen at lower concentrations and lower solubility at higher concentrations compared to pure Palladium. Modifying the solubility in this way can remove the non linearity caused by the phase transitions. Elements like Nickel and Rhodium on the other hand, which have smaller atomic sizes compared to Palladium, cause a contraction of the lattice and favour lower solubility at low Hydrogen content and higher solubility at higher hydrogen content compared to pure Palladium. This modification accentuates the non linear region, but pushes the critical pressure where the non linear transition occurs to higher pressure values. The alloying element will also affect the degree and rate of workfunction change on Hydrogen exposure. The rate will be increased by species that donate electrons to the 4d and 5s states of pure Palladium (Silver, Lead) and reduced by species that accept electrons from these states (Nickel, Rhodium) [29]. Extensive studies also describe the dependence of PdNi, PdRh [32] and PdAg [33] resistances with Hydrogen content. All these effects due to alloying could be used to tailor the sensing material for specific applications. The next section provides a brief overview of some reported Hydrogen sensors and the principles on which they are based.

3.3 Palladium based Hydrogen sensors

Exposure to Hydrogen changes physical and electrical properties of a Palladium or Palladium alloy film. The three primary properties on which a sensor can be based are the volume change of the Palladium lattice, the change in Palladium resistance and the change in Palladium workfunction on Hydrogen exposure. This section gives an overview of a few sensors described in the literature that are based on each of these three properties.

3.3.1 Sensors based on volume changes in Palladium and alloys

The change in Palladium film volume on Hydrogen exposure was used to fabricate a cantilever based Hydrogen gas sensor [34]. A glass cantilever of dimensions 24 mm×4 mm and with thickness of either 80 μm or 130 μm was coated with a Palladium or PdAg alloy on one side. Theoretically, the curvature of the Palladium cantilever was shown to be proportional to the ratio of Hydrogen to Palladium atoms in the film and for low pressures where Sievert's law is valid, it should be proportional to the square root of the Hydrogen partial pressure. The cantilever curvature roughly follows this relation for low Hydrogen pressures (below 30 Torr), but exhibits a wide departure from it for Hydrogen pressures above 30 Torr, corresponding to a phase change from α-PdH to β-PdH and the accompanying drastic volume change. Alloying with Silver was effective in reducing this non linearity but at the expense of reducing the overall response strength of the sensor. Being based on the same principle as a bimetallic strip, the magnitude of the curvature change can also be tailored by varying the Palladium/Palladium-alloy thickness as well as the thickness of the underlying glass substrate. The response of one cantilever consisting of 100 nm Palladium on 80 μm glass is shown in Fig. 3.3 for different Hydrogen pressures.

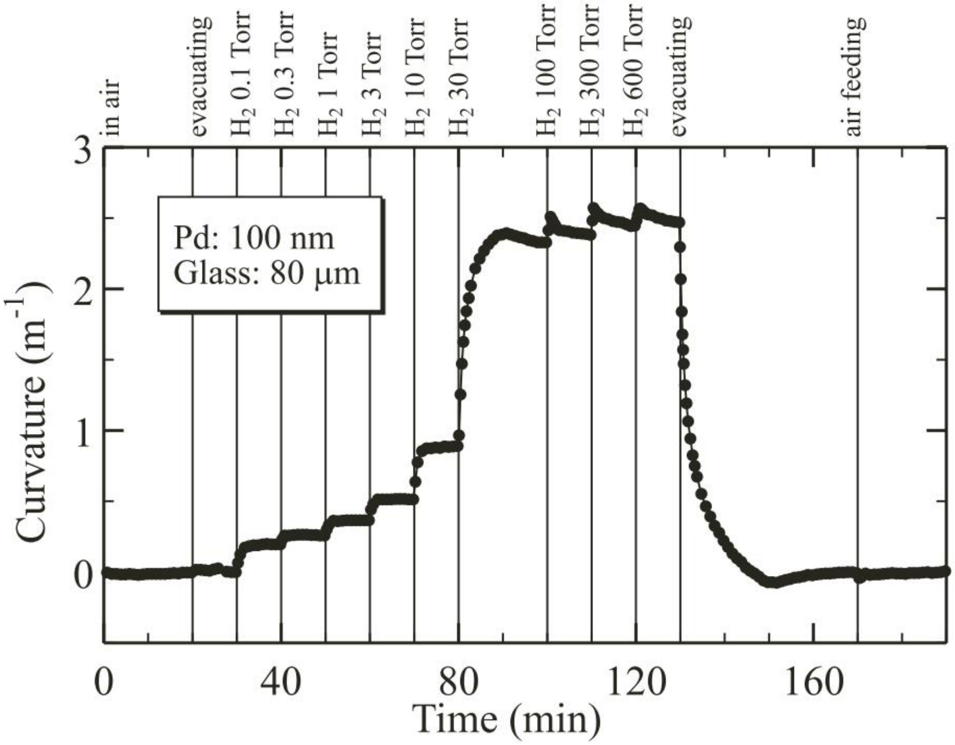

Fig. 3.3: *Curvature change of 100nm Pd/80 μm glass cantilever on exposure to Hydrogen gas. The large curvature change at 30 Torr is due to the large volume change during the α-PdH to β-PdH transition. Reproduced from [34]*

The sharp increase in curvature corresponding to the α-PdH to β-PdH phase transformation is observed at a Hydrogen pressure of 30 Torr. Fig. 3.3 shows that the changes in curvature are reversible and essentially shows that the film volume recovers after Hydrogen removal. This study found that for Hydrogen pressures above 10 Torr, the actual response of the sensor also deviated highly from the square root dependence on the Hydrogen pressure predicted by Sievert's law and thus it was claimed that the Pd/Glass film was suitable only for measuring Hydrogen pressures within the 0 to 10 Torr limits.

Fig. 3.4 shows a graph comparing the responses of sensors based on Palladium-Silver alloys with varying Silver content.

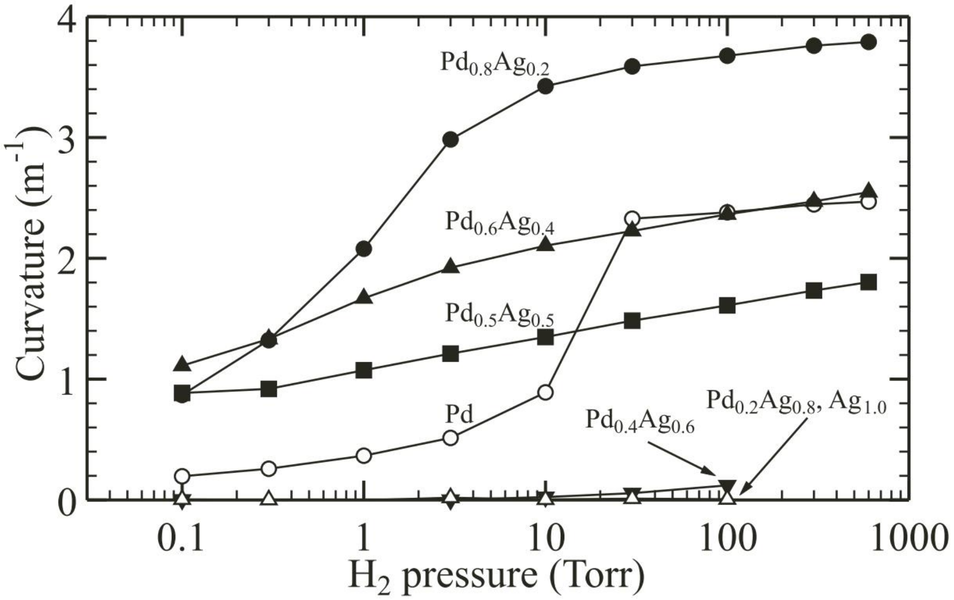

Fig. 3.4: *Curvature changes of 100 nm Pd_xAg_{1-x}/80 μm glass cantilever on exposure to Hydrogen gas. Alloying with Silver is seen to remove the sudden phase transition but also reduces the change in curvature. Reproduced from [34]*

By comparing the responses of $Pd_{0.8}Ag_{0.2}$ and $Pd_{0.5}Ag_{0.5}$ sensors, it can be seen that the Silver content in the film smooths out the Palladium phase change non linearity but also reduces the overall response strength of the sensor. An additional ill effect of alloying was the slowing down of the sensor response, possibly due to the reduced solubility of Hydrogen in the alloy film.

A device using the volume change property of Palladium in a completely different sensing mechanism is described in Ref. [35]. This sensor comprises of a Palladium mesoscopic wire array (PMA) fabricated by electrodepositing Palladium onto the step edges of Graphite. The electrodeposited Palladium wires consisted of multiple grains whose sizes were controlled by the deposition parameters. These sensors exhibited a decrease in resistivity on Hydrogen exposure, contrary to other studies involving Palladium films. This behaviour was attributed to the granular structure of the wires, wherein it was possible that two neighbouring grains did not actually form a physical contact and therefore had a high resistance. On exposure to Hydrogen, the individual Palladium grains swelled in volume as they absorbed Hydrogen and improved the electrical contacts along the entire length of the wire. The improved electrical contact between adjacent grains caused an overall decrease in the wire resistance, despite resistance increases in the individual grains. In some of the sensors, this effect was observed in the extreme, wherein the sensors behaved as an open switch in the absence of Hydrogen and changed into a conductor with measurable resistance on Hydrogen exposure. An atomic force microscope image in Fig. 3.5 of one of the Palladium mesowires illustrates the effect that causes these large resistance changes.

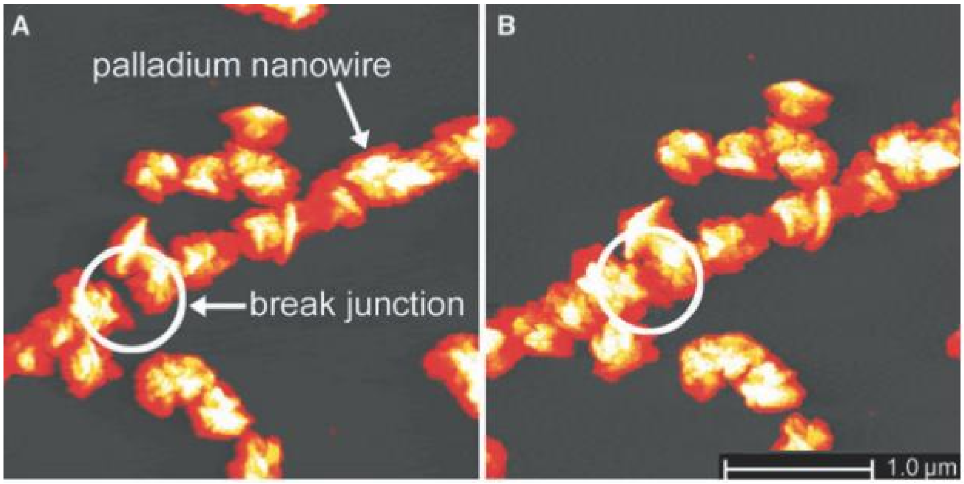

Fig. 3.5: *Sensor based on change of volume of individual grains in an electrodeposited Palladium nanowire. In absence of Hydrogen, the gaps between grains form break junctions and result in high nanowire resistance. An increase in volume on Hydrogen exposure closes the break junction and drastically reduces the nanowire resistance. Reproduced from [35]*

It can be seen from Fig. 3.5(a) that initially the Palladium wire is an open circuit as two neighbouring grains are not in contact with each other, causing a high resistance state. Upon exposure to and absorption of the Hydrogen in the Pd, the grain size increases and closes the gap between the two neighbouring grains, significantly reducing the wire resistance. This characteristic is useful for a certain class of power constrained devices such as battery powered Hydrogen leakage detectors because power consumption in the absence of Hydrogen is negligible and the device lifetime will be long. It is however, very difficult to accurately and reliably produce break junctions with the right dimensions to function as switches.

3.3.2 Sensors based on resistance changes in Palladium and alloys

Another sensing mechanism is to exploit the change of electrical resistance of a Palladium film on exposure to Hydrogen. Hughes *et al.* [27] describe a simple sensor formed from PdNi alloy thin films whose resistance was measured as a function of Hydrogen pressure and Nickel content in the alloy. Smaller sensor responses were measured at higher Nickel content and no response was observed in devices with Nickel content higher than 56%, suggesting this is the upper limit for the alloy that can be used as an active element of the sensor. A comparison of data from 100nm and 35nm films show that the resistance change is a bulk and not a surface effect. This illustrates that while the dissociation of the Hydrogen gas occurs only on the surface of the Palladium film, the dissociated Hydrogen atoms diffuse into the bulk of the film and form Palladium Hydride in the bulk of the film as well. This is an important observation for sensors based on Schottky barriers or metal-insulator-semiconductor structures as it proves that exposure to Hydrogen can affect the metal-semiconductor interface, which can then be used to sense Hydrogen pressure. Fig. 3.6 shows the responses of various Pd_xNi_{1-x} alloys as a function of the partial pressure of Hydrogen.

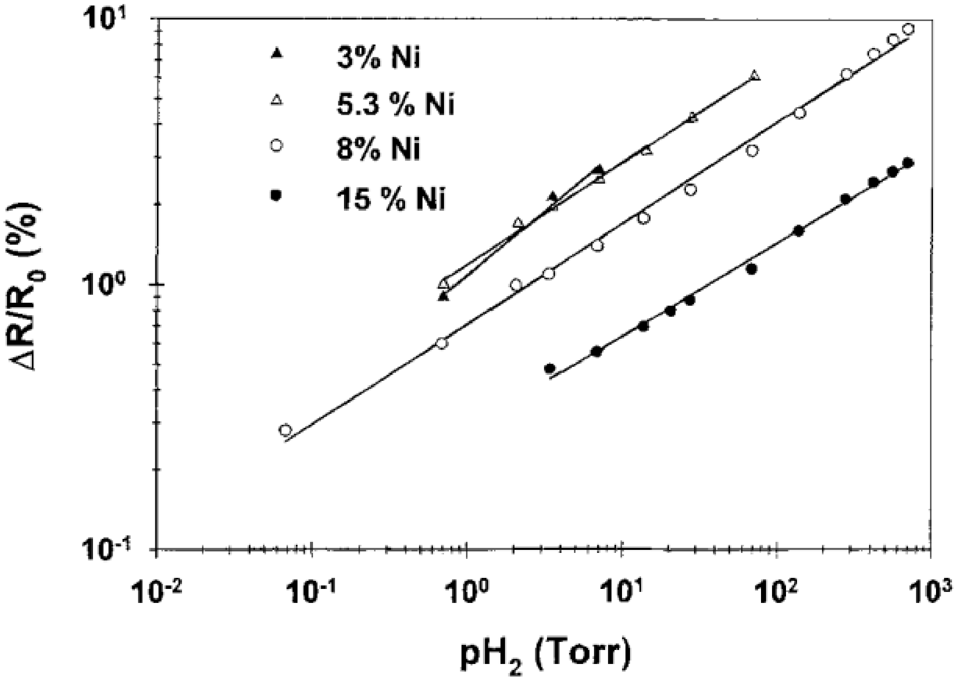

Fig. 3.6: *Normalised resistance change of PdNi alloys with varying Nickel concentration to different Hydrogen partial pressures. Reproduced from [27]*

The experimental data in Fig. 3.6 shows a power law relation between change in resistance and Hydrogen partial pressure, with the exponent value being 0.4. This shows a slight deviation of the PdNi alloys from the value of 0.5 expected from Sievert's law. The sensor reacted to changes in Hydrogen pressure in a few minutes and not significantly affected by ambient conditions. Alloying with Nickel delays the onset of the α-PdH to β-PdH phase transition from about 7 Torr [27, 29] for pure Palladium to about 100 Torr for $Pd_{0.92}Ni_{0.08}$ and thus increases the pressure range over which the sensor can operate reliably. However, a pronounced hysteresis loop as shown in Fig. 3.7 is still present as opposed to the Palladium-Silver alloys, where alloying led to an overall smoother response. The mechanical strength of the PdNi alloy allowed it to be cycled through Hydrogen absorption and desorption without damage but the presence of hysteresis restricts the pressure range of the sensor's operation.

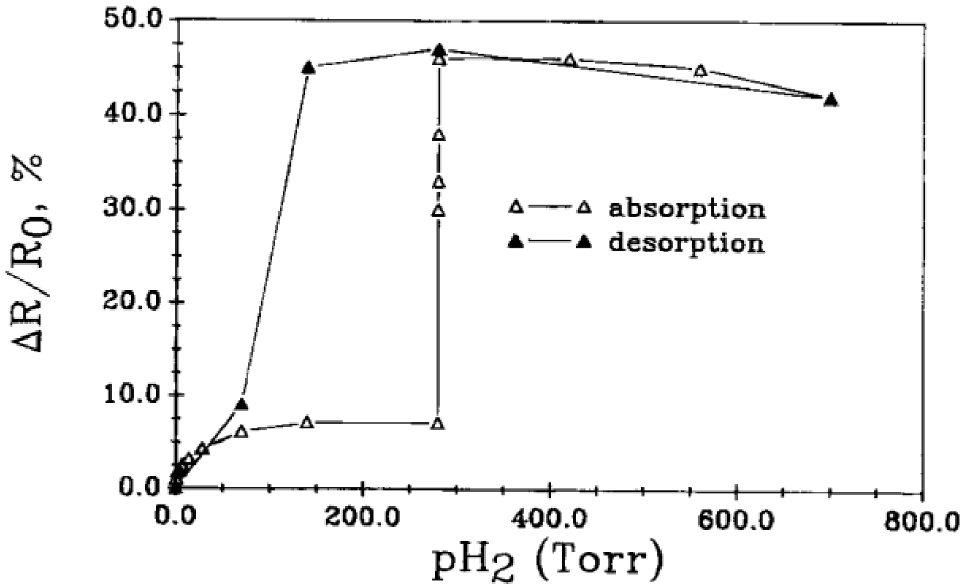

Fig. 3.7: *Hysteresis observed in the absorption-desorption cycle of a 50 nm $Pd_{0.95}Ni_{0.05}$ film at different Hydrogen partial pressures. Comparison with Fig. 3.2 shows that the change in resistance is correlated to the Hydrogen content of the film. Reproduced from [27]*

A more exotic implementation of a resistance change system was used by Kim *et al.* [36] to fabricate a device with vertically aligned Palladium nanowires whose resistance was measured in the vertical direction in the presence and absence of Hydrogen. An advantage of nanowire structures is the significantly larger surface area available for Hydrogen dissociation and absorption. In this device a net decrease of resistance was observed as the closely spaced nanowires swelled on Hydrogen absorption and formed contacts with their neighbours, effectively reducing the resistance of the entire nanowire forest. This sensor has fast response times, measurable in seconds as compared to other sensors with timescales over minutes. However, it does not offer significant power efficiency as the resistance of the Palladium nanowires is very similar to that of the bulk Palladium film and relatively large currents are drawn even in the idle state.

3.3.3 Sensors based on workfunction changes in Palladium

A third method for Hydrogen sensing using Palladium is to sense the change in the metal work function on Hydrogen exposure. Pd/Pt-semiconductor Schottky barriers or MOSFET structures with Pd/Pt as the gate material are the preferred architectures for such sensors. Kim *et al.* [37] studied the response of a Pt-ZnO Schottky diode to gaseous Hydrogen. After dissociation at the surface, the Hydrogen atoms diffuse through the metal film and reach the metal-semiconductor interface, forming a dipole layer at the interface which causes the rectifying behaviour of the contact to collapse and exhibit an ohmic characteristic. However, it was observed that the sensor recovery took much longer (>1 month) than for sensors based on a Pt-SiC or Pt-GaN Schottky barrier [38]. This discrepancy was attributed to Hydrogen atoms acting as shallow level dopants in the ZnO semiconductor, increasing the doping density of the semiconductor and consequently lowering the barrier height. The cumulative effect therefore has contributions from the dipole formation at the interface as well as the affinity of the semiconductor to be doped by the diffusing Hydrogen atoms and the recovery time is hampered by the speed of Hydrogen outgassing from the ZnO substrate.

Weichsel *et al.* [39] studied a Pd-ZnO Schottky diode grown on a layer of GaAs. In this sensor, Hydrogen lowers the Palladium workfunction and also contributes to barrier height lowering by acting as a shallow dopant in the ZnO. It is not possible to ascertain which of these competing mechanisms actually drive the sensor response, but a significantly faster recovery time ($\approx$ 17 hours) compared to the Pt-ZnO sensor [37], suggests that the dominant mechanism is the Palladium workfunction modification. While the time is an improvement over the Pt-ZnO sensor, it is still too long for commercial sensing, unless the sensor can be replaced after every individual measurement and allowed to recover.

Palladium workfunction changes are also used as the primary sensing mechanism in metal-oxide-semiconductor (MOS) or metal-insulator-semiconductor (MIS) sensors. The device can be structured and operated as a field effect transistor (FET) or a MOS capacitor. Lundström *et al.* [40] first described a field effect transistor structure with a thin layer of evaporated Palladium as the gate metal separated from the semiconductor by a 10nm oxide layer. Modification of the metal workfunction after Hydrogen exposure changes the threshold voltage of the FET. The device exhibited a decrease of the threshold voltage on introduction of Hydrogen and a recovery to its original value when the Hydrogen was removed. TaşaltIn *et al.* [41] describe a Pd/native nitride/n-GaAs MIS capacitor used to sense gaseous Hydrogen. The phenomenon driving the sensing mechanism is as in the MOSFET device described by Lundström *et al.* [40] except that the change in the MIS capacitance was sensed for varying Hydrogen concentrations. It may be possible to achieve low power operation of this sensor but capacitance measurement is a more complex procedure and use of this sensing structure will depend on the tradeoffs between the low power requirements and the complexity of the measurement circuit.

This section discussed a variety of sensors that exploit changes in different Palladium properties to measure Hydrogen concentration. Among these, the sensors with a Schottky barrier or MOS/MIS structure strike an attractive balance of low power consumption and design simplicity, both of the sensor and the allied circuitry. A back to back configuration as discussed by Wang *et al.* [42] also guarantees low power consumption at all polarities of applied potential. The Schottky barrier and MOS/MIS sensors described were fabricated using metallisation techniques like evaporation or sputtering that require relatively complex operating conditions. The PdNi-Si Schottky diodes fabricated in this project using the table top and non vacuum electrodeposition process have extremely low reverse bias currents (1 to 2 nA) and are therefore promising candidates for low power Hydrogen sensors. The use of Silicon as the substrate also simplifies integration with other electronic systems as compared to sensors using alternative substrates such as ZnO, GaAs or GaN. The following sections will describe the fabrication and characterisation of the electrodeposited PdNi-Si Schottky barrier Hydrogen sensor.

3.4 Electrodeposited PdNi-Si Schottky diode Sensors

3.4.1 Fabrication

The sensor in this work consists of a pair of back to back PdNi-Si Schottky diodes. This structure was chosen because it restricts the current consumption during a two terminal measurement to low values by always maintaining one of the Schottky diodes in reverse bias. In Chapter 2, electrodeposited PdNi-Si Schottky diodes were shown to have extremely low reverse bias currents, ensuring low power consumption in the idle state. Exposure to

Hydrogen changes the Palladium work function, lowers the Schottky barrier height and results in a corresponding rise in reverse bias current. However, since the Schottky diodes never go into forward bias simultaneously, the current is still restricted by the reverse bias currents of the modified Schottky barriers and power consumption remains relatively low for all Hydrogen pressures and applied biases.

The Schottky diode pairs were fabricated on a 2-inch, n-type, 0.5-1.5 Ω.cm ⟨100⟩ Silicon wafer by the fabrication process illustrated in Fig. 3.8. All the wafers were cleaned with fuming Nitric acid and a 50nm thermal oxide was grown on the surface. Photolithography was used to define the patterns of the Schottky diodes, following which, the oxide in the exposed windows was etched away by a 20:1 HF etch. A 50 nm thick $Pd_{0.71}Ni_{0.29}$ film was electrodeposited into the etched oxide patterns using the remaining oxide and photoresist as a mask. After electrodeposition, the resist was washed away and a second photolithography step was performed to define the Aluminium wiring and contact pads. The final step was the evaporation and lift off of a 100 nm Aluminium layer. An optical microscope image of the finished chip is shown in the final pane of Fig. 3.8. The PdNi and Aluminium areas are marked and the dark background is the Silicon oxide. The chip has a total of twelve Schottky diode pairs with different areas and exposed lengths of the PdNi film to study

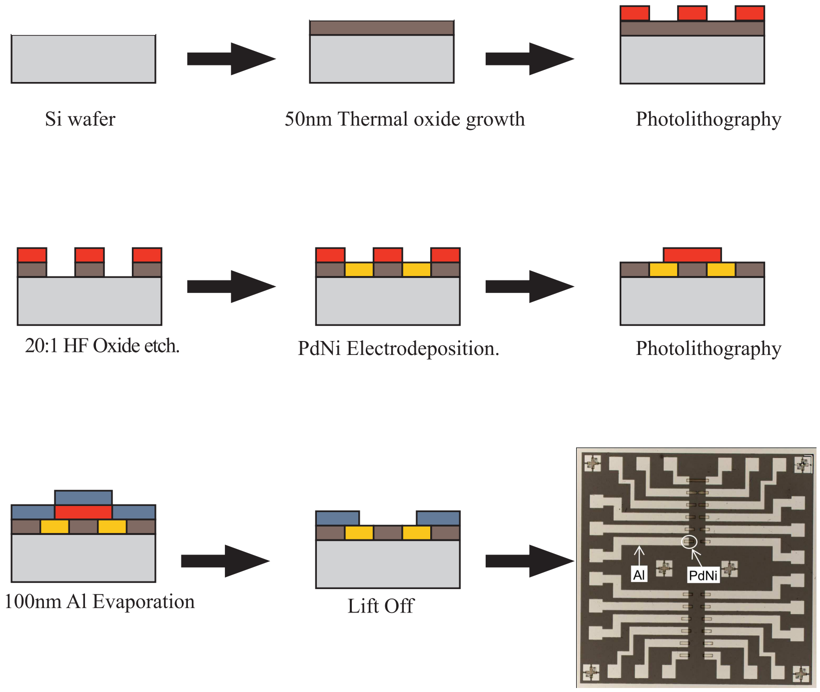

Fig. 3.8: *Fabrication process for back to back Schottky diodes for Hydrogen sensing.*

the dependence of the sensor characteristics on these parameters. The alloy was calculated to contain 29% Nickel on the basis of the electrodeposition potential employed. When the density of the sensor active elements is low, as in this case, electrodeposition results in significant cost benefits because it eliminates the lift off step for Palladium, where a lot of the metal film is wasted.

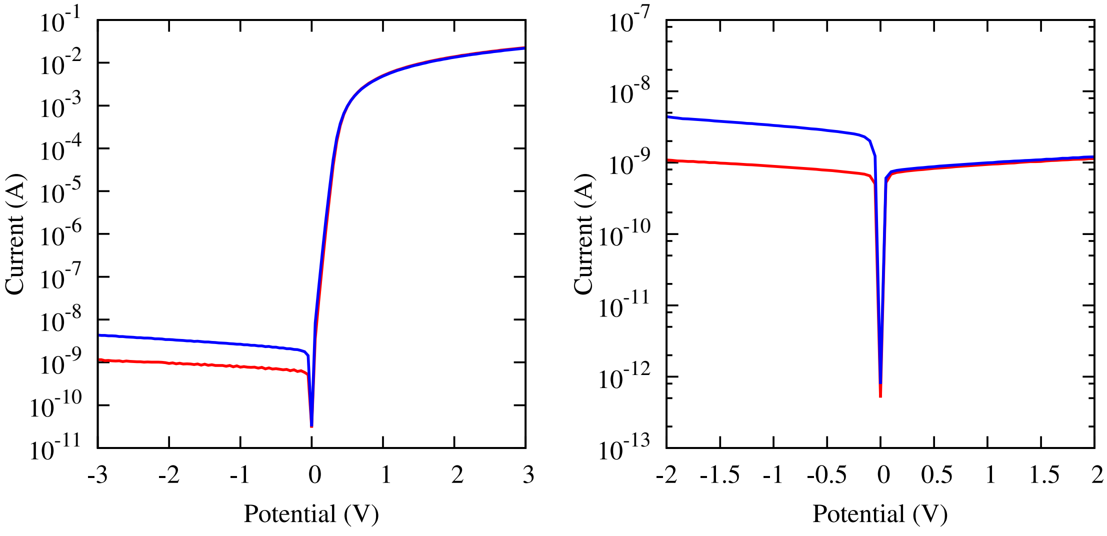

(a) (b)

Fig. 3.9: *(a) Electrical characteristics of individual* $Pd_{0.71}Ni_{0.29}$*-Si Schottky barriers. (b) Characteristics of the same* $Pd_{0.71}Ni_{0.29}$*-Si Schottky diodes in a back to back architecture.*

Initial electrical measurements were performed on the fabricated back to back sensors using a DC prober and Agilent 4155C semiconductor parameter analyser. The I-V characteristics of the PdNi-Si Schottky barriers for two devices in the absence of Hydrogen are plotted in Fig. 3.9(a). Fig. 3.9(b) shows the back to back characteristics of the same two devices in the absence of Hydrogen. It can be seen that back to back diode architecture restricts the idle current of the device to extremely low values for positive and negative ranges of the applied bias.

3.4.2 Electrical characterisation in a Hydrogen ambient

The Hydrogen ambient for the electrical characterisation was created using the vacuum chamber of a Lakeshore EMTTP4 probe station with a Hydrogen and nitrogen gas supply. The schematic of the system is shown in Fig. 3.10. After evacuation, the chamber can be pumped with either pure Nitrogen by opening valves V2, V3 and V4. The 5% Hydrogen-

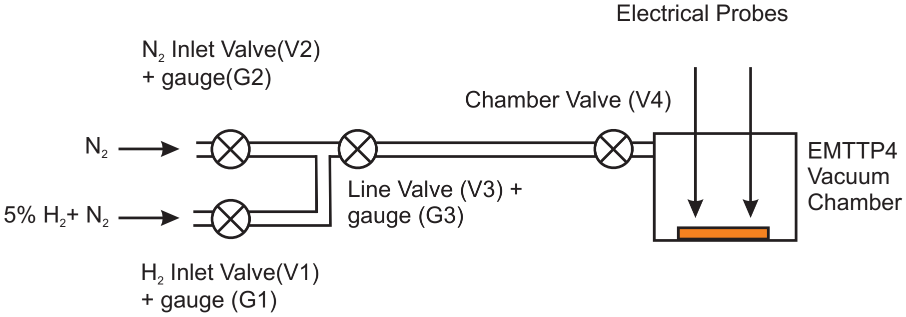

Fig. 3.10: *Schematic of the system used to created Hydrogen ambients in a vacuum chamber. V1-V4 are the valves at different points on the system and G1-G3 are pressure gauges used to read pressure of the gas sources or the chamber.*

Nitrogen mixture is introduced by opening valves V1, V3 and V4. The pressure of gases inside the chamber can be read from gauge G3 when V3 is closed and V4 is left open. The smallest pressure increase possible is equivalent to the volume of one line (between V3 and V4) of gas introduced into the chamber. For the Hydrogen-Nitrogen mixture, this was found to be around 5 mbar, which corresponds to a Hydrogen partial pressure of 250 μbar. This value will be affected by variations in the Hydrogen input pressure. In this case however, the Hydrogen source was a cylinder whose pressure output remained constant (1.5 bar) over the course of these experiments and therefore the value for the pressure increase from one line of gas is reliable. Using the line pressure to pump up the chamber was very time consuming due to the large chamber volume and also the need to open and close multiple valves to input each line and therefore this method was used only to measure the lowest pressure that the sensor can detect. For other experiments, the chamber was pressurised by leaving V3 and V4 open, while opening either V1 or V2 for an empirically determined duration.

The device was loaded into the vacuum chamber and the chamber was evacuated to a pressure of 1.5×10^{-2} mbar. It was then pressurised to 0.2-0.3 bar with pure Nitrogen to form a base pressure and to further dilute the 5% Hydrogen-Nitrogen mixture that was used for device measurement. The Hydrogen-Nitrogen gas mixture was then introduced into the chamber in steps which varied with the individual measurements. The smallest pressure step of about 5 mbar was used to find the lowest pressure that could be sensed. Otherwise, a pressure step of about 0.1 bar was used to speed up the measurements. The partial pressures of the Nitrogen and Hydrogen-Nitrogen mixture were used to calculate the partial pressure of pure Hydrogen in the chamber. Once the Hydrogen ambient was created, the device was contacted by the probes and electrical measurements were performed using an Agilent 4155C semiconductor parameter analyser.

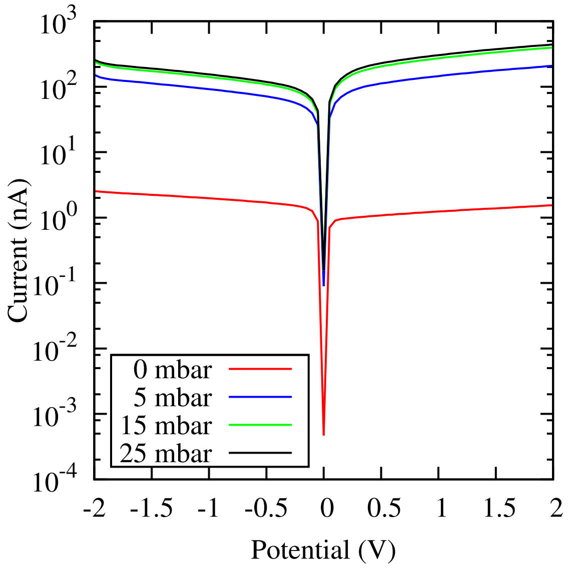

Fig. 3.11: *I-V characteristics of back to back* $Pd_{0.71}Ni_{0.29}$*-Si Schottky diodes at different Hydrogen pressures. The current variation shows the high sensitivity of the sensor to Hydrogen pressure.*

The steady state I-V characteristics of a back to back Schottky diode pair on exposure to different Hydrogen gas pressures are shown in Fig. 3.11 and they show that in the absence of Hydrogen, the Schottky diode pair draws only a few nanoamperes of current. Exposure of the sensor to the first step increase of the Hydrogen-Nitrogen mixture causes the current to increase by about two orders of magnitude. Subsequent additions of Hydrogen result in progressively smaller current rises, which suggests that the first introduction of Hydrogen is sufficient to cause a workfunction change for most of the PdNi alloy in direct contact with the Silicon, thereby causing the largest current increase. Since the reverse bias current is virtually constant, a bias voltage of -1V was chosen for all subsequent electrical measurements. Due to the symmetric device architecture, the polarity of the bias is immaterial and any potential that does not cause breakdown can be used.

The lowest Hydrogen pressure that this sensor can detect can be found by examining the device response to successive small step increases of Hydrogen pressure and noting the pressure at which the current change in the device is discernible. Data from one trial is shown in Fig. 3.12, where each arrow marks an increase in the Hydrogen partial pressure by 250 μbar on a pure Nitrogen base pressure of 0.3 bar. The plot shows that the current in the device increases rapidly after a Hydrogen partial pressure of 3 mbar, showing that a

Hydrogen partial pressure above 3 mbar can be easily detected using this device.

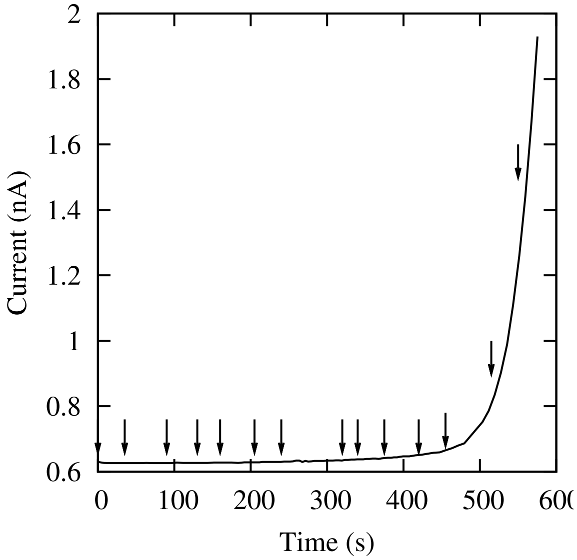

Fig. 3.12: *Response of $Pd_{0.71}Ni_{0.29}$-Si Schottky diode Hydrogen sensor to low Hydrogen pressures. Each arrow denotes an increase of the Hydrogen partial pressure by 250 μbar.*

On introduction of Hydrogen, large percentage increases in the device current are observed, but the sensor current takes a very long time to stabilise and in fact, the rate of current increase remained at a small positive value even after about 60-75 minutes in the Hydrogen atmosphere. The slow saturation of the sensor response is quite common and is also observed in other devices reported in the literature [37, 39]. Flanagan *et al.* [26] report the value of Hydrogen diffusion through the Palladium film as $D_H = 3.8 \times 10^{-11}\mathrm{m}^2/\mathrm{s}$ and calculations suggest that the Hydrogen should diffuse through the entire PdNi film in about 30s, significantly shorter than the time scales involved in this experiment. One explanation for this slow stabilisation may be that the surface of the PdNi film has developed an oxide layer or is covered by some remnant photoresist from previous processing steps that hampers the dissociation of the Hydrogen gas on the PdNi surface and slows down the remainder of the absorption process. Sensor recovery also took a long time and the devices usually had to be left in an air ambient overnight (≈8-12 hours) for the current levels to return to their original values.

This long stabilisation time causes a few problems in the sensor current measurement because the current measured for a particular device depends on the time between the Hydrogen introduction and the measurement of the sensor current. In addition, a limited number of probes made it necessary to measure the sensor response of each of the twelve

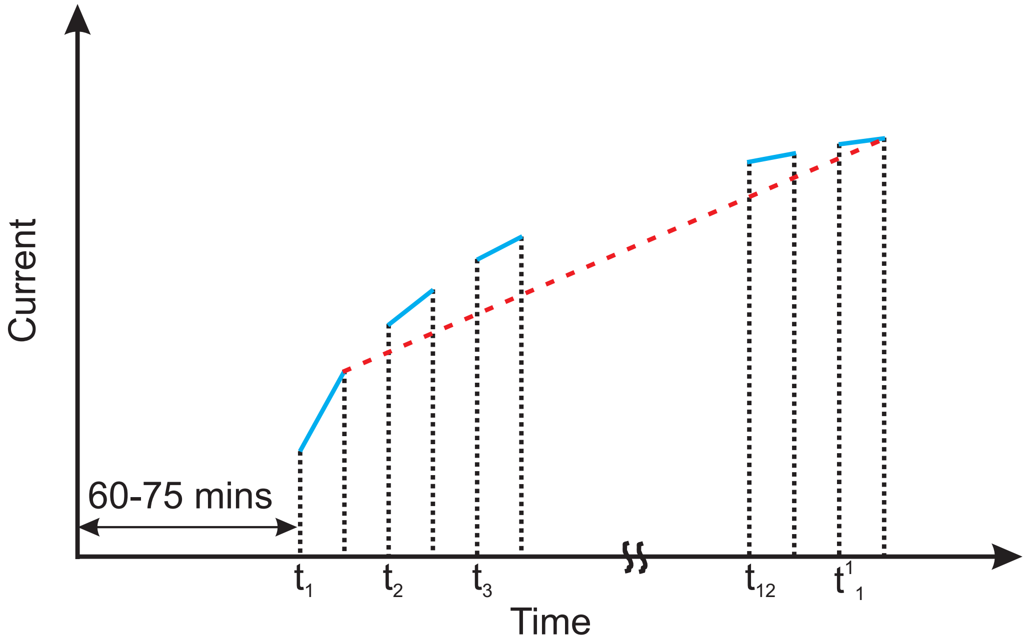

Fig. 3.13: *Measurement protocol for Hydrogen pressure sensor devices. The marked times depict the start of sampling time for each sensor measurement. The blue lines denote the constant sampling duration for each sensor. The first device was measured again at the end (t_1^1) and the red dashed line denotes the assumed linear growth of the current over the time required to measure all devices. The current compensation can be calculated using the slope of this line and the elapsed time since measurement of the first device. Axes are not to scale.*

sensors serially and meant that some sensors were exposed to the Hydrogen gas longer than others. To minimise these problems a measurement protocol was developed and is explained with the aid of Fig. 3.13. First, the sensors were allowed to rest in the Hydrogen ambient for around 60-75 mins as shown in the initial part of the time axis in Fig. 3.13 before the measurements were started, allowing the rate of current growth to reach a low value. The electrical current at -1V for each sensor was then sampled for 180 seconds at a rate of 1 sample/second and the mean of the last 120 samples was used to calculate the current at the particular Hydrogen pressure. The sampled data are depicted by the blue lines in Fig. 3.13 and the times t_1, t_2 and t_3 denote the start of the sampling period for the first, second and third sensor and so on. The remaining sensors are then measured serially using the same sampling and averaging technique, all the while noting the elapsed time. After all the devices were measured once, the first device was measured again (time t_1^1) to note the change in its current over the time taken to measure all twelve sensors on the chip. By assuming that the change in the current of the first device was linear (shown by the dashed red line) over the measurement time period, the slope was calculated and the current measured for each sensor was compensated based on the time difference between its measurement and that of the first sensor. For a first step increase in Hydrogen pressure from 0 to 5 mbar, the rate of current increase after leaving the sensors undisturbed in the Hydrogen environment for about 60 to 75 mins was found to be about 6 pA/s. This value meant that over the 1 hour duration normally required to measure all twelve devices on the chip, the current of the final few devices could have increased by upto 22 nA. However, all the devices that required large compensations already exhibited very large currents (≈ 150nA) and the compensation was not large enough to explain differences in currents between the individual sensors. For subsequent step increases of Hydrogen, the required compensation was even lower as current increases were also significantly lower compared to the first step in Hydrogen pressure, as seen in Fig. 3.11. For these reasons, the effect of the slow increase of device current even after 60-75 mins in the Hydrogen environment was ignored and all current values were reported as measured.

Fig. 3.14 shows the currents measured in three sensors for the entire range of Hydrogen partial pressures tested during this work. The sensor current shows a large increase at lower Hydrogen pressures but saturates for Hydrogen partial pressures above 15 mbar. The sensitivities of the sensors were calculated from the slope of the linear region and lie between 17.27-6.75 nA/mbar. The lines in the graph denote the fit of the datapoints using

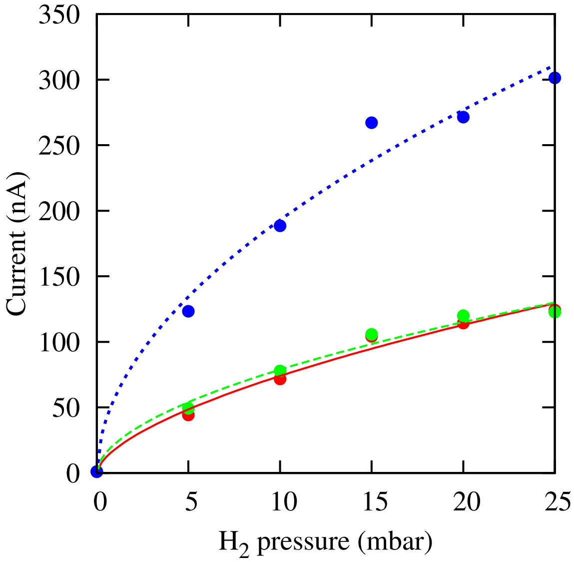

Fig. 3.14: *Dependence of the current measured in three different devices with Hydrogen gas pressures. The lines show the fits of the equation $I = Kp^n$ to the datapoints where K and n are fitting parameters.*

the equation

$$I = Kp^n \tag{3.1}$$

where I is the current, p is the Hydrogen partial pressure and K and n are fitting parameters. The value of the exponent n is computed to be 0.61, 0.55 and 0.52 for the three sensors and are close to the expected value of 0.5 from Sievert's law [26, 27]. As Sievert's law relates the Hydrogen concentration in the film to the Hydrogen partial pressure, the agreement with Sievert's law indicates that the current through the device is proportional to the Hydrogen concentration in the PdNi film.

The change in the Schottky barrier heights can be estimated from the thermionic emission theory described in Chapter 2. The barrier heights for all devices were measured to be in the range of 0.66-0.68V with ideality factors between 1.11-1.19. The low ideality factors show that thermionic emission is the dominant mechanism for the Schottky barrier conduction.

On exposure to Hydrogen gas, the Schottky barrier height changes, causing a change in the current through the device. The current through a reverse biased Schottky barrier is given by the formula

$$I = -AA^{*}T^{2}\exp\left(\frac{q\phi_B}{kT}\right) \tag{3.2}$$

where A is the area of the metal-semiconductor contact, A^{*} is the Richardson constant, T is the absolute temperature, q is the electronic charge and ϕ_b is the Schottky barrier height. The change in the Schottky barrier can be estimated by calculating the ratio of the currents before and after exposure to Hydrogen.

$$\frac{I_1}{I_2} = \exp\left[\frac{-q(\phi_{B1} - \phi_{B2})}{kT}\right] \tag{3.3}$$

where I_1, ϕ_{B1} are the current and the Schottky barrier height before exposure to Hydrogen and I_2, ϕ_{B2} are the current and Barrier height after Hydrogen exposure. Using Eq. 3.3 the changes in the Schottky barriers for the devices plotted in Fig. 3.18 were calculated to lie between 80-117 mV at 10 mbar Hydrogen pressure and between 91-126 mV for 20 mbar Hydrogen pressure.

The devices were subjected to multiple cycles of Hydrogen exposure and measurement and although stabilising and recovery times were slow, no irreversible changes were observed. This is expected since the Hydrogen pressure range over which this device was measured is lower than the pressure at which hysteresis is observed in $Pd_{0.95}Ni_{0.05}$ films

(≈400 mbar as seen in Fig. 3.7). Also the sensors measured in this project have a higher Nickel content (29%) and should therefore have a higher pressure threshold before an irreversible phase change becomes a hazard. The presence of Nickel in the alloy should also make the alloy film robust enough to withstand the phase transformation of the Palladium lattice and maintain sensor reliability even at higher Hydrogen pressures.

3.4.3 Time response of the Hydrogen sensor

The probe tips on the EMTTP4 probe station suffered large displacements during any changes in the vacuum chamber pressure. This made it impossible to measure the current during a change in Hydrogen pressure using the device fabricated as per Fig. 3.8 because the contact pads were too small to maintain contact after the probe movement. To perform some in situ transient measurements, a separate sensor was fabricated by marking out the Schottky barrier and large Aluminium contacts by hand using an insulating varnish. The film dimensions were not very well controlled as the aim of this sensor was only to obtain the transient response after the introduction of Hydrogen into the chamber. The sensor was placed in the vacuum chamber which was then pressurised with 0.4 bar of pure Nitrogen before the first step increase of Hydrogen gas. The response of the device is shown in Fig. 3.15.

The initial low current section of the curve in Fig. 3.15 shows the response of the sensor to evacuation of air from the chamber and the introduction of Nitrogen. It can be seen that hardly any response is observed during these events, showing that the sensor response to gaseous Nitrogen is extremely small. A 5 mbar step increase in Hydrogen partial pressure was introduced at around 180 s and is accompanied by a rapid increase in the sensor current. The film area of this sensor was significantly larger than the sensors described earlier and this is the reason for the higher current. The transient curve also illustrates the large saturation time for the device.

Fig. 3.16 is a continuation in time of the measurement depicted in Fig. 3.15 and shows the transient response of the same device to multiple step increases in Hydrogen pressure as well as some step increases in the Nitrogen pressure. The shape of the response to each Hydrogen pressure increase is similar to the transient response in Fig. 3.15 but with a smaller magnitude, indicating a saturation of the workfunction change with increasing Hydrogen pressure.

The Nitrogen partial pressure was increased by steps of 250 μbar at 14,15 and 18 minutes as denoted by the arrows in Fig. 3.16. The lack of any electrical response further highlights

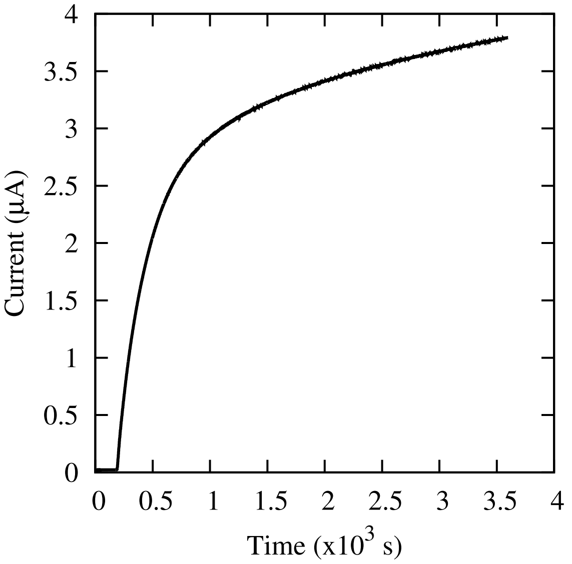

Fig. 3.15: *Response of PdNi film to a single step increase in Hydrogen partial pressure by 5 mbar.*

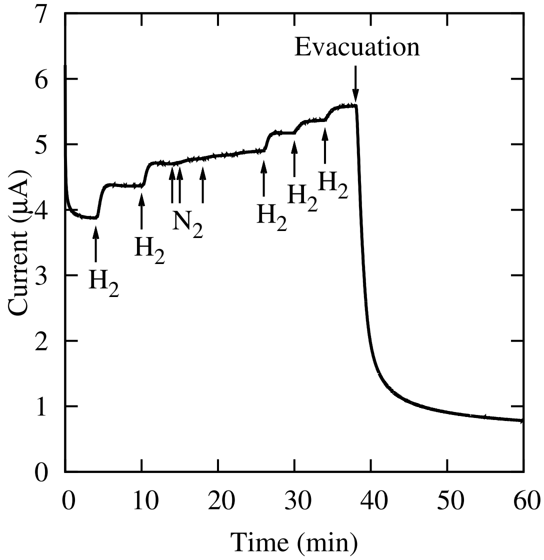

Fig. 3.16: *Response of PdNi film to multiple changes in Hydrogen partial pressure. This measurement continues from that in Fig. 3.15. The arrows and labels denote increases in the Hydrogen or Nitrogen partial pressures by ≈5 mbar each. It is seen that the sensor shows high selectivity by responding to Hydrogen inflow but not to Nitrogen.*

the selectivity of the sensor to Hydrogen compared to Nitrogen. Evacuation of the chamber was started at ≈ 38 mins and was continued till a final pressure of 3.8×10^{-3} mbar. Fig. 3.16 shows a rapid fall in the current, though the final current value is still about two orders of magnitude higher than the original current at which the trial began. The value of the current dropped back to the original level when the device was left in an air atmosphere overnight and thus the sensor can be said to have a recovery time of at least a few hours.

The chips fabricated by the process in Fig. 3.8 were designed to contain pairs of PdNi-Si Schottky diodes with different exposed areas of the electrodeposited PdNi films. The aim was to investigate how differences in the exposed areas, which act as sites for dissociation and absorption of Hydrogen affect the performance of the sensors. The rates of increase of current after exposing three Schottky diode pairs to Hydrogen were measured and are plotted in Fig. 3.17 and show that while the sensor reacts to low Hydrogen pressures and ultimately exhibits a large current change, the current does not stabilise for a long time and the current-time traces have a small slope even 40 to 50 mins after Hydrogen introduction.

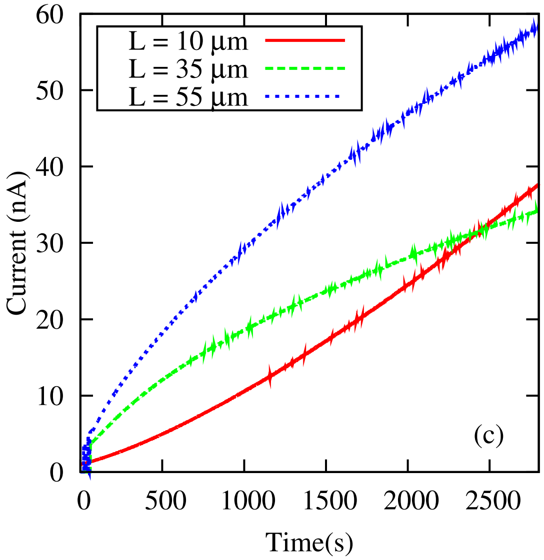

Fig. 3.17: *Rates of current increase for three devices with different exposed* $Pd_{0.71}Ni_{0.29}$ *areas on exposure to Hydrogen gas. The variable "L" is the exposed length of the sensing element. Devices with larger exposed areas show a faster increase in current than the ones with smaller exposed areas.*

The values of current measured by this method for devices with different exposed lengths of the PdNi film and for different Hydrogen pressures is shown in Fig. 3.18. Contrary to expectations, the devices with the smaller exposed lengths of film showed larger current increases on Hydrogen exposure compared to those with larger exposed areas of the PdNi

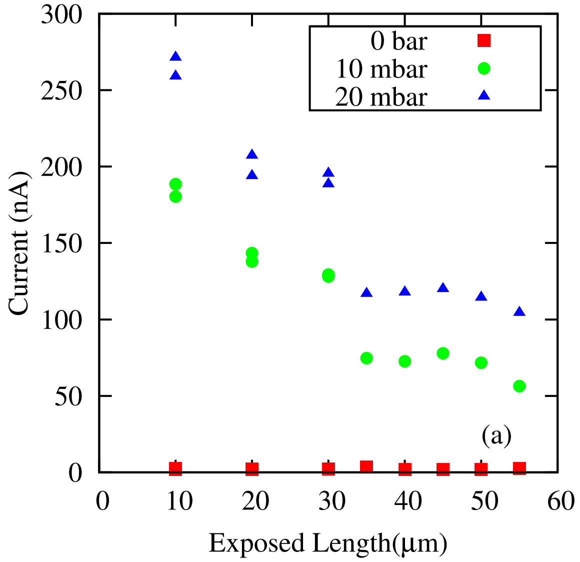

Fig. 3.18: *Dependence of device current on the exposed length of the* $Pd_{0.71}Ni_{0.29}$ *sensing element. The variable "L" is the exposed length of the sensing element.*

films. This is explained by the long settling time the devices are allowed before the steady state value is measured. This time is sufficient for the Hydrogen gas to diffuse through the entire film, including the film covered by the Aluminium wiring. The current response of each device therefore depends only on the total area and the nature of the individual PdNi-Si interface and not on the area exposed to the gaseous Hydrogen. This explanation is further supported by examining the rates of current increase for three devices with different exposed lengths shown in Fig. 3.17, which shows higher initial rates of current rises for sensors with larger PdNi exposed areas. The amount of Hydrogen dissociated and absorbed in the initial stages is therefore proportional to the exposed film areas but with the passage of time, this difference tapers out and the current levels in all sensors take similar values. This shows that the Hydrogen dissociates and is absorbed into the film only through the exposed PdNi and in the long term it diffuses through the entire film and nullifies the variation in exposed PdNi areas. Fig. 3.17 only shows traces till $\approx$ 40min and the sensors with exposed lengths of 35 μm and 55 μm provide good examples to show how the effect of the exposed film areas is nullified with time. For most of the measurements the devices remained exposed to Hydrogen gas for $\approx 70 - 75$min and therefore the effect of the exposed areas can be neglected.

Fig. 3.16 shows how a packaged sensor based on PdNi-Si Schottky barriers will react to Hydrogen pressure changes. The sensing circuitry will have to identify the areas of the curve with large slope as points where Hydrogen pressure increased and areas with small slopes as steady state electrical signals that can be used to identify Hydrogen pressure. The ability to detect low Hydrogen partial pressures means that this device can be used as a Hydrogen detector in its current form, with a binary output that can trigger an alarm or other warning system. This sensing mechanism exhibits large current changes but the slow response is the most significant problem that needs to be tackled for this sensing technique to be commercially valuable. One way to speed up the sensor response could be to use a thinner film, but this will not cause a large speed improvement as the diffusion time through the current film thickness of 50nm is many orders of magnitude larger than the theoretical values and a large thickness reduction will be required for significant speed improvement. Developing a process to clean the PdNi film surface of any oxides or impurities may improve response speed by facilitating the dissociation and diffusion of Hydrogen through the metal film. A third method is to perform the sensing and desorption at elevated temperatures. Higher temperatures reduce the solubility of Hydrogen in the Palladium film [27, 29] and while this could lead to smaller signal changes, it may also lead to an improvement in response time as equilibriums may be attained faster.

A comparison between the electrodeposited PdNi-Si Schottky barrier sensor presented in this work and other sensors, some commercially marketed and others still in the R&D phase, is shown is Table. 3.1. This includes the typical values for the power consumption and the response speeds of the sensors. Table. 3.1 shows that the Hydrogen sensor described in this work compares favourably with both commercial and research stage sensors in terms of power consumption. The closest competitor in terms of power is the device described

Table 3.1: *Comparison between Hydrogen sensor presented in this work with other sensors available commercially or reported in the literature. Typical values for the power consumption and response time are included.*

Sensor	**Reference**	**Development Stage**	**Power Consumption**	**Response Speed**
KHS-100	Ref. [43]	Commercial	Max. 25 mW	≈15s
Neodym Protisen	Ref. [44]	Commercial	≈ 750 mW	≈ 10 s
RKI Sensors	Ref. [45]	Commercial	≈ 250 mW	≈ 10 s
Favier *et al.*	Ref. [35]	Research	≈ 100 nW	≈ 500 s
Ruths *et al.*	Ref. [46]	Research	≈ 50 μW	≈ 20 mins
Wang *et al.*	Ref. [42]	Research	≈ 900 μW	≈ 10 mins
Usgaocar *et al.*	This work.	Research	≈ 200 nW	≈ 50-60 mins

by Favier *et al.* [35], which is based on the change of Palladium volume to cause improved contact between grains of an electrodeposited Palladium nanowire. The fabrication of the nanowire device though is more complex than the Schottky barrier based device described in this work. The electrodeposited PdNi-Si Schottky diode device therefore has a good balance of fabrication simplicity and low power consumption. The PdNi-Si Schottky barrier is also extremely selective to Hydrogen and is reusable, which are further advantages for commercialisation.

As seen in Table. 3.1, the response speed of the electrodeposited PdNi-Si Schottky barrier based sensor is a significant problem in this sensing technique. Improvements to the response speed from techniques previously discussed will make this sensing technology commercially competitive.

3.5 Conclusion

This chapter describes the theory behind the effect of Hydrogen on Palladium films and some of the methods in which these effects has been exploited in the construction of Hydrogen sensors. Among the different available sensing mechanisms, those involving Schottky barriers or MOSFET structures are most suited to low power sensing and are also advantageous due to their simple design.

A sensor based on back to back PdNi-Si Schottky diodes is presented. The fabrication process and electrical characterisation of the sensor are described. The novelty of this sensor lies in the use of electrodeposition as the metallisation process in place of traditional methods like evaporation or sputtering. The electrodeposition process described in Chapter 2 was used to deposit a 50nm $Pd_{0.71}Ni_{0.29}$ film to form a Schottky barrier with Silicon. The sensor comprised two back to back Schottky diodes that restricted the current to low values for all Hydrogen pressures and applied potential polarities. Idle currents of between 1-2 nA were observed, which are significantly lower than most sensors reported in the literature.

The Hydrogen sensor shows a large percentage increase for the first step increase of Hydrogen pressure and progressively smaller increases for subsequent pressure rises as the PdNi workfunction change starts saturating. The sensor is highly selective to Hydrogen and no response was observed for Nitrogen and air. The sensor is capable of detecting low Hydrogen pressures of about 3 mbar and the sensitivity of all the devices was found to lie between 17.27 and 6.75 nA/mbar. The change in current on Hydrogen exposure follows a power law with an exponent close to 0.5, as expected from Sievert's law. The current through the device is therefore proportional to the Hydrogen concentration in the film. The sensor currently has a slow response and recovery time and improving these times through cleaner metal films or elevated temperatures can constitute future research on this device.

4. CARBON NANOTUBE-PDNI CONTACT CHARACTERISATION

This chapter describes the characterisation of PdNi contacted Carbon nanotubes (CNTs) by modulating the workfunction of the PdNi contacts via Hydrogen exposure. The growth, structure and electronic properties of CNTs are briefly reviewed, followed by a description of the electrical and Raman spectroscopic techniques used to characterise the CNTs. The PdNi contacted CNTs exhibit ohmic characteristics, as expected due to the high workfunction of both Nickel and Palladium. The CNT current changes due to Hydrogen exposure are analysed and a method for differentiating between semiconducting and metallic CNTs is demonstrated. Raman analysis of the same CNTs is presented and the deduced CNT character is compared with the conclusions drawn from electrical characteristics in Hydrogen. A match is observed between the two results and the theoretically assigned CNT Raman features are thus experimentally verified.

Results in this chapter have been submitted to Journal of Applied Physics.

4.1 Introduction

Carbon nanotubes (CNTs) are an allotrope of Carbon that occur as tubes with high aspect ratios and walls of monoatomic thickness. They exhibit some remarkable physical, thermal and electronic properties which have made them the subject of much research focussed on employing them for different applications. This chapter describes some of the important electronic properties of CNTs and the formation of metal-CNT contacts for use in electronic devices. Difficulties in doping or otherwise changing the CNT bulk properties means that control via metal-CNT contact modulation plays quite an important role in CNT electronics.

This chapter describes the electrical characterisation and Raman spectroscopic analysis of CNTs contacted with electrodeposited PdNi. The modulation of PdNi-CNT contacts by changing the metal workfunction via exposure to Hydrogen instead of the electrostatic modulation of the CNT energy bands is described. PdNi was chosen as the contact material because Palladium is known to form good contacts with CNTs and also because PdNi films exhibit a decrease in workfunction on exposure to gaseous Hydrogen. Experimental data from electrical characterisation is correlated with the Raman spectra from the same CNTs. This allows experimental verification of the Raman features that have so far been theoretically assigned to metallic and semiconducting CNTs.

4.2 Physical Structure of carbon Nanotubes

The best way to visualise a Carbon nanotube is as a section of an infinite Graphene sheet that is then 'rolled up' into a tube. Graphene is a one atom thick layer of Graphite and consists of a hexagonal lattice of Carbon atoms generated by basis vectors $a_1 = a(\sqrt{3}, 0)$ and $a_2 = a(\sqrt{3}/2, 3/2)$ where a is the inter atomic distance between nearest neighbouring atoms. The Carbon atoms in the Graphene lattice are sp^2 hybridised and form strong bonds with the nearest three neighbouring atoms in the same plane and give Graphene an exceptional toughness. In addition, there exists a π orbital aligned perpendicular to the Graphene surface. When multiple Graphene sheets form Graphite, these π orbitals cause weak interactions between the Graphene sheets and allow them to remain together as a material while also allowing individual sheets to slide over one another. The π orbital electrons are also distributed over the Graphite plane, which makes Graphite electrically and thermally conductive along this direction. The curvature effects that stem from rolling the Graphene into a CNT forces the three planar sp^2 hybridised bonds into an out of plane configuration. The curvature also delocalises the π orbitals outside the tube and enhances the electrical and thermal conductivity as well as the toughness of the CNT in relation to Graphene.

Formation of a CNT from two different sections of the Graphene lattice is illustrated in Fig. 4.1. The chiral vector, which describes the circumference of the CNT and is denoted by C in Fig. 4.1, plays an important role in determining the CNT's properties. In all cases, the chiral vector can be expressed in terms of the Graphene basis vectors as

$$C = na_1 + ma_2 \tag{4.1}$$

where n and m are positive integers. The n and m values define the direction of the chiral vector and effectively translate to sections of the Graphene sheet cut at different angles before CNT formation. Since they determine the chiral vector, the values of n and m are

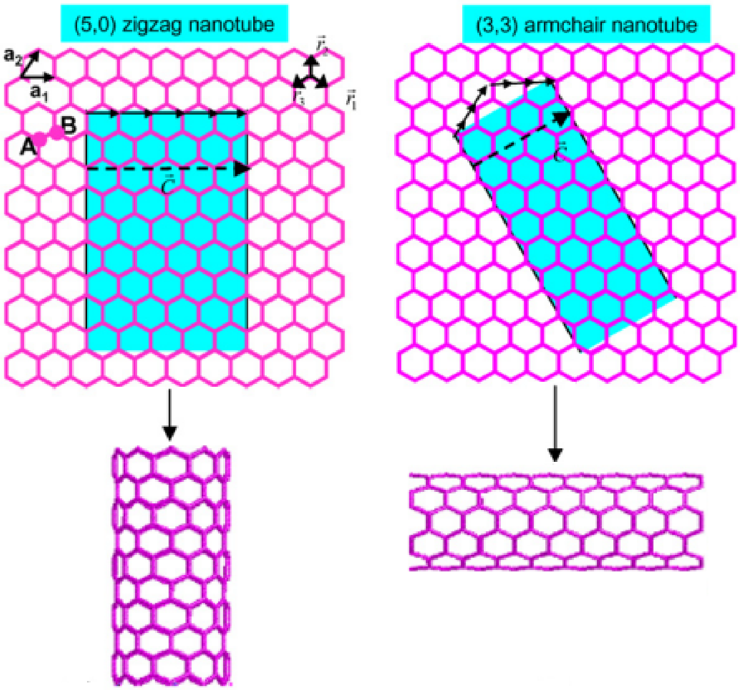

Fig. 4.1: *Different ways a section of Graphene can be rolled to form a CNT. The direction and width of the blue rectangles determines the properties of the resultant CNT. Reproduced from [47].*

extremely important in determining the properties of the CNT.

There are three major groups into which CNTs with different (n, m) values can be classified. Firstly, one of the integers could have a value of zero, resulting in a chiral vector that lies parallel to one of the basis vectors as in Fig. 4.1(a). Such a section, when rolled, forms a zigzag bond pattern at the tube ends and the resultant CNTs are therefore called zigzag CNTs. The second possibility is for both the integers to have the same value as shown Fig. 4.1(b). In this case, an armchair CNT is formed, so called because of the chair like shape at the ends of the CNT. Armchair and zigzag CNTs have some generic properties which do not depend on the exact values n and m. The third case encompasses all the remaining possibilities when n and m are both non zero and n $\neq$ m. These CNTs are called chiral CNTs and their electronic properties depend strongly on their n and m values.

The description of the CNT structure so far has focussed on a single Graphene sheet rolled into a CNT. In reality, they exist as an aggregate of single wall CNTs aligned parallel to each other and held together by Van der Waal's interactions, or as multiwall CNTs wherein a number of CNTs are aligned as concentric cylinders. When grown as single wall

CNTs, they tend to form aggregates immediately after growth or while the CNT material is being collected from the growth system. The aggregates usually have nanotubes embedded in a hexagonal lattice as shown in Fig. 4.2 with each nanotube attached to its neighbours by van der Waal's forces. The spacing between neighbouring tubes is comparable to the inter atomic separation of graphite. Aggregated CNTs can be separated from each other by sonicating in a variety of solvents. It has been observed that pristine CNTs, due to their non polar nature, have higher solubility in non polar solvents compared to polar ones. CNTs do not disperse well in water but the dispersion can be improved by using surfactants like sodium dodecyl sulphate (SDS) or plain detergent to create a molecular layer around individual CNTs that keeps them far apart enough to counter the attractive inter tube Van der Waals forces. Ref. [49] and Ref. [50, 51] respectively describe the efficacy of different solvents and surfactants in forming CNT dispersions.

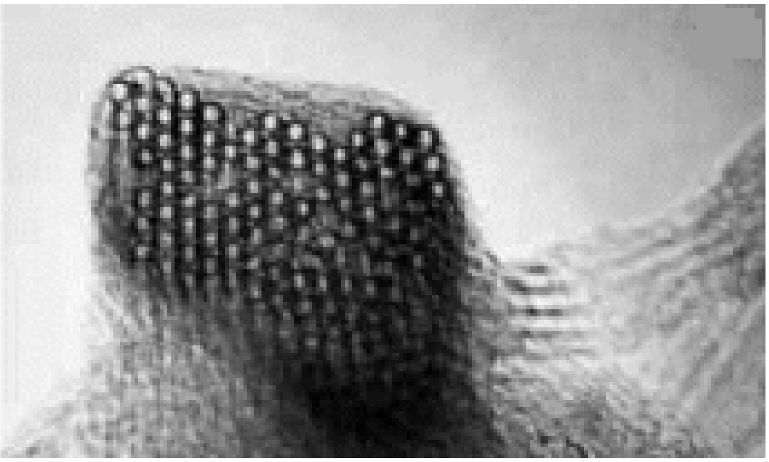

Fig. 4.2: *A bundle of CNTs arranged in a hexagonal lattice. Reproduced from [48].*

Often single wall CNTs are nested within each other as concentric cylinders to form a multi walled CNT. This state is usually achieved during the CNT growth, unlike aggregation which occurs after growth. A high resolution transmission electron microscope (HRTEM) image of such a bundle is shown in Fig. 4.3, where an innermost empty tube and subsequent nanotube layers can be seen. In electronic devices using multiwalled CNTs, the CNT with the lowest resistance (metallic or semiconducting) will define the device behaviour. Multiwalled CNTs cannot be separated as easily as CNT aggregates but it is possible to detect their presence through analytical techniques such as electron microscopy or Raman spectroscopy. A method by Collins *et al.* [53] uses electrical breakdown to burn out successive layers of the multiwalled CNTs. This method exploits previous observations that exposure to air reduces the current density required to burn a CNT [54]. By electrostatically

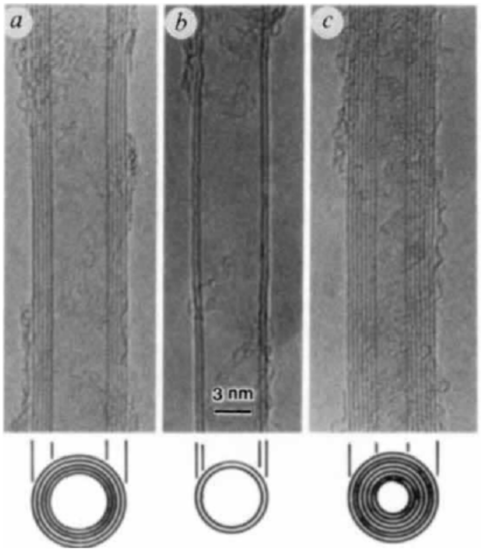

Fig. 4.3: *Cross section of multiwall Carbon Nanotubes showing the individual walls. Reproduced from [52].*

depleting the semiconducting shells and injecting large currents into the multiwalled CNT, it is possible to selectively burn metallic shells and tailor the multiwalled CNTs to some extent.

4.3 Carbon Nanotube growth

A controllable, inexpensive and reliable method for fabricating CNTs is essential for integrating CNTs into mainstream electronics. The requirements from any growth process will depend to some extent on the planned CNT applications. Processes that grow CNTs for use in transistors or other electronic devices require a high degree of control over the character and location of the CNTs. Some other applications, such as fabrication of nano-composites, place higher emphasis on the production volume. A variety of growth techniques have been reported in the literature and a brief description of each is listed below.

Laser vapourisation is a high yield commercial scale production process for CNTs first demonstrated by Smalley *et al.* [55]. In this method, a graphite target with small quantities of metals like Ni or Co is placed in a furnace maintained at 1200°C with an Argon gas flow. The target is then hit by laser pulses, which cause some of the carbon and metal from the graphite target to evaporate and get carried down the furnace by the Argon flow. The CNT continues growing as it flies down the furnace and is finally deposited on a cold target where all the CNT material is collected. This method yields large quantities of single wall CNTs generally packed together as ropes of parallel CNTs. The high yield(70%) of SWNTs makes this the method of choice for companies that commercially produce CNTs [56].

Electric arc discharge was the method that produces the first multiwalled CNTs observed by Iijima [52] in 1991. In this method an electric arc is created between two graphite electrodes of around 6 to 12 mm diameter separated by a gap of around 1 to 4 mm. The graphite electrodes are installed in a water cooled chamber and in a Helium gas environment with sub atmospheric pressure. As the arc operates, the anode is consumed and a cylinder-shaped deposit is grown on the cathode. The rate of the deposit growth is slower than the rate of consumption of the anode and it is therefore necessary to continually move the two electrodes towards each other at a constant feed rate to maintain the arc and the quality of the produced CNTs. In order to ensure a stable operation and a high yield, it is necessary to maintain a constant gap as well as a constant voltage drop across the gap during the entire synthesis process [57].

The arc discharge method generally produces multiwall CNTs, but single wall CNTs can also be produced by adding small amounts of metals like Fe, Co or Ni to the Graphite electrodes. Due to the high operating temperatures, this method is more suitable for production of high quality multi wall nanotubes. The arc discharge method is a robust growth technique that can be scaled for mass production, but the single wall CNTs produced by this method are less pure than those produced by laser ablation. Both laser ablation and arc discharge are used in commercial scale manufacture and for applications where CNTs can be grown ex situ from the point of use.

Chemical vapour deposition (CVD) is a popular CNT growth technique, especially in research because it is comparatively simple, is capable of producing single and multiwall nanotubes and operates at a lower temperature compared to competing processes. In addition, there is a possibility of exerting some control over the location of the CNTs since it is possible to grow the CNTs directly on the substrate that forms the final device [58].

In thermal CVD systems, a substrate with metal catalyst nanoparticles is placed in a tube furnace and the furnace is heated to a growth temperature that is dependent on the metal catalyst used. Once the desired temperature is reached, the Carbon feedstock (Carbon monoxide, Methane, Ethane etc) is introduced for the duration of the growth period. The commonly used catalyst nanoparticles for CNT growth are transition elements such as Iron, Cobalt, Nickel or their alloys. The catalyst nanoparticles can be physically deposited on the substrate before the CVD process is started or by using a “floating catalyst” method, wherein a nozzle is used to inject a vaporised catalyst precursor into the furnace during the

CVD growth stage.

The kind of CNTs grown in this method depends on a variety of factors such as growth temperature, the material and size of the metal catalyst and even the support [58, 59, 60]. Inoue *et al.* [59] observed that the diameter of the CNT grown by CVD on $Fe_{0.8}V_{0.2}$ increased with the nanoparticle diameter and on average, the CNT diameter was larger than that of the nanoparticle. This study also found that the same sized catalyst particle yielded multiwall CNTs at lower temperature (600°C to 700°C) while yielding predominantly single or double wall CNTs at higher temperatures between 800°C to 900°C . These results show that by careful monitoring of catalyst particle size, material and growth temperature, it is possible to control the diameter and character of the CNTs grown by the CVD process.

The presence of metal catalysts on the substrate surface is a disadvantage of the CVD method if the nanoparticle can act as a contaminant for further processing steps. A metal catalyst free CVD process using carbon doped SiGe islands has also been reported [61] and could be more useful in building CNT-based electronic devices without the danger of metal nanoparticle contamination.

4.4 Electronic properties of Carbon nanotubes

4.4.1 Electronic properties of Individual Carbon Nanotubes

The interesting electronic properties of CNTs arise from the band structure of Graphene, which in itself is unique compared to other metals and semiconductors. A derivation of the expression for the Graphene band structure is presented in [47] and the band structure is graphically depicted in Fig. 4.4. This band structure is unique because the valence and the conduction bands of Graphene meet at 6 points at the edge of the Brillouin zone while having a separation (band gap) for other k_x and k_y values. Electrically therefore, Graphene is classified as a semi-metal as it has non zero density of states at the Fermi level but the Fermi surface consists only of points.

When the Graphene sheet is rolled up to form the carbon nanotube, the wave vector is quantised in the circumferential direction. By superimposing the quantised wave vector on the Fermi surface of Graphene, the allowed energy states of one dimensional CNTs are obtained. These are illustrated in Fig. 4.5 where the allowed states are shown as lines on the hexagonal band structure of Graphene. If the allowed energy states of the CNT (straight lines in Fig. 4.5) intersect one of the vertices of the Graphene Fermi surface, then the CNT will also have a non zero density of states at the Fermi level and will exhibit

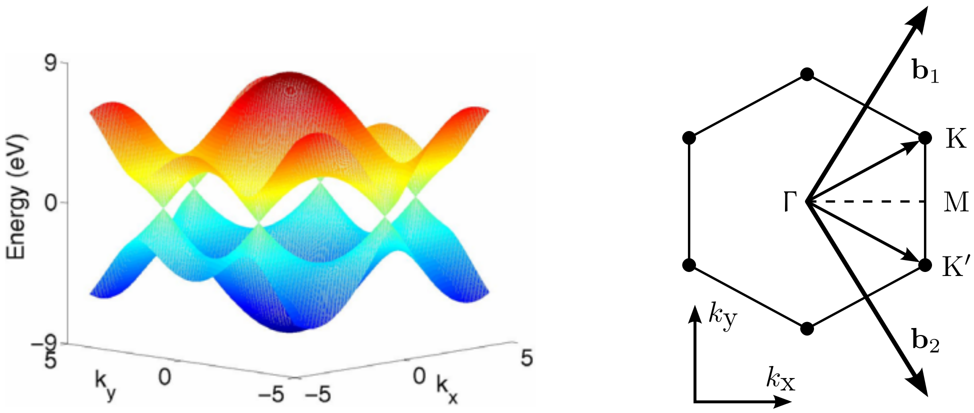

(a) (b)

Fig. 4.4: *(a)Band Structure of Graphene. The valence and conduction bands meet at the six points that form a hexagon at the Fermi level in the k-space. Graphene has non zero density of states at the Fermi level, but the Fermi surface consists just of points. Reproduced from [47]. (b) shows the first Brillouin zone of Graphene. Reproduced with permission from Marek Schmidt.*

metallic character. If there is no intersection between the allowed states of the CNT and the Graphene Fermi surface, then the CNT has no energy states at the Fermi level and exhibits a semiconducting character. The chiral vector controls the electronic properties of the CNT by deciding how the wave vector is quantised. The general rule is that all metallic nanotubes satisfy the condition [47]

$$n - m = 3 \times I \tag{4.2}$$

where I is an integer. According to Eq. 4.2, armchair CNTs ($n = m$) are always metallic while the electronic character of the zigzag and chiral CNTs are determined by the chiral vector. However, only armchair CNTs are truly metallic because they retain their metallic character independent of diameter. All other CNTs that satisfy Eq. 4.2 develop small band gaps at low diameters due to curvature induced effects [47]. The band gaps induced in these CNTs are however, much smaller than those of semiconducting CNTs of an equivalent diameter and therefore these CNTs are called semi-metallic CNTs.

Metallic CNTs have attractive electronic properties and significant effort is being made to incorporate them into electronic devices and circuits. Currently, integrated circuit (IC) interconnects are made of Copper, which starts to break down due to electromigration at current densities of around 10^6 A/cm^2, thereby limiting the scaling of the interconnects.

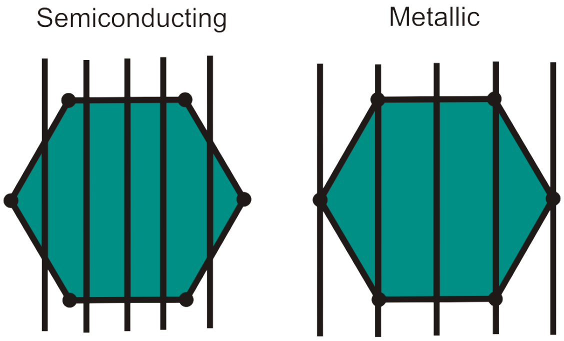

Fig. 4.5: *Allowed energies for CNTs superimposed on Fermi surface of Graphene. The hexagon is the Fermi surface of Graphene shown in Fig. 4.4 and the lines are the quantised wave vectors formed by folding into a CNT. The CNT is metallic if the wave vector passes through the Fermi points of Graphene, otherwise it is semiconducting. Reproduced from [47].*

Metallic nanotubes have been observed to carry current densities of around 10^9 A/cm^2 [62] without use of a heat sink and arrays of CNTs have already been integrated with the CMOS process to form vertical vias that carry an order of magnitude more current than conventional materials [63, 64]. The high current carrying capability and excellent mechanical and thermal properties make metallic CNTs promising materials for use in molecular electronics, either as nanocontacts or as interconnects [47]. Metallic CNTs have also been shown to exhibit ballistic transport with electron mean free paths of a few hundreds of nanometres. The resistance of such CNTs can reach a minimum of 6.5 kΩ and is primarily due to the small overlap between the metal electron energy states and the allowed states in the CNT. Ballistic transport makes CNTs a promising material for spintronic devices as it reduces the possibility of the electron spin flipping due to a scattering event.

Nanotubes that do not satisfy Eq. 4.2 are semiconducting with the band gap determined by the two allowed energy lines closest to one of the Fermi surface points in Fig. 4.5. The band gap is therefore dependent on the chirality and the diameter of the CNT. Theoretical results show that the band gap of semiconducting CNTs [65] should vary as

$$E_g = \frac{\gamma_0 a}{R} \tag{4.3}$$

where γ_0 is the C-C atom tight binding energy (≈ 2.9 eV), a is the nearest neighbour distance for Carbon (≈ 0.142 nm) and R is the radius of the CNT. Experimental data on CNT bandgaps show a good agreement with these theoretical results [66].

4.4.2 Metal-Carbon nanotube contacts

Due to their size and difficulty in positioning on a substrate, forming reliable contacts to CNTs is a difficult task. Side bonded CNT contacts are formed by simply placing the CNT on top of the metal electrodes [67] while an end bonded contact is formed by embedding the ends of a CNT inside the metal electrodes. End bonded contacts exhibit a lower contact resistance [67] compared to side bonded ones and are therefore preferred. However, forming end bonded contacts usually involves manually locating CNTs on the substrate and defining the contacts using electron beam lithography and film evaporation [68], which makes it unsuitable for mass production due to its high cost.

Part of the contacting problem also translates into the problem of positioning and directing CNT growth. Since a proper device is formed only when both ends of the CNT have been contacted, it is necessary that the location of the CNT is accurately defined. Soh *et al.* [69] used PMMA resist and electron beam lithography to pattern Silicon oxide and form windows on the substrate wherein they deposited metal nanoparticles. The process is designed to deposit nanoparticles only in the windows of the Silicon dioxide and when the CNTs were grown from these nanoparticles using CVD, it was found that quite often they bridged the gap between two neighbouring windows. Since the locations of the windows were predetermined, it was possible to deposit metal in them and contact both ends of the CNT. This process has a higher degree of control over the locations of the CNT but the direction of growth is still unpredictable. An improvement in directionality using electric [70] or magnetic fields [71] may improve the process yield.

Some of the metals that have been used to contact CNTs are Au [72], Al [73], Ti [69, 73, 74], Pd [73, 75, 76] and Pt [77]. The characteristics and the quality of the contact was found to vary widely with the metal used for contact formation. Among these, Palladium has been observed to form low resistance and reproducible contacts with both semiconducting [73, 75] and metallic [76] CNTs due to its high work function and favourable wetting properties with the CNT sidewalls [75, 78, 79]. The sidewall interaction is especially important as it distinguishes Pd-CNT contacts from other metals with high workfunctions such as Pt and Au, which formed higher resistance contacts and had lower reproducibility than those formed with Pd. The high cost of Palladium may make it unsuitable for commercial use but it is widely used in research, where production volumes are low.

4.4.3 Importance of contacts in Carbon nanotube devices

The one dimensional structure of CNTs differentiate the metal-CNT contact from that between a metal and planar semiconductor. The primary difference is the diminished role played by Fermi level pinning in determining the metal-CNT contact properties. The metal-planar semiconductor contacts result in the formation of metal induced gap states (MIGS) in the semiconductor band gap. The density of the MIGS decays exponentially from the interface, but these states create a sheet of charge at the metal-semiconductor interface that causes the Fermi level of the metal to be pinned quite strongly within a certain energy range. The metal-semiconductor Schottky barrier height is therefore always observed to be in a narrow energy range, irrespective of the workfunctions and electron affinities of the metal and semiconductor. In a metal-CNT contact on the other hand, the interface charge created by the MIGS is in the form of a small dipole ring, whose effect is negligible beyond a few nanometres from the interface. This barrier is too thin to significantly affect the electrical characteristics and therefore the metal-CNT Schottky barrier height has a closer match with its theoretical value, defined by the metal workfunction and the electron affinity of the CNT [80].

Their small size and sensitivity to surface adsorbates makes it impractical to dope CNTs to form n-type and p-type regions for use in electronic devices. Most CNT based electronic devices therefore rely on the properties and electrostatic modulation of the CNT-metal contacts. Electrostatic coupling via a gate modifies the bulk CNT energy levels as well as the thickness of the Schottky barriers formed at the metal-CNT interface. The device consequently switches on when the barrier is removed or it is made so thin that a tunnelling current is allowed to flow. Metal-CNT junction properties and their modulation are therefore significantly more important than in conventional electronic devices where most phenomena occur across a semiconductor-semiconductor interface with the metals chosen so as to form Ohmic contacts. Innovative designs such as the use of two buried gates to independently modulate the two metal-CNT contacts have been used to form a p-n diode like device without doping the CNT [81]. This highlights the importance of metal-CNT contacts in achieving desired device characteristics.

The ability to control the metal-CNT Schottky barrier properties through the use of an appropriate metal and the importance of contact properties in CNT based electronic devices make it an important area of research. In the subsequent sections a novel technique for modulating the metal-CNT contacts is presented and used to analyse CNT character.

4.5 Analytical techniques

4.5.1 Scanning electron microscopy

Electron microscopy is an important tool in CNT research because the typical CNT has a diameter between 1 and 2 nm, which is too small to be imaged using optical microscopy. Electron microscopes use an electron beam instead of light for imaging samples and the shorter wavelength of the electron beam results in higher resolution and magnification compared to optical microscopes. In addition, impinging an electron beam onto a sample also creates a variety of other signals such as Auger electrons and X-Rays that can be used to deduce further structural and elemental information about the sample [82].

The scanning electron microscope (SEM) functions by directing a beam of electrons, called primary electrons, to a point on the sample to be imaged. When the beam hits the sample surface a variety of phenomena occur, including emission of backscattered electrons, secondary electrons, Auger electrons and X-Rays. The most important for the SEM are the secondary electrons and backscattered electrons. Secondary electrons are the electrons emitted from the surface atoms due to interaction with the high energy primary electrons. Backscattered electrons are those primary electrons that are reflected or re-emitted from the surface after absorption. The secondary and backscattered electrons are collected using separate detectors and transformed into an intensity signal for the point in focus. The electron beam is then scanned across the sample surface and the variations in intensity between different points allow a raster image of the sample surface to be formed.

Typical SEM resolutions are between 2 and 5 nm, which means that theoretically, it should not be possible to image single wall CNTs (diameters between 1 and 2 nm) using SEMs. However, CNTs on an insulating substrate still exhibit high contrast compared to the insulating substrate due to a difference in conductivity [83]. The conductivity difference causes the CNT to remain at a positive potential compared to the surrounding bulk insulator and increases the number of secondary electrons emitted from the CNT, resulting in a contrast difference with the background. The CNT diameters in SEM images ($\approx$ 50nm) are observed to be much larger than the actual physical diameters ($\approx$ 5 nm) measured by techniques such as atomic force microscopy (AFM). This is because the potential difference between CNT and bulk insulator creates an electric field that affects the secondary electrons and causes the CNT diameter to appear larger. The CNTs imaged in this chapter were placed on 20 nm Silicon oxide, which allowed imaging using an SEM.

4.5.2 Raman spectroscopy

Raman spectroscopy is an analytical technique based on Raman scattering, the inelastic scattering of photons by atoms. Inelastic scattering involves a change of photon energy via interaction with the phonon modes in the material lattice. A schematic of the electronic transitions involved is shown in Fig. 4.6. Electrons in the ground state of the material are excited to the excited state by interaction with incident photons. After excitation, the electrons may gain or lose energy via the phonon mode(s) of the material. At some point after its phonon interactions, the electron loses energy via photon emission, recombines with a hole, and returns to the ground state. The difference between the absorbed and emitted photons is the amount of energy gained or lost to the phonon modes. By examining this difference, it is possible to map the dominant phonon modes, which provide detailed structural information because the phonons basically arise from atomic vibrations and their interactions with the material's lattice. A Raman measurement is performed using a laser as the photon source and detecting the intensities of the emitted light over a wide range of frequencies. The differences in energy and the intensities of the light at each frequency are used to determine the dominant phonon modes in the material.

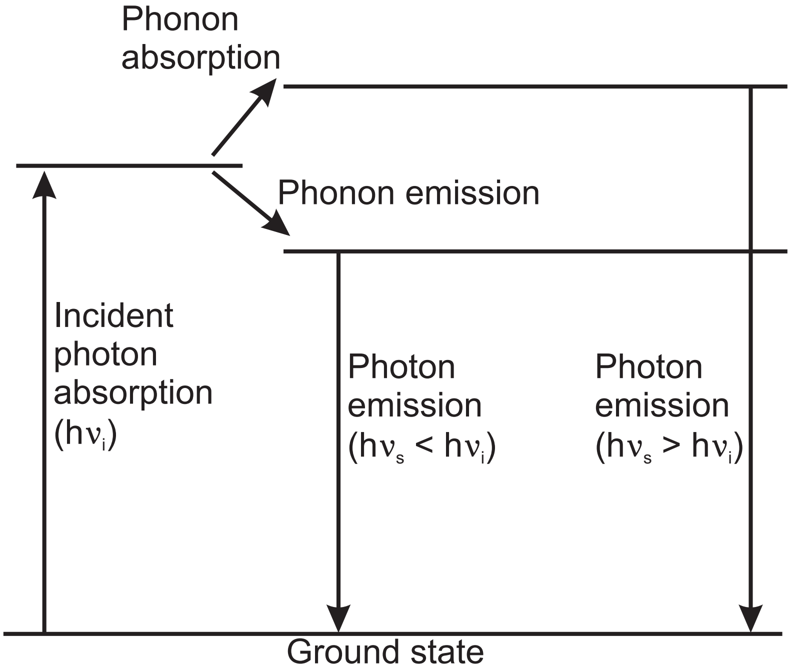

Fig. 4.6: *Illustration of the electronic transitions during inelastic scattering of light. The excited electron may gain or lose additional energy via phonon interactions. The energy of the final emitted photon therefore differs from that of the incident photon by the amount of energy gained/lost to the phonons.*

The Raman signal is usually very weak, but is significantly enhanced when the energy of the incident photons matches the energy difference between optically permitted energy transitions for the electrons in the material. This specific case of Raman scattering is called resonant Raman scattering and its strength depends on the density of states at the two energy levels between which the electron transitions. This is especially beneficial in the case of CNTs, whose 1D structures result in their density of states exhibiting van Hove singularities, which are high density of states in narrow energy ranges. When the incident laser energy matches the difference between any two van Hove singularities, it produces strong Raman signals that make it possible to study even isolated single wall CNTs using Raman spectroscopy.

The primary feature in the Raman spectrum of defect free Graphene is the G-band at around 1580 cm^{-1}, which originates from the doubly degenerate phonon mode that is active for Carbon sp^2 networks [84, 85]. Usually, the Graphene layer contains defects, which give rise to a D-band at around 1350 cm^{-1}, a D´-band at around 1620 cm^{-1} [85] and a G´-band between 2500 to 2800 cm^{-1} which is an overtone of the D-band due to the second order of zone boundary phonons that would normally not be active in the case of defect free Graphene [86, 87]. Each of these defect induced features are due to second order Raman scattering involving phonons and defects with the D and D´bands caused by one elastic and one inelastic scattering event while the G´band is caused by two inelastic scattering events in the material lattice. A wealth of information about the Graphene layers can be obtained from the Raman spectra. The intensity ratio of the D and G bands is used to judge the quality of the Graphene layer. The shape and symmetry of the G´-band is indicative of the number of Graphene layers in the sample [86]. The position and width of the Graphene G-band also varies when the carrier charge density is modulated using a gate electrode [88]. This sensitivity to carrier charge density makes it possible to study electron or hole doping in Graphene by using Raman spectroscopy.

The folding of Graphene to form CNTs changes the Raman spectrum. One difference is the presence of a feature termed the radial breathing mode (RBM) in the CNT Raman spectrum, which corresponds to the coherent movement of all Carbon atoms in the radial direction, as if the CNT were "breathing". This feature occurs only with CNTs and its occurrence is therefore conclusive evidence of the presence of single wall CNTs [89]. The RBM is observed between 100 and 300 cm^{-1} and has a diameter dependence of $\omega_{RBM} = 248/d_t$, where ω_{RBM} is the location of the RBM peak and d_t is the diameter of the CNT. The location of the RBM peak and the incident laser energy can be used to assign a chirality to the CNT under consideration [90]. Like Graphene, CNTs also exhibit a G-band, but one that is split into a theoretical maximum of six peaks due to the symmetry breaking effects of CNT curvature and the folding of the Graphene Brillouin zone [91, 92]. The occurrence of all six peaks in the spectrum is rare and both semiconducting [91] and metallic [93] CNTs more often have G-bands with between 2 and 3 peaks. The G-band lineshape is used to differentiate between metallic and semiconducting CNTs. It is observed that the G-band of semiconducting CNTs is composed of two Lorentzian peaks at around 1570 cm^{-1} and around 1590 cm^{-1} [90, 94] while that of metallic CNTs has one Breit-Wigner-Fano peak at around 1550 cm^{-1} and one Lorentzian peak at around 1590 cm^{-1} [93, 95]. The BWF peak in metallic CNTs is observed due to the downshifting and broadening of a Lorentzian peak caused by the coupling of discrete phonons to the electronic continuum of metallic CNTs [93]. The lower frequency peak of the G-band also has a diameter dependence of $\omega_G^- = 1591 - C/d_t^2$ where ω_G^- is the location of the lower frequency G-band peak and the value of C is 47.7 nm^2cm^{-1} for semiconducting CNTs and 79.5 nm^2cm^{-1} for metallic CNTs [94].

Raman spectroscopy is a very sensitive and versatile technique that can provide extensive information about the CNT structure and character. However, a lot of the interpretation of Raman spectra is based on theoretical results. Experimental confirmation of the Raman features and the CNT characteristics will increase the reliability of the theoretical Raman feature assignments.

4.6 Device structure

The devices used to characterise CNTs in air and Hydrogen were fabricated using the method described in Section 5.3.1 and were contacted by electrodeposited $Pd_{0.59}Ni_{0.41}$ electrodes. A schematic of the device cross section is shown in Fig. 4.7. In addition to the PdNi-CNT contacts, there is also a pair of PdNi-Si contacts which could cause a leakage current to flow through the Silicon substrate. This leakage current is suppressed by using the biasing scheme shown in Fig. 4.7, which reverse biases the two PdNi-Si contacts. The potential V_1 applied to terminal T1 is the variable that is swept from 0 V towards negative potentials during electrical measurements.

Electrostatic coupling with a gate electrode is the usual technique to deduce the CNT character from electrical measurements. Metals like Palladium and Nickel have high work functions that form an ohmic contact with the CNT valence band in the absence of any gate bias. A negative gate potential enhances their overlap with the CNT valence band and causes a larger current to flow through the CNT. A positive gate potential on the

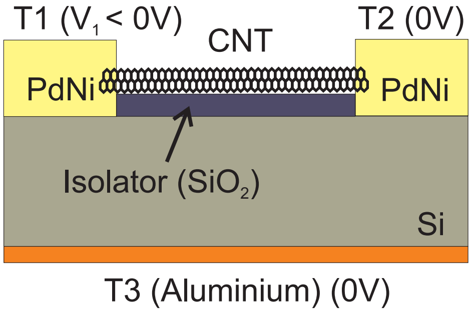

Fig. 4.7: *Schematic of the device used to characterise CNTs in air and Hydrogen. T1, T2 and T3 are the terminals of the device. The biasing scheme shown here is used to measure the CNT current while ensuring the PdNi-Si Schottky diodes remained reverse biased.*

other hand, reduces the overlap between metal Fermi level and CNT valence band and consequently reduces the CNT current. An alternative technique is to modulate the metal-CNT contacts by changing the metal Fermi level energy instead of the CNT band energies. This is equivalent to a change in the contacting metal itself and does not require any gate control.

As described in Chapter 3, exposing PdNi alloys to gaseous Hydrogen reduces the PdNi workfunction. This method can be used to modulate the PdNi-CNT contacts and thereby characterise the contacted CNT. It is important to note that Hydrogen exposure will also reduce the PdNi-Si Schottky barrier heights and cause them to conduct larger currents. Since the measured quantity is the total current sourced from terminal T1 in Fig. 4.7, it is necessary to compensate for the increased PdNi-Si Schottky barrier current in order to accurately measure the CNT current in a Hydrogen environment. To develop a compensation procedure, the I-V characteristics of a device without the connecting CNT was measured in air and Hydrogen. The biasing scheme described in Fig. 4.7 was used for this measurement, with V_1 swept from 0 to -1V. The measured currents are plotted in Fig. 4.8.

Fig. 4.8(a) shows the I-V characteristics in air and proves that all three currents are small (<1 nA) as expected from reverse biased PdNi-Si Schottky barriers. The current through the Schottky barrier T1 in Fig. 4.7 increases with increasing potential and most of this current flows between T1 and T3. The current through the zero biased Schottky diode (T2) remains low over the entire measurement range, showing that very low currents are sourced/sunk through this terminal. Fig. 4.8(b) shows the electrical characteristics of the same device measured after an exposure to 5 mbar of Hydrogen for about 75 minutes. The current magnitudes have all increased as expected, due to a reduction in the PdNi

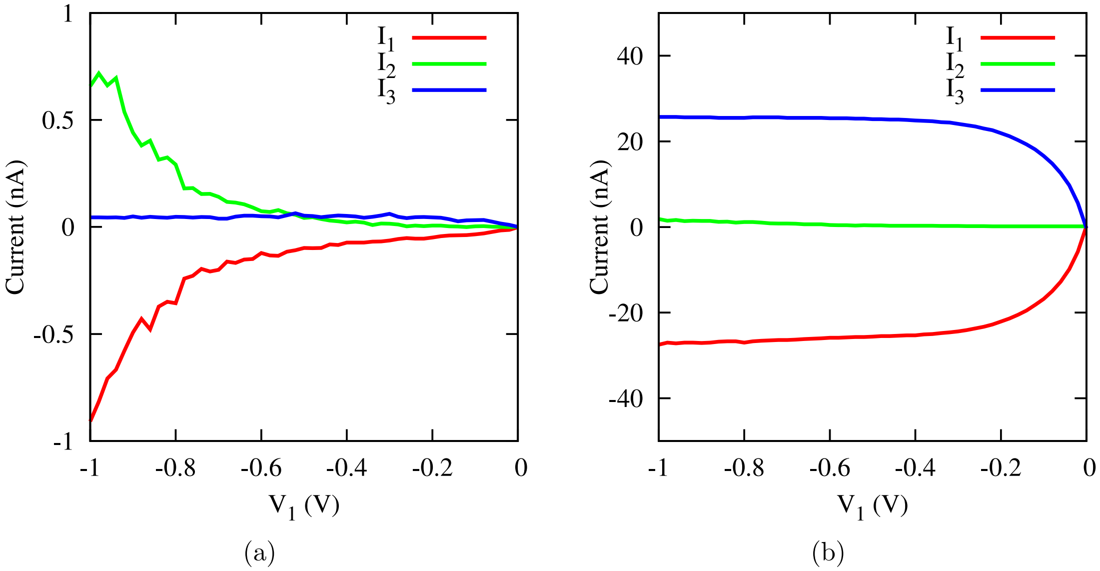

(a) (b)

Fig. 4.8: *Currents measured in (a) air and (b) Hydrogen from terminal T1 (I_1), T2 (I_2) and T3 (I_3) of the device in Fig. 4.7 in absence of a CNT. T2 and T3 are set to 0V and* I_2 *is observed to be low, showing that low currents are sourced/sunk through this terminal. The current between T1 and T3 increases on Hydrogen exposure and has to be compensated for during CNT measurements.*

workfunction and consequent decrease in PdNi-Si Schottky barrier height. Once again, most of the increased current flows between T1 and T3, while the current through the zero biased Schottky diode (T2) remains significantly lower.

Fig. 4.9 shows a simple equivalent circuit of the device depicting the PdNi-Si Schottky barriers, PdNi-CNT contacts and the measured currents from each terminal. The absence of a CNT means that $I_{CNT} = 0$ A in the measurements shown in Fig. 4.8. These measurements also show that the values of I_{23} and I_{12} always remain low and I_{13} incorporates the bulk of the current change due to PdNi-Si Schottky barrier modification. In the presence of a CNT, both currents I_{CNT} and I_{13} are sourced from T1 and therefore the difference (I_1 - I_3) will give the value of the CNT current after compensating for the increased PdNi-Si Schottky barrier current due to Hydrogen modification. This difference is plotted as the CNT current in all subsequent I-V plots. Since the highest measured current is about 25nA in Fig. 4.8(b), a measured CNT current at least an order of magnitude higher was taken to be conclusive of the presence of an interconnecting CNT.

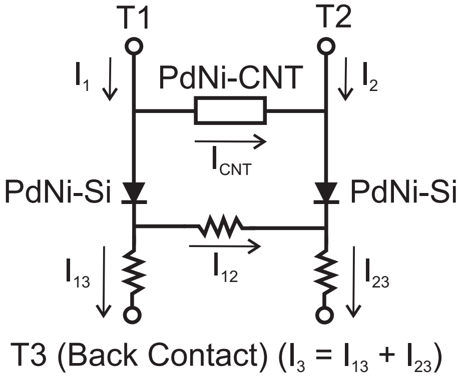

Fig. 4.9: *Simple model of the device in Fig. 4.7 showing PdNi-Si Schottky barriers and the PdNi-CNT contact.* I_1*,* I_2 *and* I_3 *are the experimentally measured currents, while other currents are those flowing through each available path in the device.*

4.7 Electrical characterisation and Raman spectroscopy

Devices where the two ends of the CNTs were connected by the $Pd_{0.59}Ni_{0.41}$ contacts were found by scanning the chip area with an SEM. Those that had a single interconnecting CNT and that showed reproducible electrical characteristics in air were chosen for characterisation in a Hydrogen environment. The CNTs were measured in the vacuum chamber of an EMTTP4 probe station with an Agilent 4155C parameter analyser. The Hydrogen measurements were performed by evacuating the vacuum chamber and then pumping it with pure Nitrogen to a partial pressure of 0.3 bar and a 5% Hydrogen-Nitrogen mixture till a partial pressure of 0.1 bar. This corresponds to a Hydrogen partial pressure of 5 mbar.

An SEM image of one interconnecting CNT is shown in Fig. 4.10 and the electrical characteristics of the same CNT as measured in air and Hydrogen are shown in Fig. 4.11. In air, the electrical characteristics show that the PdNi-CNT contacts are not rectifying and are closer to being ohmic contacts. On exposure to Hydrogen, the current through the device decreases and starts resembling a diode characteristic. This change in the I-V characteristics can be explained by examining the effect of Hydrogen gas on the energy bands at the PdNi-CNT interface.

Fig. 4.12(a) shows the band diagram of the PdNi-semiconducting CNT contact in air, with typical values for the PdNi workfunction and CNT electron affinity. The Fermi level of the CNT is shown closer to the valence band as CNTs are inherently p-type when exposed to the atmosphere [98]. The high workfunctions of Palladium and Nickel cause their Fermi level to overlap with the CNT valence band and form an ohmic contact. The extent of

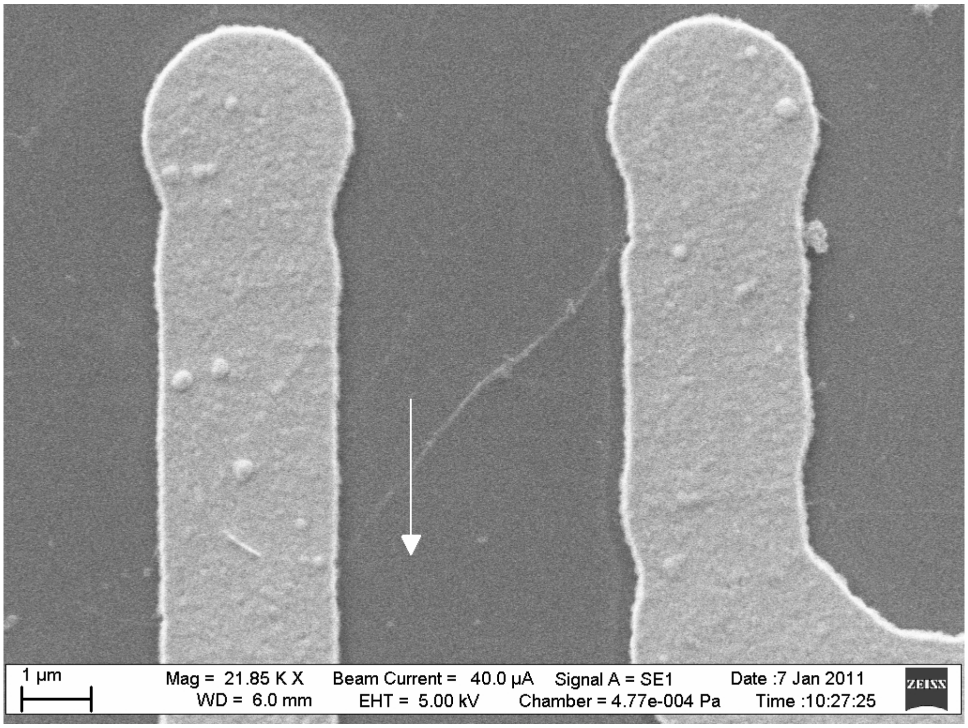

Fig. 4.10: *SEM image of a CNT connecting two* $Pd_{0.59}Ni_{0.41}$ *electrodes. The arrow in the figure shows the direction and the length over which Raman spectra were collected.*

the overlap between the PdNi Fermi level and CNT valence band is shown by the quantity qΦ in Fig. 4.12. This value will be close to the numerical difference between the metal workfunction and the CNT valence band energy due to reduced Fermi level pinning in any metal-CNT contact [47, 80]. On exposure to Hydrogen, the PdNi workfunction is reduced and the band structure is transformed into that shown in Fig. 4.12(b). The workfunction decrease moves the PdNi Fermi level to a higher energy and realigns the energy bands such that the PdNi Fermi level has a smaller overlap with the CNT valence band or has possibly even moved into the CNT bandgap. A reduction in the overlap reduces the current through the device as the CNT density of states aligned with the metal Fermi level is lower. If the metal Fermi level has moved into the CNT bandgap, the PdNi-CNT contact is transformed from an ohmic contact to a Schottky barrier. The CNT will therefore show rectifying or back to back Schottky diode characteristics, depending on whether only one or both PdNi-CNT contacts have transformed into Schottky diodes. Metallic CNTs should not show a significant current change on Hydrogen exposure as the absence of a bandgap means the metal Fermi level will always be aligned with some CNT energy levels having non zero density of states. Examining the change in I-V characteristics of CNTs exposed to

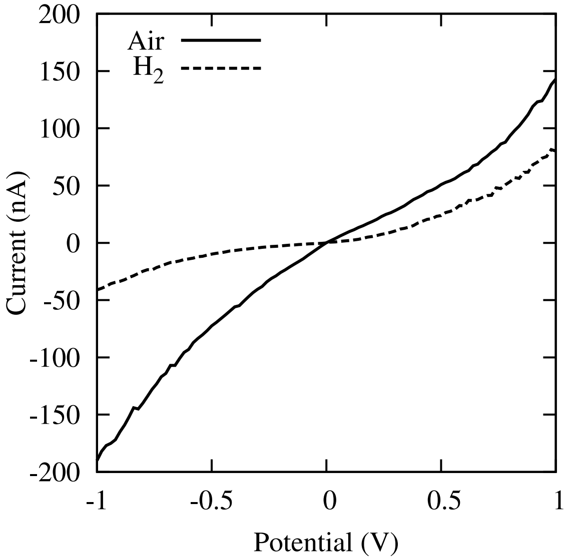

Fig. 4.11: *I-V characteristics of the CNT from Fig. 4.10 in air and Hydrogen. The current measured in a Hydrogen environment shows a large percentage decrease as expected from semiconducting CNTs.*

Hydrogen will therefore allow differentiation between semiconducting and metallic CNTs. The reduction in the CNT current as shown in Fig. 4.11 proves that the CNT shown in Fig. 4.10 is semiconducting in nature.

Electrical measurements of the PdNi-Si Schottky barriers in the device in Fig. 4.7 can be used to estimate the PdNi workfunction change by comparing the PdNi-Si barrier heights before and after Hydrogen exposure. The PdNi-Si Schottky barriers were measured on the same device and in the same trial as the CNT electrical characterisation, ensuring that the conditions for both measurements were the same. These Schottky barriers were measured individually, so as to remove any interference from the back to back Schottky diodes or the interconnecting CNT. The measured parameters of the PdNi-Si Schottky barriers are summarised in Table. 4.1 and the workfunction change is estimated to be about 150 mV. However, this value is not fully reliable because it assumes that the change in barrier height will not be affected by Fermi level pinning, which is unlikely in a metal-planar semiconductor contact.

To independently verify the CNT character, a 633 nm laser was swept in steps of 0.3 μm across the CNT as shown by the arrow in Fig. 4.10 and Raman spectra were collected. The Raman data from the radial breathing mode (RBM) and G-band ranges for this CNT are shown in Fig. 4.13(a) and Fig. 4.13(b) respectively, with the lines staggered along the intensity axis for clarity. The rise and fall of the Raman feature intensities as the laser is

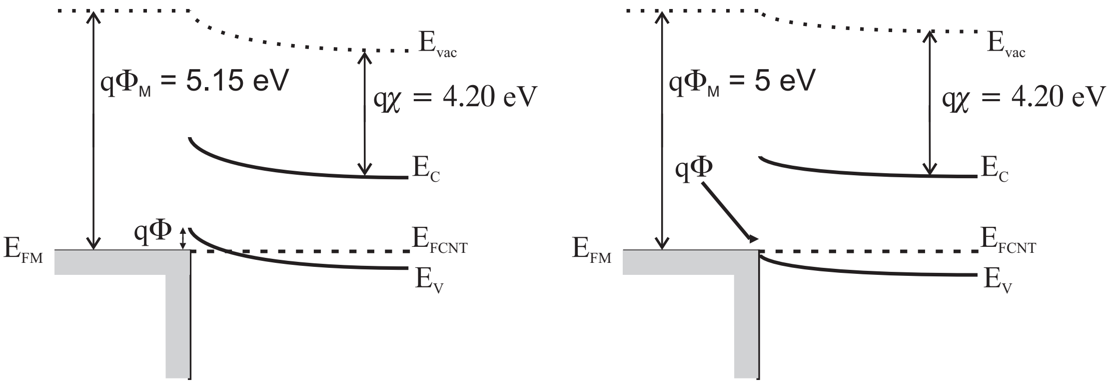

(a) (b)

Fig. 4.12: *Band structures at the PdNi-semiconducting CNT interface. (a) The natural state of the bands in air with a barrier for PdNi to CNT electron transport. The PdNi Fermi level overlaps with the CNT valence band forming an ohmic contact for holes. (b)Band structure after reduction of PdNi work function by 150 mV due to Hydrogen exposure. The overlap between PdNi Fermi level and CNT valence band is reduced, lowering the CNT current. The CNT electron affinity was calculated from typical values of workfunctions and bandgaps listed in Refs. [66, 96, 97].*

Table 4.1: *Parameters of the PdNi-Si Schottky barriers before and after Hydrogen exposure showing a reduction in PdNi workfunction by 150 mV.*

Terminal	Air		Hydrogen	
	$\Phi_B(V)$	η	$\Phi_B(V)$	η
Vd	0.79	1.61	0.64	2.21
Vs	0.79	1.51	0.64	2.28

scanned across the CNT shows that only one CNT is in resonance with the excitation laser.

The strong RBM and the double peak G-band also indicate the presence of a single wall CNT in resonance with the excitation laser [94, 95]. The locations of the RBM and the G-band peaks were found by fitting Lorentzian curves to the strongest Raman spectrum among those shown in Fig. 4.14. Most features in the Raman spectrum of a CNT can be fit with either Lorentzian curves or a Breit-Wigner-Fano (BWF) lineshape, which is essentially a Lorentzian with an asymmetry. In this case, the BWF fits had negligibly small asymmetry factors, showing that the features were essentially Lorentzian. Gaussian fits to the RBM and G-bands were also attempted but the quality of the fit was either lower or at most equal to that of the Lorentzian.

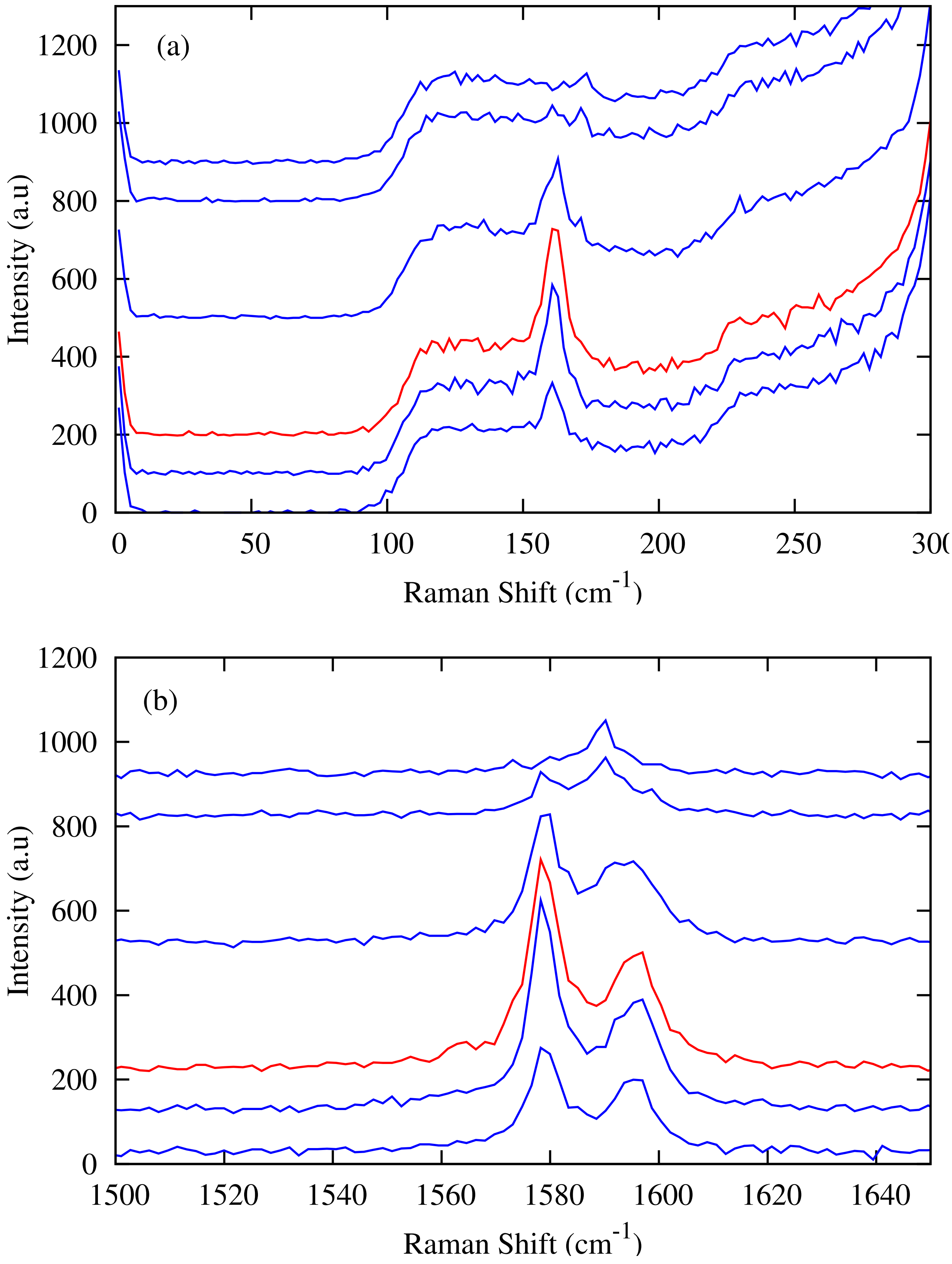

Fig. 4.13: *RBM and G-band peaks obtained by sweeping a 633 nm laser across the arrow shown in Fig. 4.10. The spectra are staggered along the intensity axis for clarity. The peak structures as well as rise and fall of intensities show resonance with a single CNT. The most intense spectrum is plotted in red.*

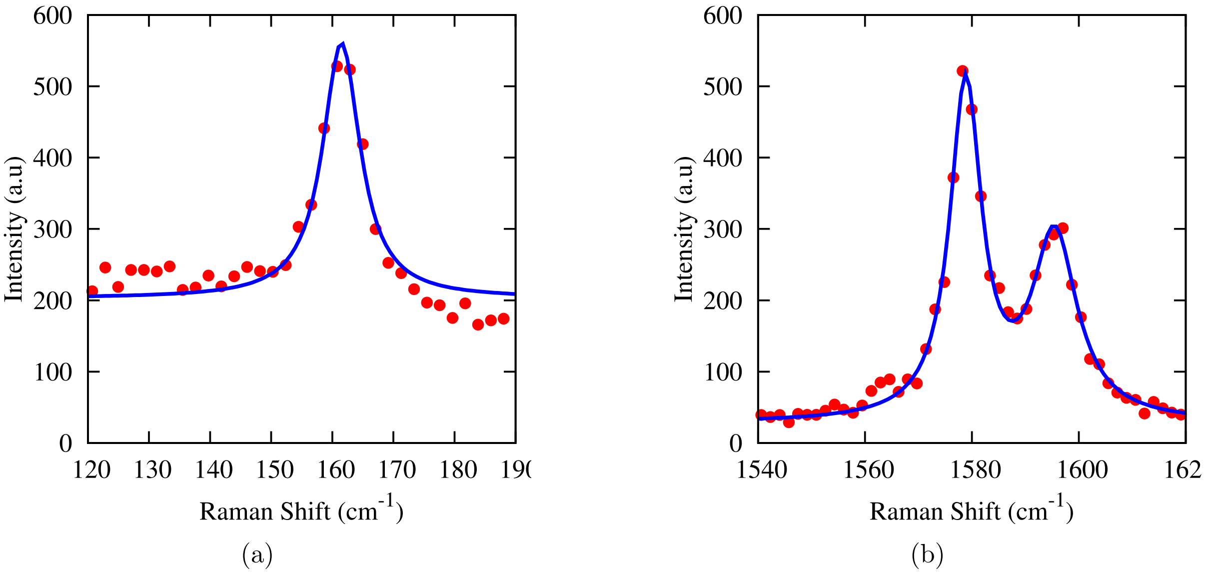

(a) (b)

Fig. 4.14: *(a) The most intense RBM peak from Fig. 4.13(a) fit with a Lorentzian curve. (b) The most intense G-band from Fig. 4.13(b) fit with two Lorentzian curves. The points are the measured Raman data and the line denotes the fit to the data. The RBM and G-band lineshapes match those of semiconducting CNTs.*

The RBM peak for this CNT was located at 161 cm^{-1}, while the two G-band peaks were located at 1579 cm^{-1} and 1595 cm^{-1} respectively. The double Lorentzian peaks in the G-band are consistent with observations in other Raman studies [90, 94, 95] of semiconducting single wall CNTs where Lorentzian peaks were recorded at around 1570 cm^{-1} and around 1590 cm^{-1}. The close match between semiconducting CNT G-band shapes described in the literature and those measured in Fig. 4.13(b) confirm that the CNT from Fig. 4.10 is semiconducting. The diameter of the CNT can be estimated from both the RBM and the G-band peaks [94] and was found to be 1.55 nm and 1.73 nm respectively.

Fig. 4.15 and Fig. 4.16 show an SEM image and measured I-V characteristics in air and Hydrogen for a second CNT. From the SEM image, it can be seen that a single CNT spans the gap between the two electrodes. Fig. 4.16 shows that there is a small increase in the current through the CNT on exposure to Hydrogen gas. The changes in the PdNi workfunctions were calculated by measuring the PdNi-Si Schottky barriers in situ and extracting the barrier heights. The change in the PdNi-Si Schottky barrier heights was calculated to be about 150 mV. A similar workfunction change in the sample measured in Fig. 4.11 caused a large percentage decrease in the current while in this case a small percentage increase is observed. The smaller current change could either mean that the

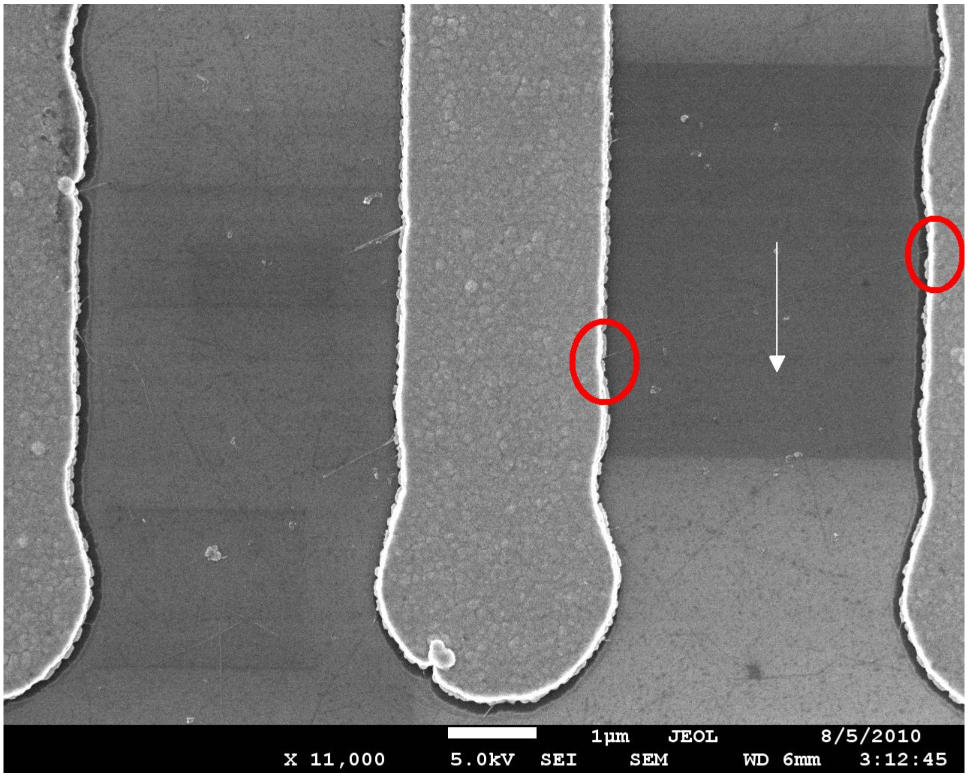

Fig. 4.15: *SEM image of a second CNT contacted by two* $Pd_{0.59}Ni_{0.41}$ *electrodes. The arrow in the figure shows the direction and the length over which Raman spectra were collected. The red circles show the two ends of the CNT.*

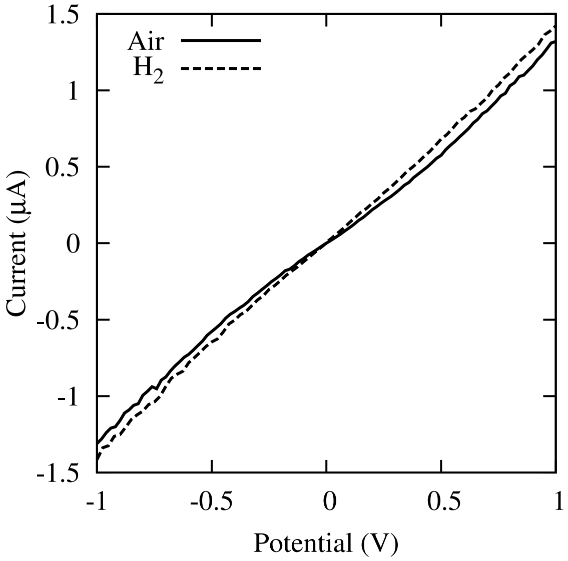

Fig. 4.16: *I-V characteristics of CNT transistor from Fig. 4.15 in absence and presence of Hydrogen. The current measured in a Hydrogen environment does not show a significant change, as expected from a metallic CNT.*

CNT is metallic and has no bandgap or the CNT is semiconducting but has so small a bandgap that despite the 150 mV increase in the PdNi Fermi level energy, it is still not close to the CNT valence band edge.

Fig. 4.17(a) and Fig. 4.17(b) show the RBM and G-band ranges from the Raman spectra of the CNT, staggered along the intensity axis for clarity. The Raman spectra were collected by scanning across the CNT with a 532 nm laser in the direction of the arrow in Fig. 4.15 with a step of 0.3 μm. The presence of a single CNT is indicated by a strong RBM peak, the splitting of the G-band and the rise and fall of the feature intensities as the laser is swept across the CNT. A Lorentzian fit of the strongest RBM feature is shown in Fig. 4.18(a) and yields a peak position of 183 cm^{-1} corresponding to a tube diameter of 1.36 nm. By using this value in Eq 4.3, the bandgap of the CNT is calculated to be about 0.6 eV, which is a typical value reported in the literature [99]. The small current change in Fig. 4.16 is therefore due to the metallic nature of the CNT and not due to an exceptionally small bandgap of a semiconducting CNT.

The G-band data of the strongest Raman spectrum can be fitted with one asymmetric Breit-Wigner-Fano (BWF) lineshape at 1552 cm^{-1} and two Lorentzians with peak positions at 1581 cm^{-1} and 1591 cm^{-1} respectively as shown in Fig. 4.18(b). The BWF lineshape has an asymmetry factor of 0.16 which is similar to values reported in other studies of Raman spectroscopy of individual metallic CNTs [95]. The peak at 1581 cm^{-1} can also be fitted with a BWF lineshape but the value of the asymmetry factor is -0.069, an order of magnitude smaller than that of the 1552 cm^{-1} peak and other reported values in the literature. For this reason, a Lorentzian fit was retained for the 1581 cm^{-1} peak. The fits to this G-band spectrum closely match those reported in the literature [93, 94, 95] for metallic CNTs and therefore show that the CNT is metallic. The electrical characteristics from Fig. 4.16 and the G-band fits from Fig. 4.18 demonstrate that the G-band lineshape of metallic CNTs contain one BWF peak at around 1550 cm^{-1} and one Lorentzian peak at 1590 cm^{-1}.

Fig. 4.19 shows the intensities of the RBM and G-band from the semiconducting CNT as well as the RBM of the metallic CNT as a function of scanning distance, staggered along the intensity axis for clarity. The lines are gaussian fits to the data points and have full width at half maximum (FWHM) between 0.78 to 1.22 μm, consistent with the spot size of between 1 to 3 μm for the Raman system. The gaussian variation mirrors the gaussian intensity distribution of the laser spot and shows that a single CNT is in resonance with the laser spot over the measurement distance.

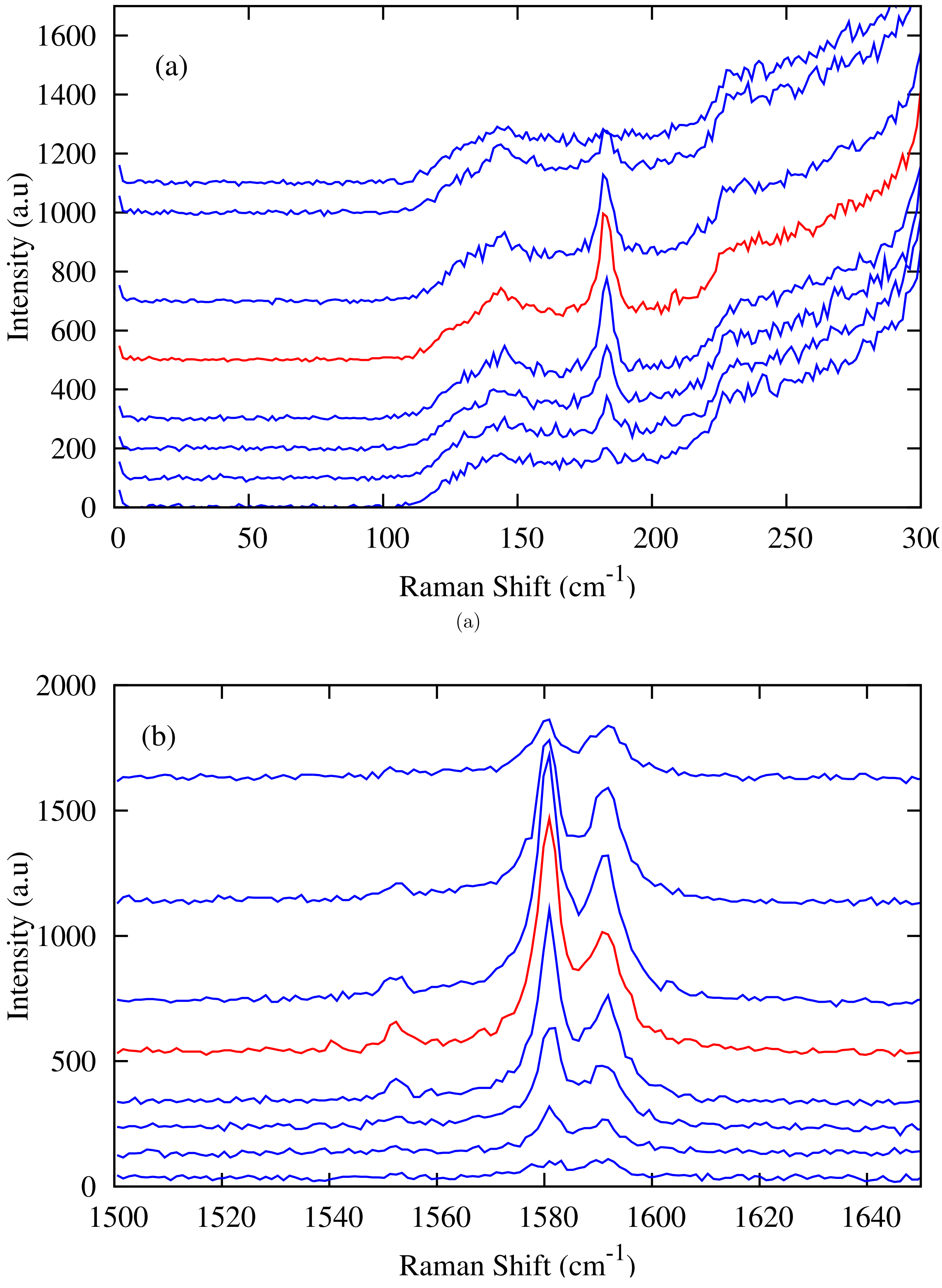

Fig. 4.17: *RBM and G-band peaks obtained by sweeping a 532 nm laser across the arrow shown in Fig. 4.15. The spectra are staggered along intensity axis for clarity. The peak*

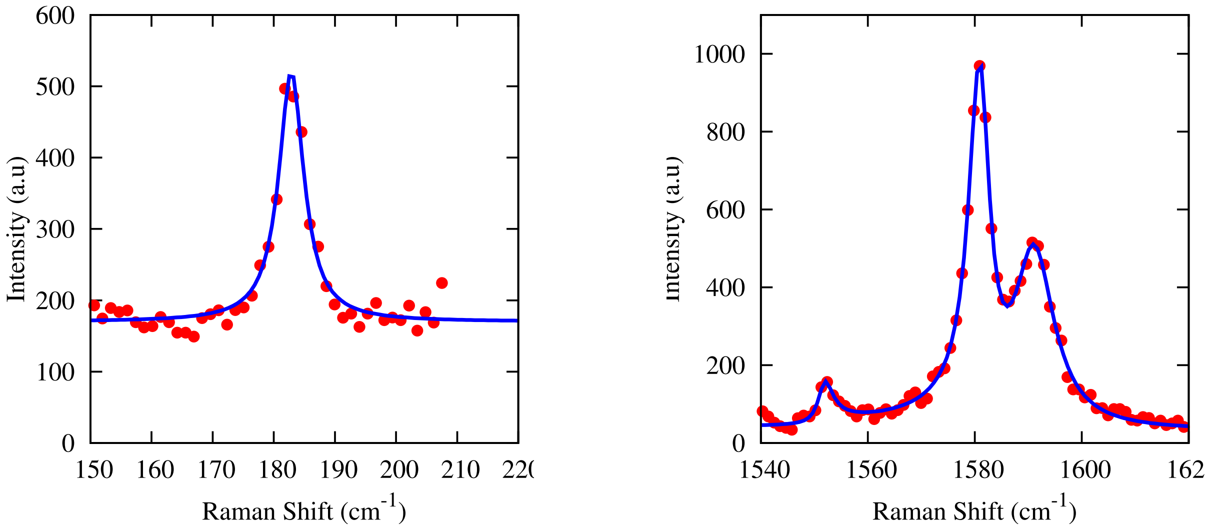

Fig. 4.18: *(a) The most intense RBM from Fig. 4.17(a) fit with a Lorentzian curve. (b) The most intense G-band from Fig. 4.17(b) fit with one BWF and two Lorentizian curves. The points are the measured Raman data and the line denotes the data fit.*

4.8 Conclusion

CNTs contacted by electrodeposited PdNi were characterised using electrical measurements in air and Hydrogen. Exposing PdNi to gaseous Hydrogen causes a reduction in the PdNi workfunction and modulates the barriers at the PdNi-CNT contacts. The change in the CNT current allows differentiation between semiconducting and metallic CNTs. The semiconducting CNTs exhibit a large percentage decrease in current caused by the reduction in the overlap between PdNi Fermi level and CNT valence band after Hydrogen exposure. Metallic CNTs exhibit a small percentage increase as the lack of a bandgap means there is always an overlap between the PdNi Fermi level and CNT energy states. The results of the electrical measurement are correlated with Raman spectroscopic analysis performed on the same CNTs. Previous studies on CNTs used electrostatic gate control [72, 75] or purely Raman spectroscopic [94, 95] analysis but no studies correlating the Raman spectra to the electrical characterisation of CNTs by modifying the metal-CNT workfunction difference have been reported in the literature. The correlation between these two techniques serve as experimental verification of the Raman features that have theoretically been attributed to semiconducting and metallic CNTs. Modulation of the metal workfunction by this technique is equivalent to a change of the metal contacting the CNT as carriers from both the metal and the CNT see different barrier heights at the contact, as compared to electrostatic

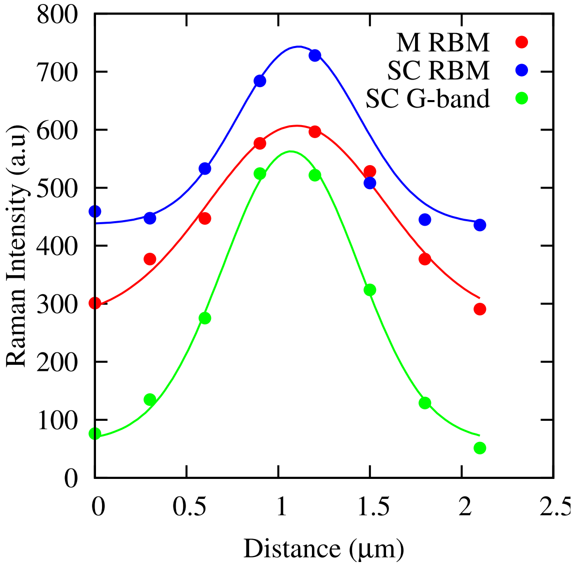

Fig. 4.19: *Intensities of the RBM and G-band of semiconducting (SC) CNTs and the RBM of metallic (M) CNTs plotted against scan distance, staggered along intensity axis. The lines are gaussian fits to the data points. The gaussian distribution shows that a single tube is in resonance with the laser spot and reflects the gaussian intensity distribution of the laser spot.*

control that modifies the contact barriers only for the CNT charge carriers. Developing methods that use this technique can lead to many interesting research possibilities into the CNT band structure and metal-CNT contacts.

5. CARBON NANOTUBE TRANSISTORS

This chapter describes the fabrication and electrical characterisation of Carbon nanotube (CNT) transistors with electrodeposited PdNi contacts. A review of the literature relevant to CNT transistors is presented. Dispersion of CNTs in 1,2- dichlorobenzene and its use in the fabrication of three terminal CNT transistors with electrodeposited PdNi contacts are described. The low PdNi-Si reverse biased Schottky barrier current is used to suppress the current through the Silicon substrate during electrical characterisation of the transistors. The operating restrictions imposed by the presence of a direct PdNi-Si contact are discussed and methods to overcome these restrictions are suggested. The characteristics of the CNT transistor in a changing magnetic field at room temperature are also presented.

This chapter has been partly published in Physica Status Solidi (b), **247**, 888, 2010.

5.1 Introduction

The previous chapter briefly introduced the electronic properties of Carbon nanotubes (CNTs) as well as the formation and modulation of PdNi-CNT contacts. Their attractive electronic properties such as availability of semiconducting as well as metallic material, high mobility, high current carrying capability and the possibility of ballistic transport have sparked huge interest in employing CNTs in electronic devices. The holy grail of this effort is to build integrated circuits completely from CNTs, which would prolong the scaling trend beyond when Silicon technology hits fundamental limits.

This chapter describes the CNT field effect transistors (CNTFETs) that have been reported in the literature. Schemes for doping CNTs or otherwise modifying the properties of the CNT to form n-type and p-type material are also described. The fabrication process for CNT transistors incorporating electrodeposited PdNi and their electrical characterisation are described. These data are used to examine the suitability of electrodeposition as a metallisation process and of PdNi alloys as a contacting material.

5.2 Carbon nanotube based electronic devices

5.2.1 Field effect transistors

CNT field effect transistors (CNTFETs) are structurally similar to conventional MOSFETs but with the CNT serving as the transistor channel. The first CNTFETs were demonstrated in 1998 [72, 77] and were fabricated by depositing a CNT on a Si wafer with prefabricated noble metal contacts. A schematic of the device is shown in Fig. 5.1 and the dependence of the drain-source current as a function of gate potential is shown in Fig. 5.2. The CNT bridges two electrodes to form the channel, with the underlying SiO_2 and Silicon acting as the gate oxide and back gate electrode respectively. In such "side bonded" devices, the

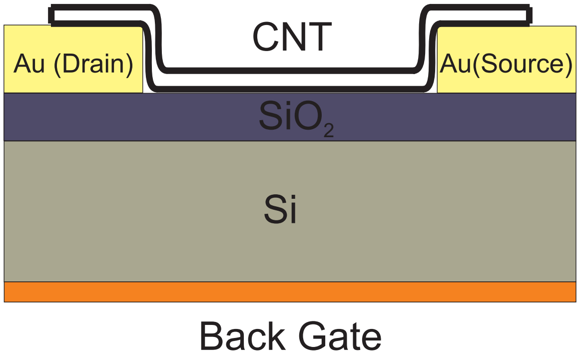

Fig. 5.1: *Schematic of a back gated CNTFET fabricated by placing a CNT on Au electrodes. Modified from [72].*

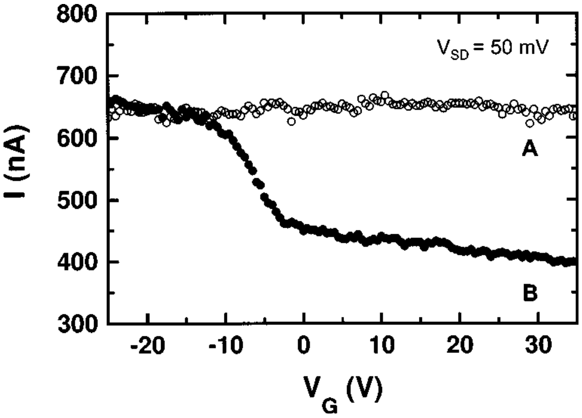

Fig. 5.2: *Electrical characterisation of semiconducting and metallic CNTs in the structure shown in Fig. 5.1. The graph shows the drain current dependence on gate voltage. Solid circles are from semiconducting CNTs and empty circles are for metallic CNTs. Reproduced from [72].*

CNT is merely placed on top of the metal contacts and not embedded in them [67, 72, 77]. Nevertheless, these devices were functional and exhibited p-type FET characteristics with high parasitic contact resistance(≥ 1 MΩ), low drive current and low transconductance (10^{-9} A/V) [67].

An alternative method is to form "end bonded" contacts, in which the ends of the CNTs are embedded in the metal electrodes forming a superior contact [74, 100]. Some studies also employed an annealing step that further improves the end bonded metal-CNT contact. End bonded devices exhibit a lower contact resistance (~ 30 kΩ) and a higher transconductance (3.4×10^{-7} A/V) compared to their side bonded counterparts. Output characteristics from such an end bonded device with a back gate are shown in Fig. 5.3, with the inset showing the device structure.

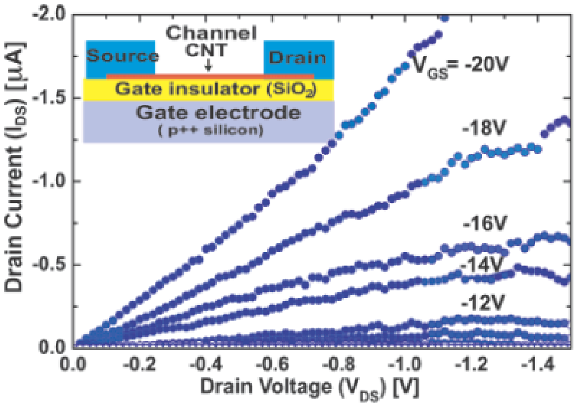

Fig. 5.3: $\mathrm{I_D - V_D}$ *characteristics of Back-gated CNTFET formed by contacting a CNT with Cobalt electrodes. The inset shows the structure of the device. Reproduced from [67].*

However, a significant disadvantage arises from the back-gated CNTFET structure shown in Fig. 5.1 and Fig. 5.3. Using a back gate to control the CNTFET characteristics means that all devices on the Silicon wafer are switched simultaneously and individual control of the CNTFETs is not possible. In addition, the electrostatic coupling between the back contact and the CNT is weak due to the presence of the substrate as well as gate oxide and therefore the devices required high gate voltages to switch. This is illustrated by the output characteristics in Fig. 5.2 and Fig. 5.3, where gate voltages of between -10V and -20V are required to switch the devices on.

The I-V characteristics in Fig. 5.2 and Fig. 5.3 also show the p-type behaviour of the transistor. Since the device behaviour is dependent on the channel characteristics, this implies that the connecting CNT is p-type, even when specific steps to induce p-type behaviour were not followed during fabrication. This intrinsic p-type behaviour is also observed in other CNTFET studies [77, 101] and one explanation for this behaviour is the adsorption of oxygen on the CNT surface [98]. The p-type behaviour can be reversed by simply annealing the CNT in vacuum [67], but it recurs on exposure to air. This is a second disadvantage of the back gated structure, as the CNTs on the surface are not protected from air and will therefore tend to take on p-type characteristics over time [98]. Any application that needs n-type CNT behaviour with a back gated structure has to shield the CNT from the atmosphere with a protective layer, which introduces additional processing steps during fabrication.

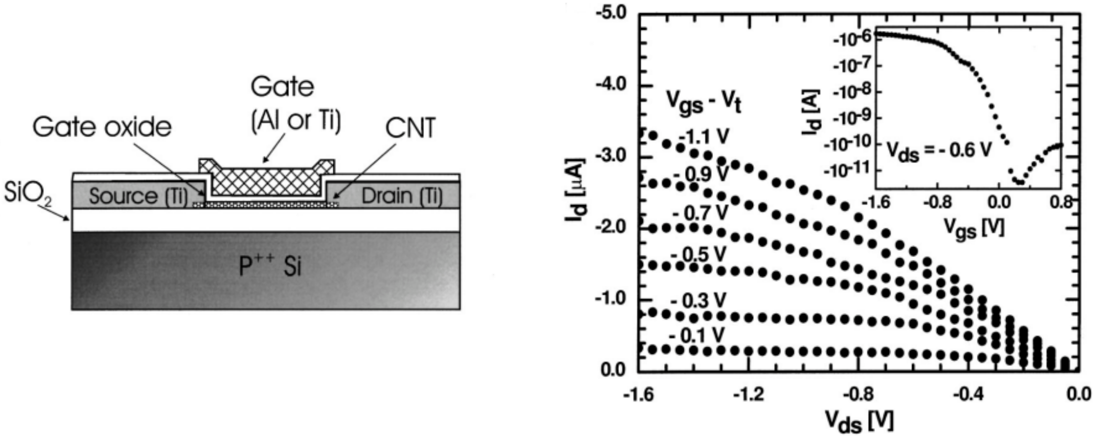

(a) (b)

Fig. 5.4: *(a) Top-gated CNTFET with Titanium electrodes, SiO_2 gate oxide and metallic gate. (b)* $I_D - V_D$ *characteristics of device from (a). Reproduced from [100].*

The top-gated CNTFET structure described in Ref. [100] and shown in Fig. 5.4 is a solution to both these problems. This CNTFET was fabricated using Ti to contact CNTs dispersed on the Si substrate. A very thin layer of SiO_2 was then deposited on top of the CNT to form the top gate. The top gate and thin oxide layer allowed individual CNTs to be controlled and switched at significantly lower voltages and also protected the n-type CNTs from atmospheric oxygen. Fig. 5.4(b) shows that the top gated device has a significantly lower threshold voltage than the back gated devices from Fig. 5.2 and Fig. 5.3 and puts the threshold voltage at a value similar to that of conventional MOSFETs.

An alternative CNTFET structure that achieves individual control without a top gate is described by Bachtold *et al.* [102] and is depicted in Fig. 5.5(a). The primary difference is the fabrication of an Aluminium gate on top of the SiO_2 layer before the CNTs are deposited and contacted using Gold electrodes. The thin layer of naturally forming Aluminium oxide then functions as the gate oxide. This device structure allows individual FET control but

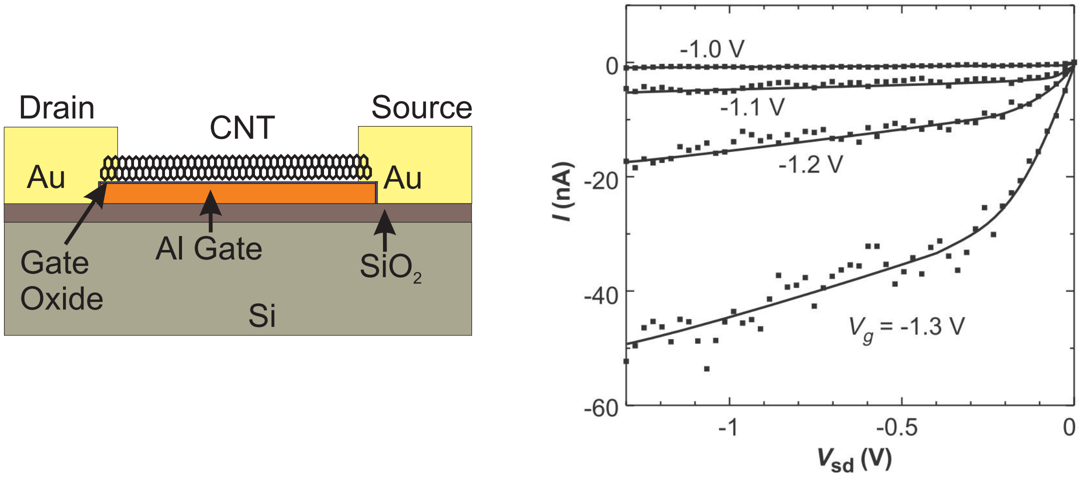

(a) (b)

Fig. 5.5: *Individual control of CNTFET using Aluminium backgate. (a) The CNT lies on the Aluminium electrode, with a thin Aluminium oxide layer acting as the gate oxide. (b)* $\mathrm{I_D - V_D}$ *characteristics of the device in (a). Reproduced from [102].*

its main advantage stems from the very thin oxide layer (few nanometres) which does not have to be deposited or grown but forms naturally. This increases the electrostatic coupling of the gate potential with the CNT energy bands and lowers the threshold voltage of the CNTFET. The reduction in the threshold voltage is evident in a comparison between Fig. 5.5(b) and the conventional back gated CNTFET characteristics in Fig. 5.3. The disadvantage of using a naturally grown oxide is the lack of control on the oxide thickness and quality as is possible with grown or deposited oxide layers in a top gated structure. This transistor also does not offer any protection for n-type CNTs against atmospheric Oxygen and fabrication of both n-type and p-type devices requires additional processing steps.

Developing and sustaining n-type characteristics in a CNT is of great importance to construct logic devices using CNTs. Most CNTs exhibit intrinsic p-type character, which has been attributed to adsorbed molecules, chemical groups on substrates or charge transfer from metal electrodes [103]. As a consequence, additional processing/fabrication is required to prevent a pristine CNT from developing p-type characteristics.

The simplest technique for converting a p-type CNT to n-type is to anneal the CNT in vacuum for several minutes. The anneal causes desorption of Oxygen and other chemical species from the CNT surface and induces n-type characteristics by directly modifying the metal-CNT contacts [98, 99]. This process is reversible, and the p-type character of the

CNT is reinstated on exposure to oxygen. Deryck *et al.* [98] also reported that intermediate ambipolar characteristics can be achieved by controlling the Oxygen exposure of n-type CNTs. To maintain the n-type character, it is therefore necessary to cover the CNT with a protective layer after the anneal.

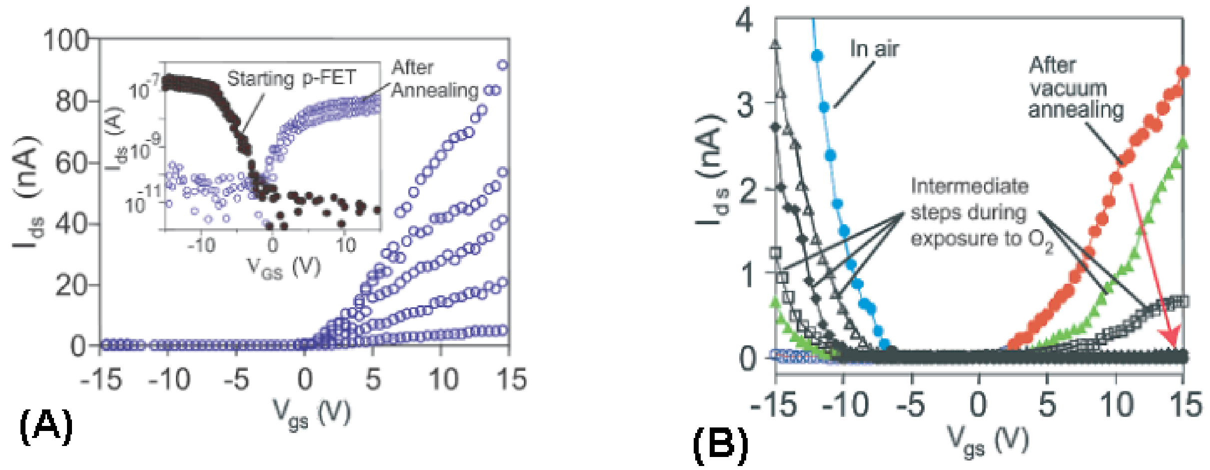

Fig. 5.6: *Conversion of p-type CNTs to n-type by annealing. (a) n-type character induced in the CNT via annealing in vacuum. The inset shows the change in characteristics from p to n-type after annealing. (b) The annealed n-type sample regains its p-type character on exposure to Oxygen, going through intermediate stages. Reproduced from [67].*

Fig. 5.6(a) shows the n-type characteristics of a CNT after annealing in vacuum. The inset in this figure shows a comparison between the initial and final device characteristics. Fig. 5.6(b) illustrates the reversibility of this process and the effect of Oxygen exposure on the n-type CNT. It shows that multiple exposure to Oxygen converts the device properties from n to p-type while transitioning through some intermediate stages where the device is ambipolar.

A second method for inducing n-type behaviour is to dope the CNT with electropositive elements, usually alkali metals. Bockrath *et al.* [104] describe a doping process for CNTs by differentially heating CNTs and Potassium placed at different ends of a vessel so that the CNTs are doped by atoms from the Potassium vapour. The Potassium atoms are adsorbed on the CNT surface and induce n-type behaviour by donating electrons to the CNT and moving the CNT Fermi level closer to the conduction band. Fig. 5.7 illustrates the change of CNT characteristics from p-type to n-type following doping with Potassium. This technique has also been used to dope one half of a CNT while shielding the other half with a PMMA layer so as to form an intra-tube p-n junction [103].

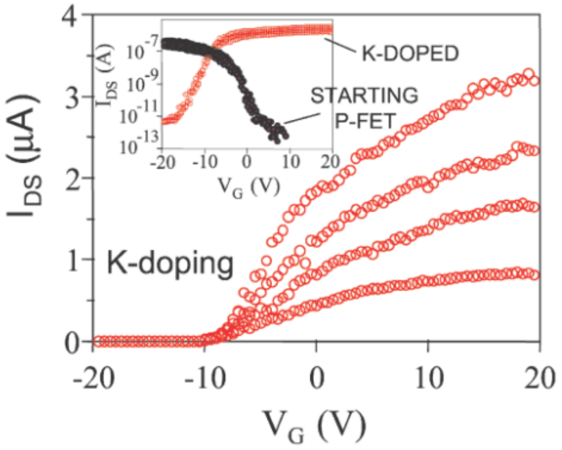

Fig. 5.7: *Change in CNTFET characteristics after Potassium doping. The inset compares the device characteristics before and after Potassium doping. The main figure shows the final n-type characteristics of the device. Reproduced from [98].*

Ambipolar characteristics have been observed in Titanium contacted CNTs passivated using a layer of SiO_2 and annealed at $T > 700$°C in an inert gas or vacuum [74]. Initially, the CNT exhibited p-type characteristics but after passivation and annealing, it allows strong currents at both positive and negative gate potentials. The change from p-type to ambipolar characteristics is explained by the desorption of adsorbed molecules from the CNT surface and formation of Titanium carbide at the metal-CNT junction. These two events lead to the formation of small barriers to both electrons and holes [67] and result in ambipolar characteristics.

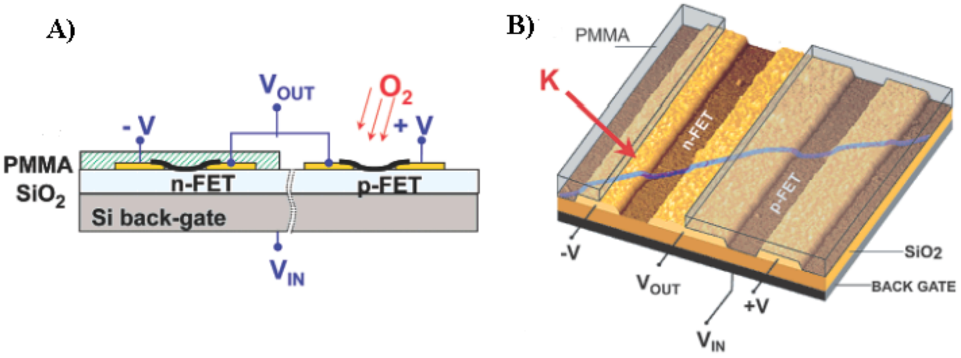

Fig. 5.8: *(a)Inter-molecular CNT NOT Gate fabricated by annealing in vacuum and then allowing one n-type CNT to revert to p-type via exposure to air. (b)Intra-molecular CNT NOT gate formed by protecting part of a p-type CNT while inducing n-type behaviour in the remainder by Potassium doping. Reproduced from [98].*

Simple inter-molecular [98] and intra-molecular [103] logic gates have been fabricated from CNTs using the annealing and doping processes discussed above. An inter-molecular CNT NOT gate was formed by annealing both the CNTFETs to convert them to n-type behaviour, depositing a protective layer over one of them and allowing the other to revert back to p-type behaviour [98]. The intra-molecular NOT gate was fabricated from a single CNT by covering half of a p-type CNT with PMMA and doping the other half with Potassium till n-type character was induced. Schematics for both these devices are shown in Fig. 5.8.

5.2.2 Spintronic devices

Spintronics is a new paradigm in electronics that aims to use electronic spin, instead of charge, for information transmission and storage. The difficulty in working with electron spin is that it can change through scattering or the influence of magnetic and electric fields. A good spintronic material is one that allows efficient injection of electrons with a specific spin and also has a long spin relaxation length over which the spin is conserved.

CNT properties such as a high charge mobility, negligible spin-orbit coupling and weak hyperfine interactions result in very long spin relaxation lengths [105] and makes them an attractive spintronic material. A majority of spintronic devices operate on the principle of magnetoresistance, wherein the resistance of a device with two magnetic layers changes depending on their relative magnetisations. The geometries of the magnetic layers are designed so as to favour certain magnetisation directions and to switch between these favoured states at different fields. Different switching fields make it possible to control the relative alignment of the magnetic layers, leading to high and low resistance states, that can then be sensed and processed. Commercial spintronic devices exploit the phenomena of Tunnel magnetoresistance (TMR) or Giant magnetoresistance (GMR) which require ferromagnet-insulator-ferromagnet and ferromagnet-metal-ferromagnet layers respectively. Since CNTs can be semiconducting or metallic, they can be used as spacer layers in both TMR and GMR devices.

The first CNT based spintronic device was demonstrated by Tsukagoshi *et al.* [68]. These were formed by contacting multiwall CNTs with Cobalt electrodes and measuring the device resistance at different temperatures and in the presence of a magnetic field sweeping between -100 mT and 100 mT. Most devices exhibited a hysteretic magnetoresistance at low temperatures (4.2 K) as shown in Fig. 5.9 with a maximum change in resistance of 9% [68].

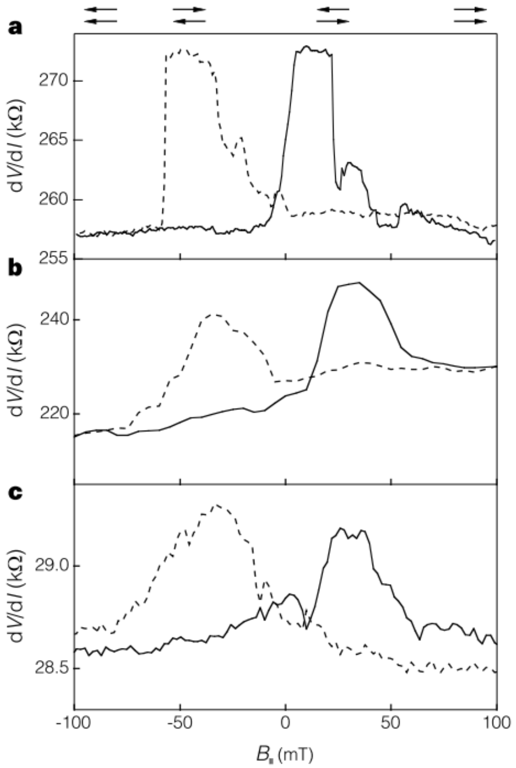

Fig. 5.9: *Hysteretic Magnetoresistance at 4.2 K in multiwall CNTs contacted by Cobalt electrodes. The low and high resistance states correspond to the parallel and anti-parallel alignment of the magnetic domains in direct contact with the CNT. Reproduced from [68].*

It is stipulated that the high resistance state is due to an anti-parallel magnetisation in the two contacts and the low resistance state corresponds to parallel magnetisation. The geometries of the contacts in this device however, were exactly the same and in theory the device should have never reached an antiparallel state at all. The experimental results bring to light the importance of the small contact area between the CNT and the Cobalt electrodes (around 30 nm), which probably includes only a few magnetic domains whose switching fields can be quite different from the bulk electrode material. This causes the two domains to switch at different fields, producing magnetoresistance from a device with symmetric contact geometries [68]. The importance of individual domains rather than the bulk makes it difficult to control the extent of the hysteresis and hence there was large variability between samples. This could be controlled by changing the structure of the Cobalt electrodes so that they behave more like a single domain material. The spin scattering length in a CNT, as estimated from this experiment is 130 nm, which is significantly longer than the 5-10nm spacer thicknesses used in current TMR/GMR devices. Other studies [106] have demonstrated magnetoresistance effects from CNTs as long as $2\mu m$. These results highlight the promise of using CNTs to fabricate long channel spintronic devices.

The current TMR/GMR devices require extremely thin spacer layers to obtain an appreciable magnetoresistance effect [106]. This precludes any control of the electrons in the spacer through the use of a gate. The long spin scattering lengths in CNTs can be used to fabricate spintronic devices with gated spacer layers to allow modification of the electron spin in the spacer layer. Such a device will be a manifestation of the Datta-Das spin transistor [107] with the general structure shown in Fig. 5.10.

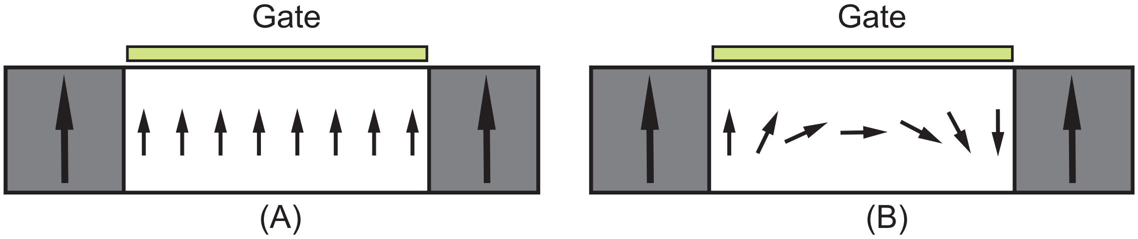

Fig. 5.10: *Operation of a gated spintronic device.(a) With no gate influence, the electrons from the two parallel aligned ferromagnets travel through the device without changing spin, resulting in a low resistance state. (b) The electron spin is flipped by the gate influence and a high resistance state is observed due to anti-parallel alignment between the conduction electrons and the second ferromagnetic electrode.*

This device would use the gate electrode and the electron spin precession caused by electric [107] or magnetic [108] fields to modify the electron spin during transit through the channel between the ferromagnetic electrodes. Such control will achieve the magnetoresistance effect by aligning the channel electrons parallel or antiparallel to the destination ferromagnetic electrode instead of changing the magnetisation of the entire ferromagnetic electrode itself. This will make spintronic devices more efficient as modifying the electron spin in the channel is less expensive in terms of energy compared to flipping the bulk electrode magnetisations.

A second interesting effect that could favour the use of CNTs in spintronic devices is the complete decoupling of spin and charge currents in one dimensional conductors [109]. This effect allows measurement of a signal voltage between a spin injector and a detector without a net charge current flow between these electrodes. This is a diffusion based effect and is therefore more pronounced in one dimensional structures due to the restricted number of directions for electron diffusion. The one dimensional structure of CNTs, coupled with their electronic properties make them good candidates for devices exploiting this effect. Initial results on such a device have been presented by Tombros *et al.* [110].

As with their counterparts using charge based electronics, the contact properties of various ferromagnets and CNTs are of great importance for spintronic devices [111]. Electrical and magnetoresistance measurements have been performed on CNTs contacted by ferromagnetic materials like Co [68], Fe [112], Ni [113] and PdNi [114, 115]. These materials have exhibited varying degrees of electrical as well as magnetoresistance, but reliably low contact resistances were obtained by Sahoo *et al.* [114] using PdNi alloys as electrodes in back gated CNT spintronic devices. The choice of PdNi was primarily due to the good quality Pd-CNT contacts [75] and the fact that addition of a few ferromagnetic impurities was sufficient to make the alloy ferromagnetic in character.

Subsequent sections describe the fabrication of field effect transistors with a CNT as the channel, contacted by electrodeposited PdNi electrodes. The suitability of electrodeposited PdNi contacts to CNTs is investigated via electrical characterisation.

5.3 Experimental Details

5.3.1 Carbon nanotube transistor fabrication Process

The CNTs used for device fabrication in this study were commercially sourced from Cheaptubes Inc., USA and were produced using Chemical Vapor Deposition (CVD). The CNTs were dispersed in 1,2-dichlorobenzene using sonication and Carbon nanotube field effect transistors (CNTFETs) were fabricated using this dispersion as shown in the process diagram in Fig. 5.11.

A $\langle 100 \rangle$, 1.39-1.41 Ω.cm Silicon wafer was used as the substrate for the CNTFETs (Fig. 5.11(a)). A 300 nm Aluminium back contact was evaporated on the Si wafer and was followed by an anneal at 300°C to form the ohmic back contact that acts as the gate (Fig. 5.11(b)). A 20 nm Silicon oxide layer was thermally grown on the wafer surface to serve as the gate oxide (Fig. 5.11(c)). The CNT dispersion was then spun onto the wafer using a standard photoresist spinner (Fig. 5.11(d)). This was immediately followed by spin coating a layer of photoresist and defining patterns by photolithography using an EVG620TB mask aligner (Fig. 5.11(e)). After development (Fig. 5.11(f)), the underlying SiO_2 in the opened windows is etched by dipping in buffered 20:1 HF (Fig. 5.11(g)) and rinsing with DI water. Assuming that a CNT is aligned such that it bridges the gap between two contacts, at the end of this step the central section of the CNT is shielded by the photoresist and separated from the Silicon substrate by the thermal oxide. The ends of the CNT, on the other hand are exposed and positioned in the developed contact patterns. The sample is

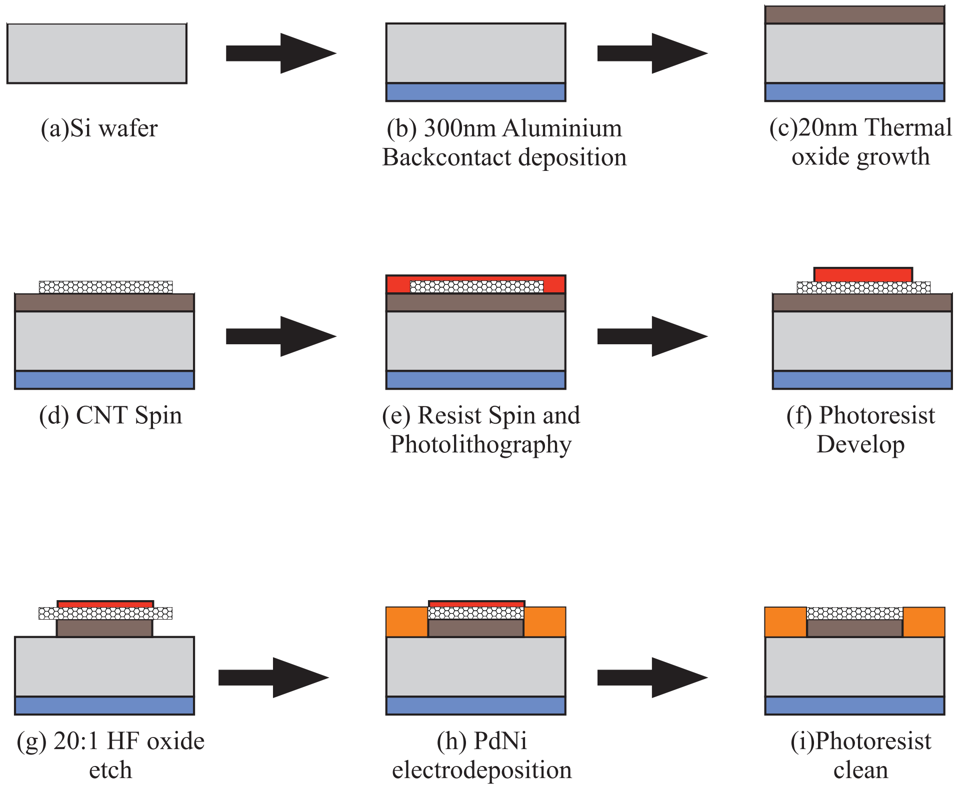

Fig. 5.11: *Fabrication process for CNT transistors by spin coating a CNT dispersion and electrodepositing* $Pd_{0.59}Ni_{0.41}$ *contacts.*

then immersed in an electrochemical bath and the PdNi contacts are electrodeposited (Fig. 5.11(h)). The photoresist layer performs the dual role of preventing metal deposition on the central CNT section and holding the CNT in place on the substrate during the HF etch and the electrodeposition process. A $\mathrm{Pd_{0.59}Ni_{0.41}}$ alloy is deposited in the windows and the two ends of the CNT are embedded in the metal film, to form end bonded contacts. Finally, the resist is carefully washed off with Acetone leaving the electrodeposited contacts holding down the contacted CNT(s) and forming a three terminal transistor (Fig. 5.11(i)).

It is evident that this process does not involve any directed CNT placement but instead relies on chance that a CNT will bridge the gap between any two contacts. A number of CNTs may also be rendered useless if they are deposited under the contact pads or positioned such that only one end of the CNT is contacted by electrodeposited metal. The probability of CNTFET formation can be increased by ensuring a high density of both CNTs and contact pads. The surface density of the CNTs depends on the CNT concentration in dispersion and the density of the contacts are governed by the mask design, making both these parameters critical to the process.

5.3.2 Mask Design

The mask was designed to partition the Silicon wafer into 8 mm × 5 mm chips containing a collection of bondpads and tracks to contact any CNTs in their vicinity. To maximise the probability of contact, the active area was extended to the whole chip except for a 0.5 mm boundary on the outside of the rectangle, which served to demarcate neighbouring chips and as a guide during cleaving.

Two kinds of patterns were designed for the bond pads and the tracks and are shown in Fig. 5.12. Since the area under the contact pads do not contribute to forming a useful CNT contact, the contact pads were made small (50 μm× 50 μm) and were placed as close to each other as possible. Part of the wafer was also devoted to patterns with larger contact pads (100 μm× 100 μm) to allow for wirebonding.

Fig. 5.12(b) includes a close up view of the fingers defined in the patterns. The fingers are where the metal tracks have the lowest separation from each other and any CNT in this region is likely to contact the metal layers. The distance between the tracks (d) is varied to form devices with different CNT channel lengths. Different values of the track width (w) are used so that the mask can be used for devices incorporating in-situ grown CNTs, in which the larger window sizes provide more growth sites. The low reverse bias PdNi-Si Schottky diode currents can be used to suppress any leakage caused by the direct PdNi-Si contact, even for relatively large areas of the metal film. The patterns were therefore designed as monolithic structures to be deposited in a single process step instead of minimising the PdNi-Si contact area via a more complex multi step process.

The patterns described in Fig. 5.12 with varying values of track separation (d) and track size (w) were placed on each chip, along with numerical identifiers to easily locate each device through an optical microscope. A section of the active area of the chip is shown in Fig. 5.13. This section was repeated so as to cover the entire area of the chip.

5.3.3 Carbon nanotube dispersion and spin coating

Several studies have examined the dispersion of CNTs in various polar and non polar solvents [49, 51, 116]. Pure CNTs are non polar molecules and are found to disperse better in non polar solvents. If the use of polar solvents is necessary, then surfactants such as Sodium dodecylsulphate (SDS) or Triton-X have to be used to overcome the attractive inter-tube Van der Waal's forces.

The CNTs were dispersed in non polar 1,2-dichlorobenzene (DCB) due to its superior dispersion ability among non polar solvents, as demonstrated by Bahr *et al.* [49]. The

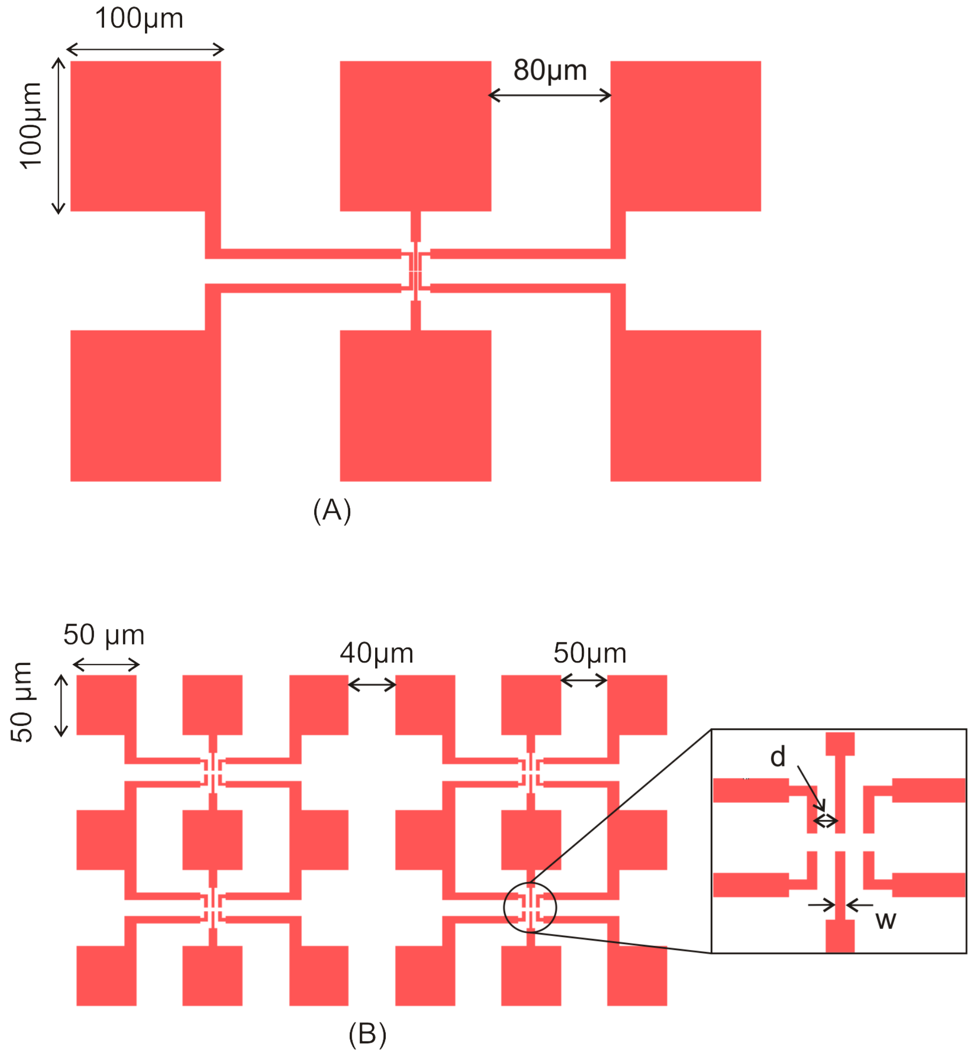

Fig. 5.12: *Layouts of pads and tracks described on the mask to form CNT contacts. (a)* 100 *µm* × 100 *µm Square contact pads with tracks to provide larger contact areas for electrical probing. (b) The smaller* 50 *µm* × 50 *µm contact pads and tracks designed to increase contact density on the chip. The close up view shows the region of nearest approach of the tracks and is the same design for both contact sizes. The separation between tracks 'd' and the track thickness 'w' are varied to provide different contact areas and CNT channel lengths.*

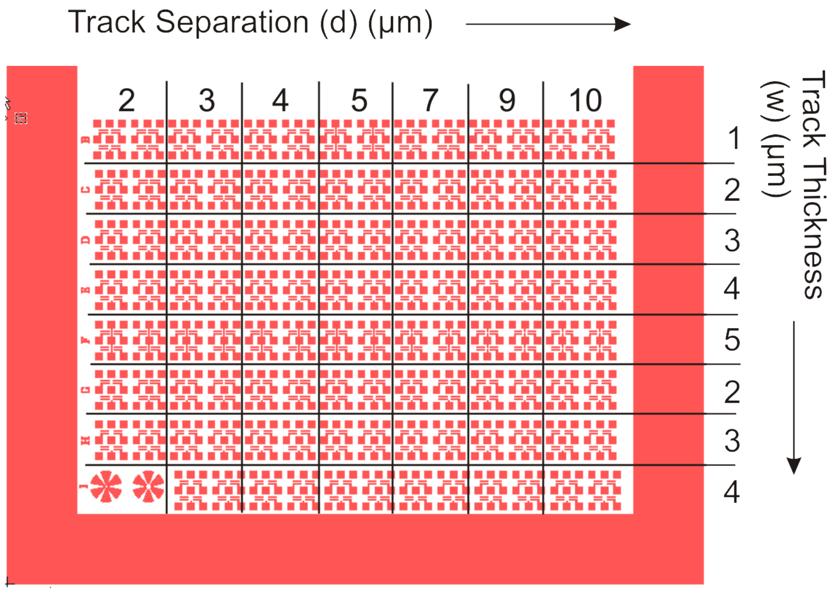

Fig. 5.13: *A section of the active area of the chip showing the variation in the track separation and track width. This set of contacts was repeated over the entire chip area to maximise the contacting probability.*

first dispersion was prepared by adding a small amount (<1 mg) of dry CNT powder to 10 ml of 1,2-dichlorobenzene followed by sonication for 45 mins. As per the study by Bahr *et al.* [49], this dispersion is close to the saturation limit for dispersing CNTs in 1,2-dichlorobenzene and a black coloured dispersion was formed with the presence of some particulates. After a few trials, the solution was topped up to 10 ml by an additional 4 ml of 1,2-dichlorobenzene, followed by sonication for 30 to 45 minutes. The dispersion was quite stable with no precipitation observed for weeks after preparation.

The CNT dispersion was initially spin coated on small Silicon chips and scanning electron microscope (SEM) images of one chip surface is shown in Fig. 5.14(a).

As can be seen from Fig. 5.14(a), there is a high density of deposited CNTs as well as a large quantity of particulate debris on the surface. The debris could be clumps or ropes of CNTs not separated by sonication or impurities such as metal catalysts or ash, remnants from the CNT growth process. Some of these particles were large enough (macroscopic) to interfere with the photoresist flow during spinning and adversely affected the uniformity and spread of the photoresist, resulting in extremely poor feature reproduction. To improve the photolithography, the sonicated CNT dispersion was filtered through a Whatman 2.5 μ.m filter paper and the filtered solution was spun onto the Silicon substrate. The filtration step reduced the number of large particulates as seen in Fig. 5.14(b). The number of CNTs was also reduced, but a significant number of CNTs were deposited on the substrate.

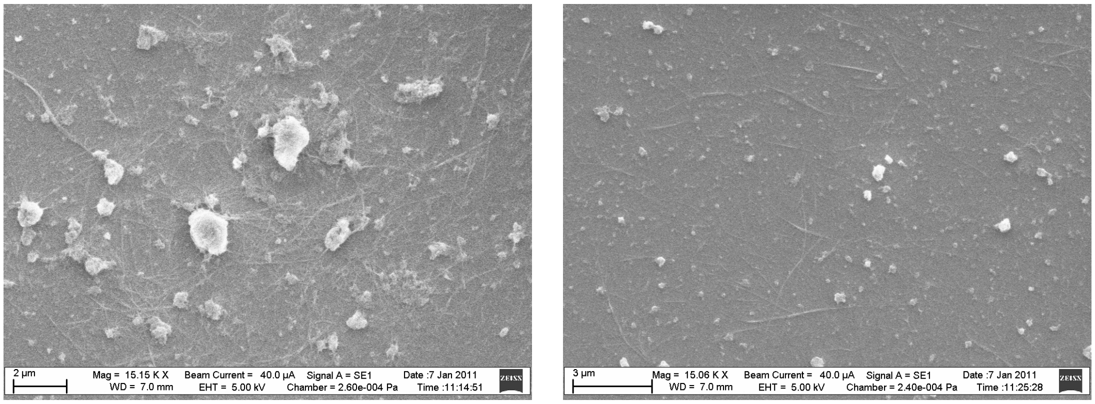

Fig. 5.14: *SEM image of spin coated CNTs on Silicon using (a)unfiltered CNT dispersion and (b)dispersion filtered through a 2.5 µm filter paper. The filtered dispersion shows a reduction in the quantity of debris present on the Silicon surface as compared to the unfiltered dispersion.*

Filtering the dispersion hugely improved the uniformity of the photoresist coating and the reproduction of the mask features.

After spin coating the dispersed CNTs on the Silicon surface, the metal electrodes were deposited as per steps (e) to (i) in Fig. 5.11. The PdNi alloy was electrodeposited from a 44.4 g/L $NiSO_4$ and 11.1 g/L $Pd(en)Cl_2$ bath. A pulse of -1.5 V was applied for 0.1 s and was followed by deposition at -0.9 V and a current density of about 4 mA/cm^2. After deposition, the chip was rinsed with DI water, blown dry and the excess photoresist was removed by gently rinsing with Acetone and isopropyl alcohol (IPA). Planar SEM images of the CNT transistors fabricated by this process are shown in Fig. 5.15.

Despite the high concentration of CNTs in the dispersion and a high density of contact patterns, the yield of devices with an interconnecting CNT was quite low. A total of only about ten working devices out of a possible maximum of about three hundred were obtained from one fabricated chip. Other problems included non reproducible electrical characteristics and soft metal electrodes which were damaged easily during measurement, a problem also reported for transistors with Palladium electrodes [75].

5.4 Electrical Characterisation

A schematic of the fabricated device is shown in Fig. 5.16 and is similar to many back gated CNT transistors described in other studies [67, 72]. One major difference is that the electrodeposited $Pd_{0.59}Ni_{0.41}$ films are in direct contact with both the Silicon and the CNT,

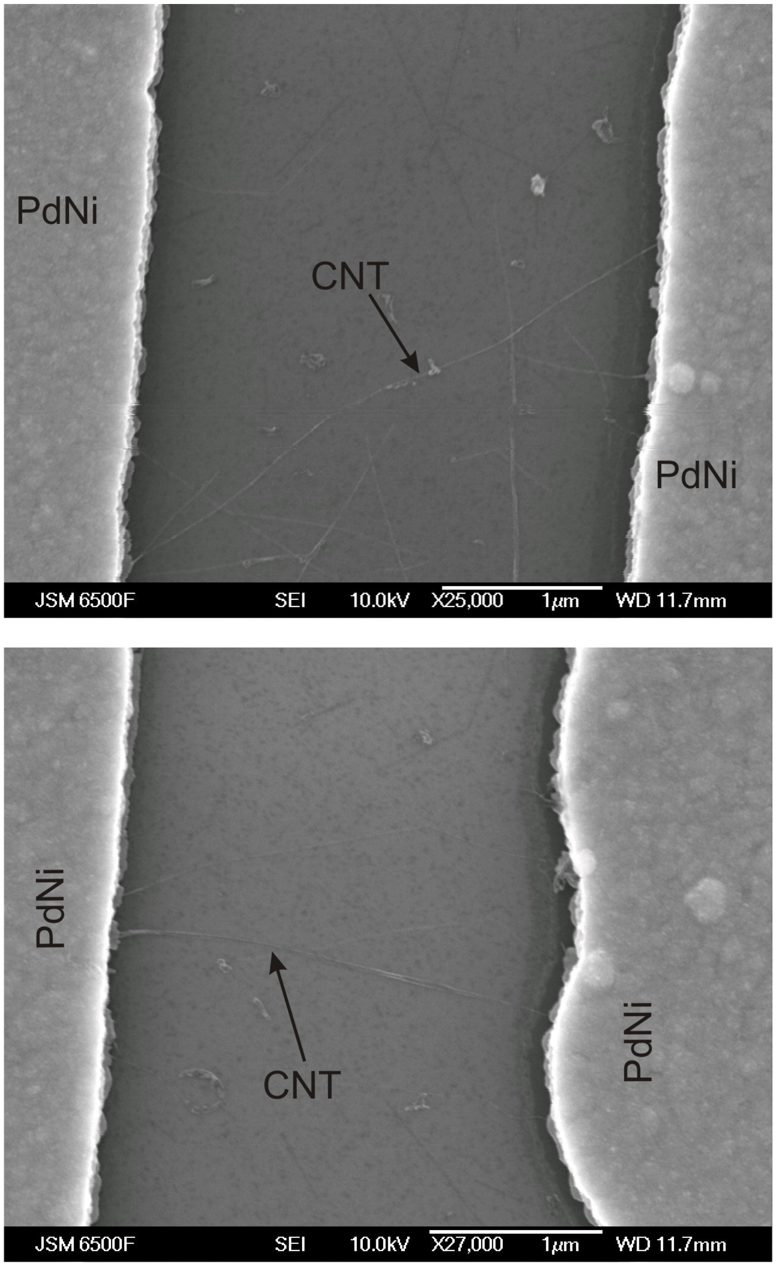

Fig. 5.15: *SEM images of CNTs contacted by* $Pd_{0.59}Ni_{0.41}$ *electrodes. At least one CNT is seen to contact both the PdNi electrodes. More than one CNTs are present but only one bridges the gap between the contacts.*

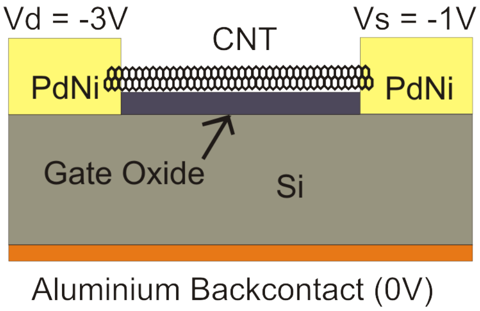

Fig. 5.16: *Schematic of the CNT transistor and example of a biasing scheme to suppress leakage current through the substrate. The potentials of the three contacts are chosen to ensure that the* $Pd_{0.59}Ni_{0.41}$*-Si Schottky barriers are always reverse biased.*

which creates a possible leakage path through the underlying Silicon. The Aluminium back contact is primarily used to suppress the leakage current through this path by maintaining both the PdNi-Si Schottky diodes in reverse bias. The low reverse bias currents of the PdNi-Si Schottky diodes as reported in Chapter 2 suppress the leakage currents and ensure that most of the current between the two PdNi electrodes is driven through the CNT.

The biasing scheme shown in Fig. 5.16 was used to suppress the leakage current. The gate potential was always maintained higher than that of the source and drain and a potential drop is created across the CNT by making the drain potential more negative than that of the source. All electrical measurements were performed using a DC prober and an Agilent 4155C semiconductor parameter analyser. Some of the results obtained from the electrical characterisation are shown in Fig. 5.17.

Fig. 5.17(a) and Fig. 5.17(b) show the dependence of the drain current (I_d) on the drain voltage (V_d) at fixed gate potentials for two different sets of transistors. The currents in one set, plotted in Fig. 5.17(a) are about 5 orders of magnitude higher than those measured in the second set, plotted in Fig. 5.17(b). The currents in Fig. 5.17(b) are all at most a few hundred picoamperes, which is the same as the noise levels in the parameter analyser and it can be concluded that no CNT exists between the source and drain contacts of this transistor. The much higher currents in Fig. 5.17(a) on the other hand suggest the presence of a CNT channel between the source and drain. The resistance of the transistors shown in Fig. 5.17(a) are in the 275 k$\Omega -$ 2.8 MΩ range and show no rectification because both Palladium and Nickel, by dint of being high workfunction metals, form ohmic contacts to the CNT valence band [75, 80]. This resistance range is similar to that observed by Javey *et al.* [75] for Palladium contacted semiconducting CNTs and significantly lower than those observed by Mann *et al.* [76] for Palladium contacted metallic CNTs. However,

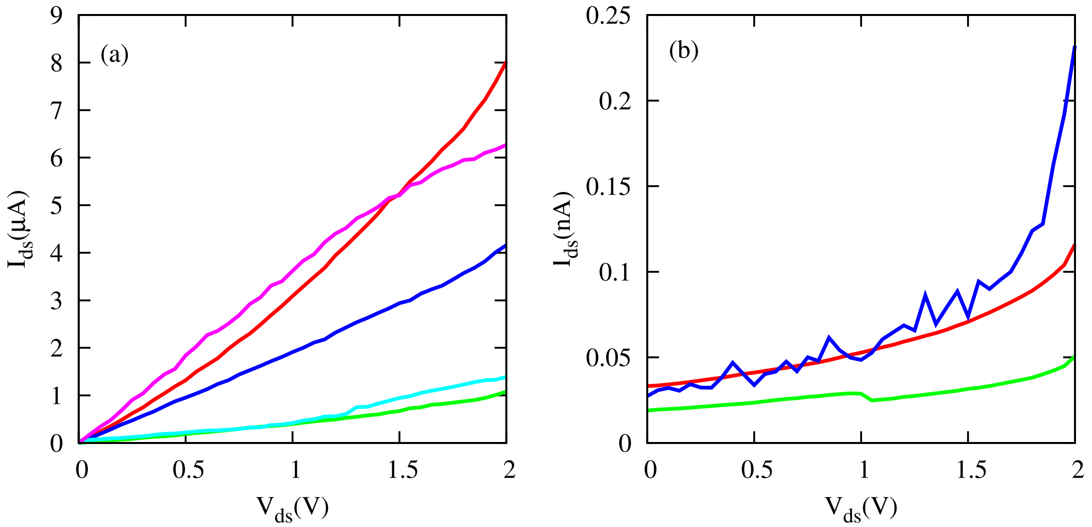

Fig. 5.17: $\mathrm{I_{ds}} - \mathrm{V_{ds}}$ *characteristics at* $\mathrm{V_{gs}} = 1$ V *for (a)five transistors with a CNT channel between* $Pd_{0.59}Ni_{0.41}$ *electrodes and (b)three transistors without a CNT channel between* $Pd_{0.59}Ni_{0.41}$ *electrodes. The devices with a CNT channel show significantly higher currents compared to those without. No rectification is observed in (a) because both Pd and Ni are high workfunction metals and form ohmic contacts to the CNT valence band.*

the PdNi contacted CNT transistors showed lower resistances at zero gate potential than those contacted by Gold [72, 99] and Titanium [100]. A number of factors such as the local alloy composition near the CNT and the presence of impurities could be the reason for higher device resistances. It is possible that the alloy in the neighbourhood of the CNT is richer in Nickel and therefore the contact quality is not as good as a Palladium-CNT contact. The small dimensions of the CNT make it especially susceptible to local variations in composition or presence of small quantities of impurities that would be inconsequential in bulk contacts. While it can differentiate whether the metal-CNT contact is ohmic or Schottky in character, the $\mathrm{I_d} - \mathrm{V_d}$ characterisation at gate potential of 0V does not reveal any information about the nature of the CNT.

The usual technique for differentiating between metallic and semiconducting CNTs in such a transistor structure is to study the source-drain current ($\mathrm{I_{ds}}$) over positive and negative gate potentials. CNTs have been shown to be inherently p-type in air and a transistor formed from a p-CNT has a negative threshold voltage, beyond which they conduct high currents while remaining off for all other gate potentials. Back gated transistor structures require especially high negative gate potentials due to the presence of the semiconductor substrate as well as the gate oxide between the gate electrode and CNT. The transistors studied by Javey *et al.* [75], which are structurally similar to those used in this work, recorded their lowest resistances at gate potentials between -10 to -20 V. For metallic CNTs the gate potential is irrelevant due to the absence of a band gap, and they should exhibit similar resistance values for all gate potentials [76].

The gate dependence of one of the devices from Fig. 5.17(a) is shown in Fig. 5.18(a) and highlights the problem. The measured currents through each terminal is shown so that all current paths in the device can be identified. During this measurement, the drain (V_d) and source (V_s) potentials were fixed at -2 V and 0 V respectively while the gate potential (V_g) was swept from -2 V to 2 V. This causes the source-gate Schottky barrier to be forward biased for $V_g \leq 0$ V and a large current flows between the source and gate, as shown by the traces for (I_s) and (I_g) in Fig. 5.18. As V_g rises above 0 V to positive potentials, the source-gate Schottky barrier becomes reverse biased and the gate current drops to a few nanoamperes in both graphs of Fig. 5.18, showing that negligible currents flow through the PdNi-Si Schottky diodes. Fig. 5.18(a) shows that a current of the order of a few microamperes, similar in value to those observed in Fig. 5.17(a), starts to flow between the source and drain. This current cannot be flowing through the Silicon because both Schottky diodes are reverse biased. The large source to drain current therefore conclusively proves

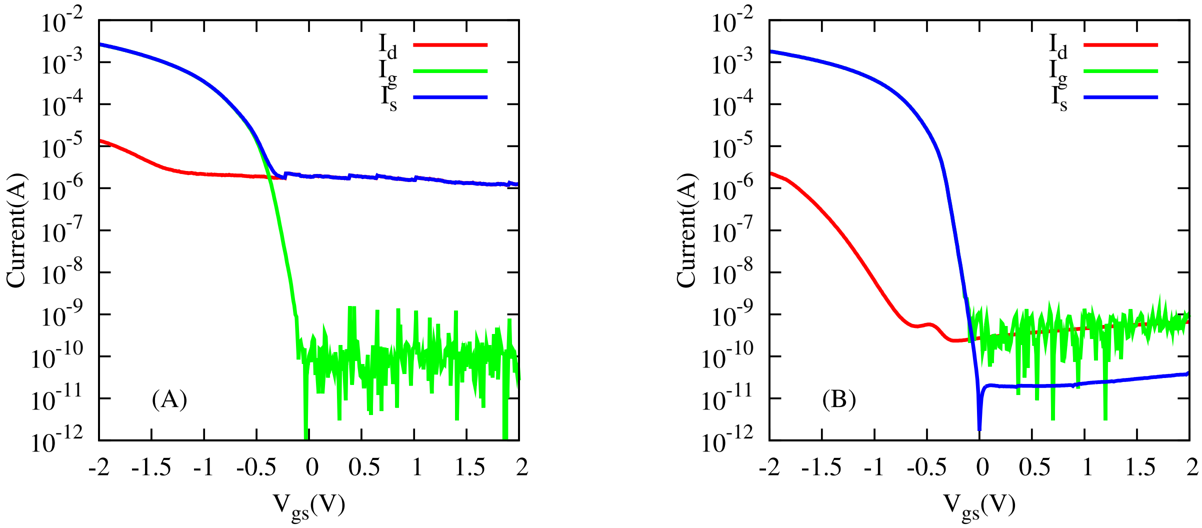

Fig. 5.18: *Variation of* I_d, I_s *and* I_g *with* V_{gs} *at* $V_{ds} = -2$ V *for devices (a)with CNT channels and (b)without CNT channels. The match between* I_d *and* I_s *for positive* V_{gs} *values in (a) shows the presence of a current conduction path between drain and source and indicates the presence of a CNT. The large current for negative* V_{gs} *in both graphs is due to the forward biased source-gate Schottky diode.*

the presence of a CNT between the source and drain.

The gate dependence of a second device is shown in Fig. 5.18(b). In this figure the source and gate currents match each other for negative gate potentials, but the values of all three currents are in the nanoampere region for positive gate potentials. These current levels correspond well with the reverse bias currents of the PdNi-Si Schottky barriers. The high resistance of the drain to source path shows that the current in this case is flowing through the Silicon due to the absence of a connecting CNT. These graphs show that for a back gated CNT transistor, the most reliable measurements of CNT current are when the gate bias is higher than both the source and drain potentials.

Fig. 5.18 highlights a significant problem in back gated CNT transistors with electrodeposited source and drain contacts. For gate potentials lower than either the source or the drain potentials, at least one Schottky diode in the structure is forward biased, causing a large leakage current to flow through the diode and into the gate. This current dominates the smaller CNT current and makes it impossible to determine the CNT's electrical characteristics at negative V_{gs} values. A functional CNT transistor with electrodeposited contacts will therefore have to be designed as a four terminal device with independent gate and body terminals so that gate control can be achieved while maintaining both electrodeposited Schottky barriers in reverse bias. Possible manifestations could use a top gated structure [100] or a back gate independent of the Silicon substrate [102] as shown in Fig. 5.2.1. An alternative method to differentiate between semiconducting and metallic CNTs is possible by modulating the PdNi-CNT contacts by changing the PdNi Fermi level via Hydrogen exposure.

5.5 Magnetic characterisation

The electrical characteristics of the CNT transistors were measured at room temperature in the presence of a changing magnetic field to investigate the presence of magnetoresistance. The measurements were performed using a Lakeshore EMTTP4 probe station with a built in electromagnet. The field was varied between -400 G and +400 G at a rate of 40 G/min and the forward and reverse currents were recorded. The current through the CNT was measured by maintaining the transistor drain at -1 V and both source and back gate terminals at 0 V. Fig. 5.19 shows the measured current as a function of the field. The current is seen to be noisy and no obvious changes in resistance are observed. The largest magnetoresistance values reported using CNTs are about 9% [68] at 4.2K with typical values being 2 to 4% [114, 117], also recorded at low temperatures. These resistance

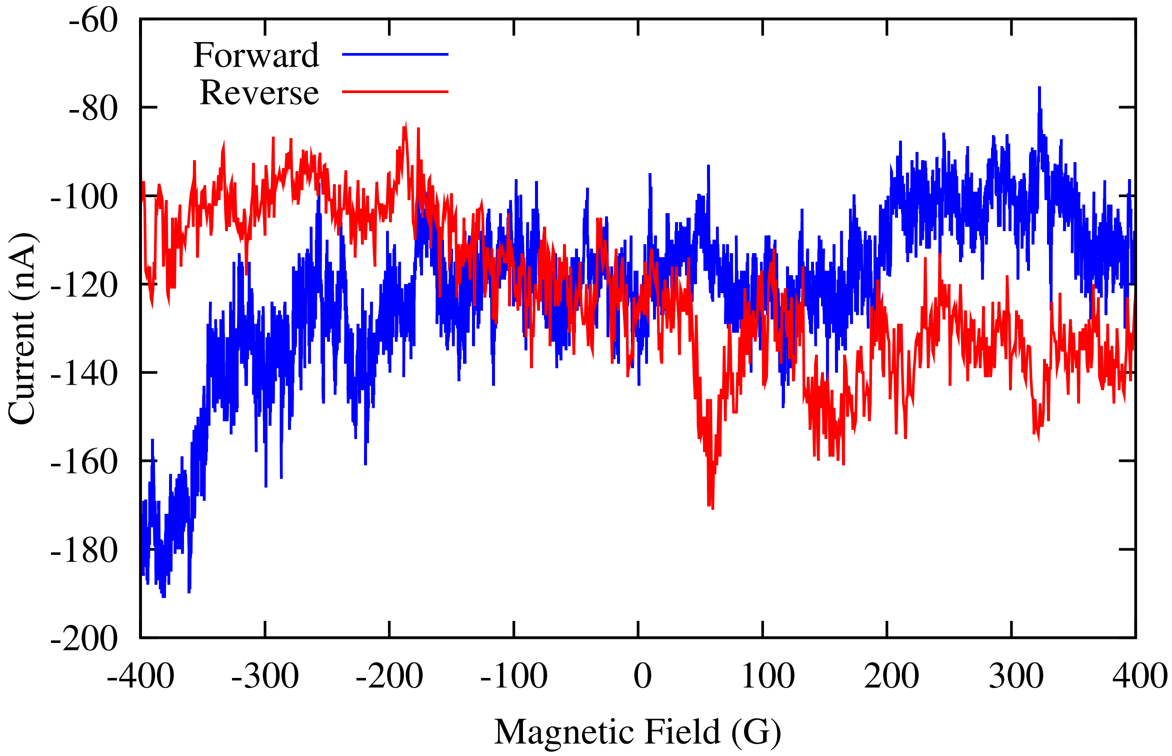

Fig. 5.19: *The CNT transistor current variation in a changing magnetic field. The noise level in the current is between 10 to 15%, which is large enough to obscure the magnetoresistance signal.*

changes are small enough to be obscured by the noise in the current signal. Additional low temperature measurements on the transistor characteristics and a reduction in the noise levels are necessary to investigate the magnetoresistive properties of CNTs contacted by electrodeposited PdNi.

Electrical measurements in a sweeping magnetic field were performed at a temperature of 80 K for both semiconducting and metallic CNTs and the results are plotted in Fig. 5.20 (semiconducting) and Fig. 5.21 (metallic). The noise levels in the device with the semiconducting CNT is still seen to be about 10%, which is higher than expected magnetoresistance values from such a CNT device. The noise levels for the metallic CNT is significantly lower, but no distint magnetoresistance is observed in either device. There are many possible explanations for the absence of magnetoresistance from the characterised devices. One possibility could be the symmetrical design of the two PdNi contacts, which will result in the bulk PdNi magnetisation switching at roughly the same magnetic field. There is a possibility that the magnetic domains in direct contact with the CNT switch at

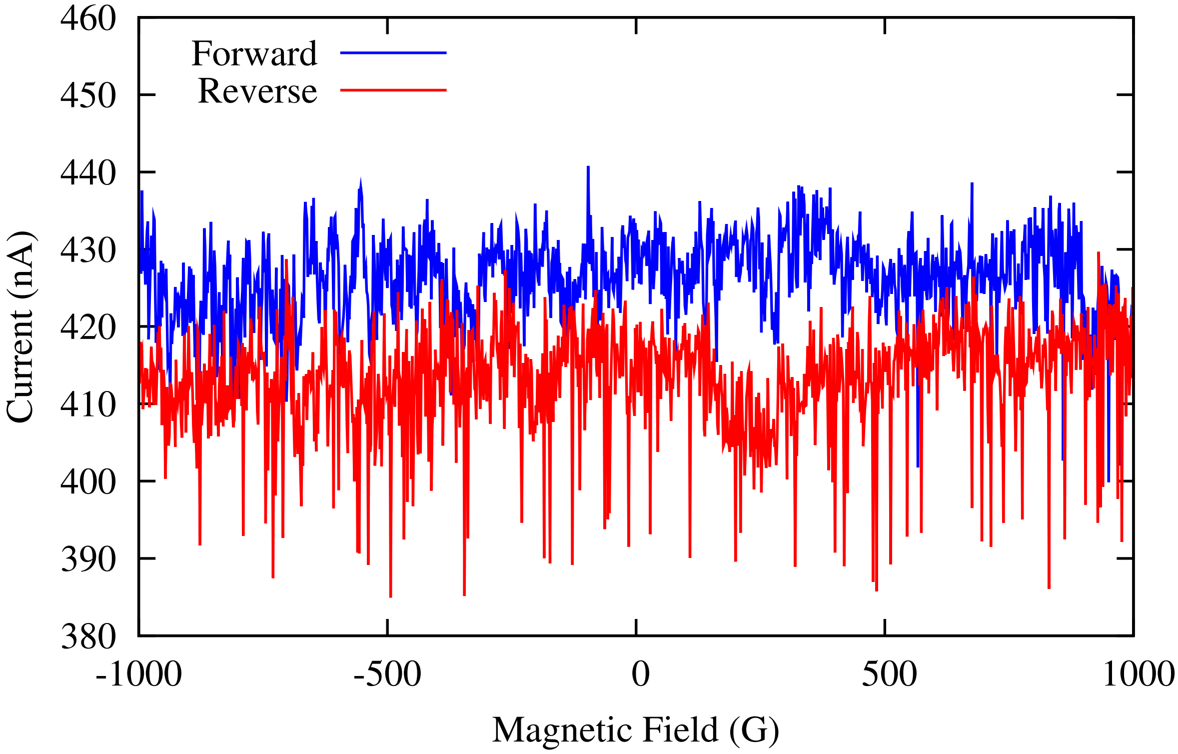

Fig. 5.20: *Electrical characteristics of the PdNi contacted semiconducting CNT at 80 K and in a sweeping magnetic field. The noise level in the current is around 10%, which is large enough to obscure the magnetoresistance signal.*

different fields but this did not produce any magnetoresistance in this case. The semiconducting CNT is seen to be curved in Fig. 4.10, which is indicative of defects in the CNT lattice. These defects can reduce the spin lifetime and diffusion length of the conducting electrons by acting as scattering sites. The estimated spin lengths of electrons in CNTs is also estimated to be a few hundreds of nanometres [68], with the longest spin length estimated to be between 1 to 2 μm [106]. The CNTs in this study are longer than 3 μm the spin diffusion length is probably not sufficiently long to produce magnetoresistance in these CNTs. The measurement technique in this study used non bonded probes in physical contact with the PdNi metal that was bonded to the CNTs. Such an arrangement will yield lower signal to noise ratio (SNR) compared to wire bonded probes due to external vibrations to the system, especially due to the pumping required during low temperature measurements. Finally, most reported results of magnetoresistance are observed at temperatures between 4.2 and 5 K, while the lowest temperatures used in this work was 80 K. Designing devices to address these issues and performing measurements at lower tem-

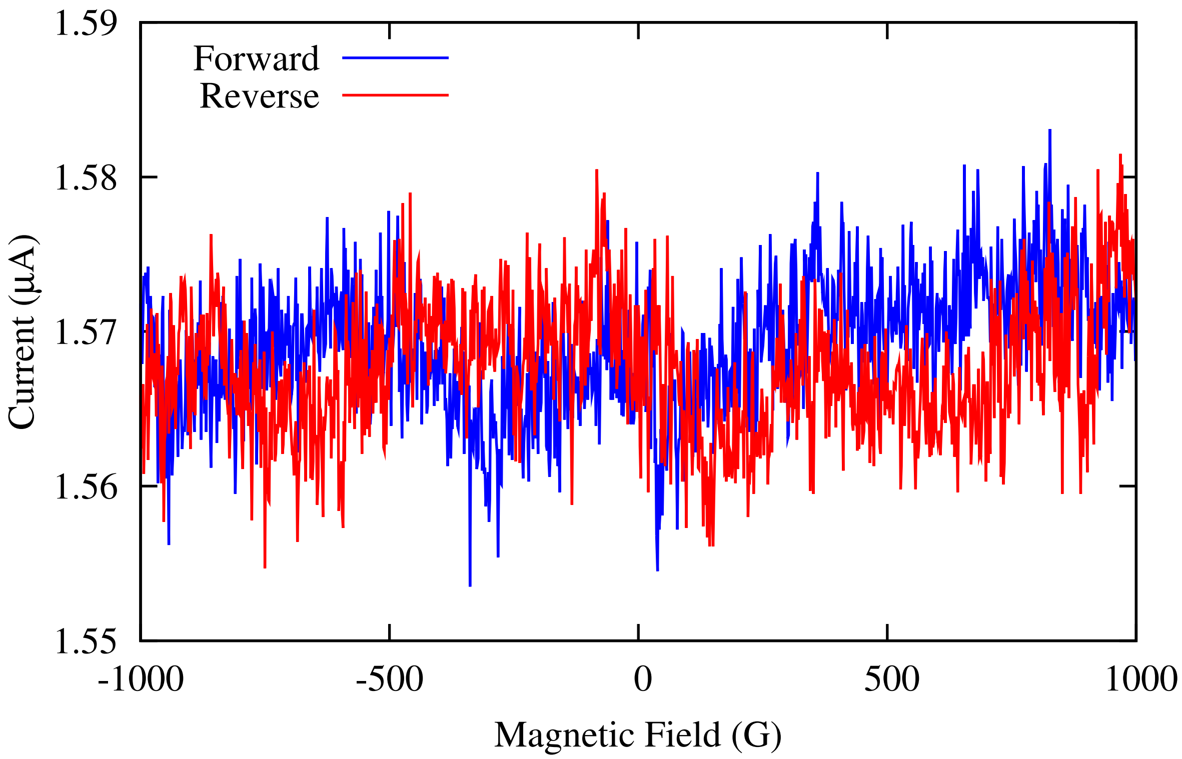

Fig. 5.21: *Electrical characteristics of the PdNi contacted metallic CNT at 80 K and in a sweeping magnetic field. The noise level is significantly lower in this device, but no magnetoresistance effect is observed.*

peratures will allow estimation of the magnetoresistance effect for CNTs contacted with electrodeposited PdNi electrodes.

5.6 Conclusion

The fabrication process and electrical characterisation of back gated CNTFETs incorporating electrodeposited PdNi contacts are presented. The electrical characteristics of the CNTFET at zero gate potential show that the contact resistance of the PdNi-CNT is superior to that observed with Gold and Titanium, similar to that between Palladium and semiconducting CNTs and inferior to previously described Palladium and metallic CNT contacts. The direct contact between electrodeposited PdNi and the Silicon substrate creates a possible leakage path for the current but this path is suppressed by the low reverse bias currents of the PdNi-Si Schottky diodes. The presence of the PdNi-Si Schottky diodes does not allow the use of negative gate voltages and therefore this CNTFET cannot be characterised over a range of positive and negative gate potentials. This is a disadvantage of back gated CNTFETs incorporating electrodeposited source and drain electrodes and can be eliminated by using a four terminal architecture that separates the gate and substrate terminals. This will yield more data on the suitability of the electrodeposited PdNi as an electrode material for CNTFETs.

6. CONCLUSIONS

Incorporation of new materials and processes into fabrication of electronic devices requires a thorough understanding of the material properties, the process parameters and the properties of interfaces formed with other components of the device. In this PhD, the use of electrodeposition, a nonstandard fabrication process, to contact Silicon and CNTs is examined. The detailed description of the electrodeposition process and the characteristics of the electrodeposited PdNi-Si and PdNi-CNT contacts are presented. The use of the PdNi-Si and PdNi-CNT contacts in fabricating electronic devices is also described.

A process for electrodepositing PdNi alloys with controlled Nickel content onto Silicon is presented. The bath composition and deposition potential primarily determine film composition and it is possible to deposit an alloy with a wide range of compositions from the same bath by changing the deposition potential. The composition of the deposited PdNi film can be predicted from the Nickel and Palladium currents at the chosen deposition potential. The deposited PdNi films are ferromagnetic with their saturation magnetisation increasing with Nickel content. Excellent PdNi-Si Schottky barriers are formed, with very low reverse bias currents, on/off currents differing by about six orders of magnitude and no breakdown till -3 V. The ferromagnetic character of the alloys and the formation of a PdNi-Si Schottky barrier make the electrodeposited PdNi films suitable for use as electrodes in spintronic devices.

The method used to characterise the PdNi electrodeposition is directly transferable for electrodepositing other alloys. One possible extension of this technique is the electrodeposition of multilayered PdNi stacks with varying Nickel content in each layer. This can be achieved by changing the deposition potential during deposition to tailor the composition of the layer being deposited. Each layer then contributes a specific attribute towards the properties of the stack as a whole. For instance, a PdNi stack for Hydrogen sensing could have a Nickel rich layer closest to the Silicon substrate to improve adhesion and robustness, with a top layer rich in Palladium to facilitate Hydrogen dissociation.

The fabrication and electrical characterisation of a low power Hydrogen sensor based on back to back electrodeposited PdNi-Si Schottky barriers were described. The back to back architecture ensures low power operation for all applied biases by restricting the sensor current to the reverse bias currents of the PdNi-Si Schottky diode. The sensor was placed in a vacuum chamber and its response to different Hydrogen partial pressures was recorded. A very low idle current of between 1 to 2 nA and excellent selectivity are observed, with the sensor exhibiting a large percentage current change in response to Hydrogen, with no response to pure Nitrogen or air. The smallest Hydrogen partial pressure detected was 3 mbar and the highest sensitivity was found to be around 17 nA/mbar. The current saturation and recovery times were long but no irreversible damage was observed from multiple exposure to and evacuation from the Hydrogen environment.

Improving the current saturation time is the next step in developing this Hydrogen sensing technology. Possible methods of accomplishing this could be to reduce the thickness of the film or to clean the PdNi film surface before measurements to speed up the absorption and diffusion of Hydrogen through the PdNi film. Another possibility is to measure the sensor response at elevated temperatures, which will reduce the Hydrogen solubility and may result in faster saturation times, albeit with smaller current increases. Investigating the sensor response to other gases such as Hydrogen sulphide (H_2S) and dissolved Hydrogen is also a promising research direction. Research on deep sea hydro thermal vents has a specific need for a sensitive, low power and reliable Hydrogen sensor. The suitability of the electrodeposited PdNi Hydrogen sensors can be gauged by packaging the sensor and electrically characterising it for different dissolved Hydrogen concentrations.

A novel technique for differentiating between semiconducting and metallic CNTs via electrical measurements in air and Hydrogen was demonstrated. PdNi contacted CNTs were exposed to Hydrogen, which modifies the PdNi workfunction and changes the overlap between the PdNi Fermi level and the valence band of the CNT. This change causes a large percentage decrease in the current through the semiconducting CNT while a small percentage increase is observed in the metallic CNT current. Raman spectra from the same CNTs were collected and correlated with the conclusions drawn from the electrical characterisation. In addition to demonstrating a new technique for differentiating between metallic and semiconducting CNTs, this work serves as an experimental verification of Raman features that have so far been theoretically assigned to semiconducting and metallic CNTs.

Different metal workfunctions can be modified by exposure to various gases (H_2, O_2, NO_2) and modulation of metal-CNT contacts leads to very interesting research avenues. One choice is to fabricate gas sensors using metal-CNT instead of metal-planar semiconductor contacts. The lack of strong Fermi level pinning in metal-CNT contacts will result in larger responses to workfunction changes, thus increasing sensor sensitivity. A more exotic research theme is in studying the metal-CNT contact properties. In this work, the modulation of PdNi-CNT contacts via Hydrogen exposure was used to differentiate between semiconducting and metallic CNTs. The workfunction change caused by the Hydrogen was relatively small at around 150 mV. Reports in the literature describe materials such as Ytterbium [118] and Vanadium carbide [119] that exhibit significantly larger workfunction changes (≈1 to 1.5 V) on exposure to Oxygen and water vapour. This change is large enough to sweep through the entire CNT bandgap and an electrode of such metals will be able to form ohmic contacts to the CNT valence and conduction bands as well as Schottky barriers with controllable heights. The currents in a CNT contacted with such electrodes should also vary with the overlap between the the metal Fermi level and the CNT density of states and allow a mapping of the CNT band structure using electrical measurement. A "configurable" contact like this will be useful in studying metal-CNT contacts and for applications that require precise contact properties.

Three terminal Carbon nanotube field effect transistors (CNTFETs) with electrodeposited PdNi contacts were fabricated and electrically characterised. The CNTFETs were fabricated by spin coating CNTs dispersed in 1,2-dichlorobenzene and electrodepositing PdNi contacts in patterns defined by photolithography. The low reverse bias current of the PdNi-Si Schottky diodes was used to suppress the current through the leakage path formed by direct PdNi-Si contact. The high workfunctions of Palladium and Nickel result in an ohmic contact to the CNT valence band. The resistance of the transistor at zero gate potential is found to be lower than those using Gold and Titanium as CNT contacts, similar to Pd-semiconducting CNT resistances and higher than reported values of Pd-metallic CNT contacts. The discrepancy in resistances could be due to variations in the PdNi alloy in the neighbourhood of the CNT. The direct PdNi-Si contact makes it impossible to study the transistor characteristics for negative gate-source potentials as the CNT current is obscured by the forward bias current of the PdNi-Si Schottky diode. This problem in the three terminal CNTFETs with electrodeposited contacts can be overcome by fabricating a four terminal device that separates the gate and substrate control. Alternative architectures to fabricate the four terminal CNTFET were discussed.

The next step in analysing CNTFETs formed with electrodeposited contacts would be to fabricate four terminal CNTFETs with independent gate and body terminals. This will allow the PdNi-Si Schottky diodes to be maintained in reverse bias while using the gate voltage to modulate the CNT energy bands and study the CNT as well as PdNi-CNT contact properties. Alternatively, the three terminal CNTFET can be used to study the suitability of electrodeposited PdNi as ferromagnetic contacts in CNT spintronic devices. Ideally, the two electrode dimensions should be different so that they switch magnetisation at different magnetic fields. However, it may be possible to observe magnetoresistance with symmetric contacts because the PdNi domains in direct contact with the two CNT ends may have different switching fields. By examining the electrical characteristics in a varying magnetic field, at low temperatures around 4K and with improved electrical contact between the device contacts and characterisation equipment, the differences between the magnetoresistance of CNTs contacted by electrodeposited PdNi and those contacted by evaporated PdNi can be measured.

BIBLIOGRAPHY

[1] P. C. Andricacos, C. Uzoh, J. O. Dukovic, J. Horkans, and H.; Deligianni. Damascene copper electroplating for chip interconnections. *IBM Journal of Research and Development*, 42:567 – 574, 1998.

[2] Michail E. Kiziroglou, Xiaoli Li, David C. Gonzalez, Cornelis H. de Groot, Alexander A. Zhukov, Peter A. J. de Groot, and Philip N. Bartlett. Orientation and symmetry control of inverse sphere magnetic nanoarrays by guided self-assembly. *Journal of Applied Physics*, 100(11):113720, 2006.

[3] Milan Paunovic and Mordechay Schlesinger. *Fundamentals of Electrochemical deposition.* Wiley Interscience, second edition, 2006.

[4] Mordechay Schlesinger and Milan Paunovic. *Modern Electroplating.* John Wiley and Sons, fourth edition, 2000.

[5] F. A. Lowenheim. *Modern Electroplating.* Wiley, 1974.

[6] S. Nakahara and Y. Okinaka. Microstructure and ductility of electroless Copper deposits. *Acta Metallurgica*, 31(5):713–724, May 1983.

[7] M.L. Sartorelli, A.Q. Schervenski, R.G. Delatorre, P. Klauss, A.M. Maliska, and A.A. Pasa. Cu-Ni Thin Films Electrodeposited on Si: Composition and Current Efficiency. *Physica Status Solidi (a)*, 187(1):91–95, September 2001.

[8] J. Goldstein, D.E. Newbury, D.C. Joy, C.E. Lyman, P. Echlin, E. Lifshin, L. Sawyer, and J.R. Michael. *Scanning Electron Microscopy and X-ray Microanalysis.* Springer, 3rd edition, 2003.

[9] Simon Foner. Versatile and sensitive vibrating-sample magnetometer. *Review of Scientific Instruments*, 30(7):548–557, 1959.

[10] B. E. Conway and J. O'M. Bockris. On the calculation of potential energy profile diagrams for processes in electrolytic metal deposition. *Electrochimica Acta*, 3(4):340–366, January 1961.

[11] Seung-Eun Nam, Sang-Hak Lee, and Kew-Ho Lee. Preparation of a palladium alloy composite membrane supported in a porous stainless steel by vacuum electrodeposition. *Journal of Membrane Science*, 153(2):163–173, February 1999.

[12] Michail E. Kiziroglou, Alexander A. Zhukov, Mamdouh Abdelsalam, Xiaoli Li, Peter A. J. de Groot, Philip N. Bartlett, and Cornelis H. de Groot. Electrodeposition of Ni-Si Schottky Barriers. *IEEE Transactions on Magnetics*, 41(10):2639–2641, October 2005.

[13] Simon M. Sze. *Semiconductor Devices: Physics and Technology.* John Wiley and Sons, second edition, 2001.

[14] J. Crangle and D. Parsons. The magnetization of ferromagnetic binary alloys of cobalt or nickel with elements of the palladium and platinum groups. *Proceedings of the Royal Society of London. Series A, Mathematical and Physical Sciences*, 255(1283):509–519, 1960.

[15] J. Crangle and W. R. Scott. Dilute ferromagnetic alloys. *Journal of Applied Physics*, 36(3):921–928, 1965.

[16] F. Cardarelli. *Materials Handbook: A Concise Desktop Reference, 2nd Edition.* Springer, 2008.

[17] J. Reader and C. H. Corliss. *CRC Handbook of Chemistry and Physics.* CRC Press, 2006.

[18] Michail E. Kiziroglou. *Integration of Spintronics into silicon microelectronics.* PhD thesis, University of Southampton, October 2006.

[19] M Duch, J Esteve, E Gmez, R Prez-Castillejos, and E Valls. Electrodeposited co-ni alloys for mems. *Journal of Micromechanics and Microengineering*, 12(4):400, 2002.

[20] G Schmidt. Concepts for spin injection into semiconductors - a review. *Journal of Physics D: Applied Physics*, 38(7):R107–R122, 2005.

[21] G. Schmidt, D. Ferrand, L. W. Molenkamp, A. T. Filip, and B. J. van Wees. Fundamental obstacle for electrical spin injection from a ferromagnetic metal into a diffusive semiconductor. *Phys. Rev. B*, 62(8):R4790–, August 2000.

[22] Kang Ding, William E. Seyfried, M. K. Tivey, and A. M. Bradley. In situ measurement of dissolved H2 and H2S in high-temperature hydrothermal vent fluids at the Main Endeavour Field, Juan de Fuca Ridge. *Earth and Planetary Science Letters*, 186(3-4):417–425, April 2001.

[23] Cédric Boulart, Matthew C. Mowlem, Douglas P. Connelly, Jean-Pierre Dutasta, and Christopher R. German. A novel, low-cost, high performance dissolved methane sensor for aqueous environments. *Opt. Express*, 16(17):12607–12617, August 2008.

[24] Marielle Lacombe. *Methodes Electrochimiques Pour L'analyse In Situ de Composes Bioactifs en Milieu Oceanique.* PhD thesis, Université de Toulouse, 2007.

[25] Kang Ding, William E. Seyfried, Jr., Zhong Zhang, Margaret K. Tivey, Karen L. Von Damm, and Albert M. Bradley. The in situ ph of hydrothermal fluids at mid-ocean ridges. *Earth and Planetary Science Letters*, 237(1-2):167–174, August 2005.

[26] T B Flanagan and W A Oates. The palladium-hydrogen system. *Annual Review of Materials Science*, 21(1):269–304, 1991.

[27] R. C. Hughes, W. K. Schubert, and R. J. Buss. Solid-State Hydrogen Sensors Using Palladium-Nickel Alloys: Effect of Alloy Composition on Sensor Response. *Journal of The Electrochemical Society*, 142(1):249–254, 1995.

[28] D. H. Everett and P. Nordon. Hysteresis in the palladium + hydrogen system. *Proceedings of the Royal Society of London. Series A, Mathematical and Physical Sciences*, 259(1298):341–360, 1960.

[29] E Wicke and H. Brodowsky. *Hydrogen in Metals II*, volume 29 of *Topics in Applied Physics*, chapter Hydrogen in Palladium and Palladium alloys, pages 73–155. Springer-Verlag, 1978.

[30] J. C. Barton, F. A. Lewis, and Miss I. Woodward. Hysteresis of the relationships between electrical resistance and the Hydrogen content of Palladium. *Transactions of the Faraday Society*, 59:1201 – 1207, 1963.

[31] Y Sakamoto, K Takai, I Takashima, and M Imada. Electrical resistance measurements as a function of composition of palladium - hydrogen(deuterium) systems by a gas phase method. *Journal of Physics: Condensed Matter*, 8(19):3399, 1996.

[32] J. C. Barton, J. A. S. Green, and F. A. Lewis. Changes of electrode potential and electrical resistance as a function of the hydrogen content of some Pd+Ni and Pd+Rh alloys. *Trans. Faraday Soc.*, 62:960 – 970, 1966.

[33] A. W. Carson, F. A. Lewis, and W. H. Schurter. Relationships between the hydrogen content and electrical resistance of palladium + silver alloys. *Trans. Faraday Soc.*, 63:1447–1452, 1967.

[34] Sumio Okuyama, Yuichi Mitobe, Katsuro Okuyama, and Koichi Matsushita. Hydrogen Gas Sensing Using a Pd-Coated Cantilever. *Japanese Journal of Applied Physics*, 39(Part 1, No. 6A):3584–3590, 2000.

[35] Frederic Favier, Erich C. Walter, Michael P. Zach, Thorsten Benter, and Reginald M. Penner. Hydrogen sensors and switches from electrodeposited palladium mesowire arrays. *Science*, 293(5538):2227–2231, 2001.

[36] Kyun Tae Kim, Jun Sim, and Sung Min Cho. Hydrogen gas sensor using Pd nanowires electro-deposited into anodized alumina template. *Sensors Journal, IEEE*, 6(3):509–513, 2006.

[37] Suku Kim, B. S. Kang, F. Ren, K. Ip, Y. W. Heo, D. P. Norton, and S. J. Pearton. Sensitivity of Pt/ZnO Schottky diode characteristics to Hydrogen. *Applied Physics Letters*, 84(10):1698–1700, 2004.

[38] Jihyun Kim, F. Ren, B. P. Gila, C. R. Abernathy, and S. J. Pearton. Reversible barrier height changes in hydrogen-sensitive Pd/GaN and Pt/GaN diodes. *Applied Physics Letters*, 82(5):739–741, 2003.

[39] C. Weichsel, O. Pagni, and A. W. R. Leitch. Electrical and hydrogen sensing characteristics of Pd/ZnO schottky diodes grown on GaAs. *Semiconductor Science and Technology*, 20(8):840–843, 2005.

[40] I. Lundström, S. Shivaraman, C. Svensson, and L. Lundkvist. A Hydrogen - sensitive MOS field - effect transistor. *Applied Physics Letters*, 26(2):55–57, 1975.

[41] Nevin TaşaltIn, Fatih Dumludağ, Mehmet Ali Ebeoğlu, Hayrettin Yüzer, and Zafer Ziya Öztürk. Pd/native nitride/n-GaAs structures as Hydrogen sensors. *Sensors and Actuators B: Chemical*, 130(1):59–64, March 2008.

[42] Xinhua Wang, Xiaoliang Wang, Hongling Xiao, Chun Feng, Xiaoyan Wang, Baozhu Wang, Cuibai Yang, Junxi Wang, Cuimei Wang, Junxue Ran, Guoxin Hu, and Jinmin Li. Hydrogen sensors based on Pt-AlGaN/GaN back-to-back Schottky diode. *physica status solidi (c)*, 5(9):2979–2981, 2008.

[43] Kebaili Corporation. KHS-100 Hydrogen Gas Sensor. Online, March 2011. `http://www.kebaili.com/files/KHS-100A_RevB.pdf`.

[44] Neodym gas detection Systems. Neodym Protisen Hydrogen Sensor. Online, March 2011. `http://www.neodymsystems.com/download/ProtiSen_Datasheet_101.pdf`.

[45] RKI Instruments. RKI Hydrogen Specific Sensor/Transmitter Data sheet. online, March 2011. `http://www.rkiinstruments.com/pdf/H2_Specific.pdf`.

[46] P.F. Ruths, S. Ashok, S.J. Fonash, and J.M. Ruths. A study of pd/si mis schottky barrier diode hydrogen detector. *Electron Devices, IEEE Transactions on*, 28(9):1003–1009, 1981.

[47] M P Anantram and F Leonard. Physics of carbon nanotube electronic devices. *Reports on Progress in Physics*, 69:507561, 2006.

[48] Andreas Thess, Roland Lee, Pavel Nikolaev, Hongjie Dai, Pierre Petit, Jerome Robert, Chunhui Xu, Young Hee Lee, Seong Gon Kim, Andrew G. Rinzler, Daniel T. Colbert, Gustavo E. Scuseria, David Tomanek, John E. Fischer, and Richard E. Smalley. Crystalline ropes of metallic carbon nanotubes. *Science*, 273(5274):483–487, 1996.

[49] Jeffrey L. Bahr, Edward T. Mickelson, Michael J. Bronikowski, Richard E. Smalley, and James M. Tour. Dissolution of small diameter single-wall carbon nanotubes in organic solvents? *Chem. Commun.*, pages 193 – 194, 2001.

[50] Zhenyu Sun, Valeria Nicolosi, David Rickard, Shane D. Bergin, Damian Aherne, and Jonathan N. Coleman. Quantitative evaluation of surfactant-stabilized single-walled carbon nanotubes: Dispersion quality and its correlation with zeta potential. *The Journal of Physical Chemistry C*, 112(29):10692–10699, 2008.

[51] Richa Rastogi, Rahul Kaushal, S.K. Tripathi, Amit L. Sharma, Inderpreet Kaur, and Lalit M. Bharadwaj. Comparative study of carbon nanotube dispersion using surfactants. *Journal of Colloid and Interface Science*, 328(2):421–428, December 2008.

[52] Sumio Iijima. Helical microtubules of graphitic carbon. *Nature*, 354(6348):56–58, November 1991.

[53] Philip G. Collins, Michael S. Arnold, and Phaedon Avouris. Engineering carbon nanotubes and nanotube circuits using electrical breakdown. *Science*, 292(5517):706–709, April 2001.

[54] Philip G. Collins, M. Hersam, M. Arnold, R. Martel, and Ph. Avouris. Current saturation and electrical breakdown in multiwalled carbon nanotubes. *Phys. Rev. Lett.*, 86(14):3128–, April 2001.

[55] T. Guo, P. Nikolaev, A. Thess, D.T. Colbert, and R.E. Smalley. Catalytic growth of single-walled manotubes by laser vaporization. *Chemical Physics Letters*, 243(1-2):49–54, September 1995.

[56] Rainer Weiser, editor. *Nanoelectronics and Information Technology.* Wiley-VCH., 2005.

[57] M. Meyyappan, editor. *Carbon Nanotubes: Science and Applications.* CRC Press, 2005.

[58] Jing Kong, Alan M. Cassell, and Hongjie Dai. Chemical vapor deposition of Methane for single-walled carbon nanotubes. *Chemical Physics Letters*, 292(4-6):567–574, August 1998.

[59] Takashi Inoue, Itaru Gunjishima, and Atsuto Okamoto. Synthesis of diameter-controlled carbon nanotubes using centrifugally classified nanoparticle catalysts. *Carbon*, 45(11):2164–2170, October 2007.

[60] E. F. Kukovitsky, S. G. L'vov, N. A. Sainov, V. A. Shustov, and L. A. Chernozatonskii. Correlation between metal catalyst particle size and carbon nanotube growth. *Chemical Physics Letters*, 355(5-6):497–503, April 2002.

[61] T. Uchino, K. N. Bourdakos, C. H. de Groot, P. Ashburn, M. E. Kiziroglou, G. D. Dilliway, and D. C. Smith. Metal catalyst-free low-temperature carbon nanotube growth on SiGe islands. *Applied Physics Letters*, 86(23):233110, 2005.

[62] B. Q. Wei, R. Vajtai, and P. M. Ajayan. Reliability and current carrying capacity of carbon nanotubes. *Applied Physics Letters*, 79(8):1172–1174, 2001.

[63] F. Kreupl, A. P. Graham, G. S. Duesberg, W. Steinhgl, M. Liebau, E. Unger, and W. Hnlein. Carbon nanotubes in interconnect applications. *Microelectronic Engineering*, 64(1-4):399–408, October 2002.

[64] Quoc Ngo, D. Petranovic, S. Krishnan, A.M. Cassell, Qi Ye, Jun Li, M. Meyyappan, and C.Y. Yang. Electron transport through metal-multiwall carbon nanotube interfaces. *Nanotechnology, IEEE Transactions on*, 3(2):311 – 317, 2004.

[65] C. T. White, D. H. Robertson, and J. W. Mintmire. Helical and rotational symmetries of nanoscale graphitic tubules. *Phys. Rev. B*, 47(9):5485–5488, Mar 1993.

[66] Jeroen W. G. Wilder, Liesbeth C. Venema, Andrew G. Rinzler, Richard E. Smalley, and Cees Dekker. Electronic structure of atomically resolved carbon nanotubes. *Nature*, 391(6662):59–62, January 1998.

[67] P. Avouris. Molecular electronics with carbon nanotubes. *Accounts of Chemical Research*, 35(12):1026–1034, 2002.

[68] Kazuhito Tsukagoshi, Bruce W. Alphenaar, and Hiroki Ago. Coherent transport of electron spin in a ferromagnetically contacted carbon nanotube. *Nature*, 401(6753):572–574, October 1999.

[69] Hyongsok T. Soh, Calvin F. Quate, Alberto F. Morpurgo, Charles M. Marcus, Jing Kong, and Hongjie Dai. Integrated nanotube circuits: Controlled growth and ohmic contacting of single-walled carbon nanotubes. *Applied Physics Letters*, 75(5):627–629, 1999.

[70] E. Joselevich and C.M. Lieber. Vectorial growth of metallic and semiconducting single-wall carbon nanotubes. *Nano Letters*, 2(10):1137–1141, October 2002.

[71] S. Niyogi, C. Hangarter, R.M. Thamankar, Y.-F. Chiang, R. Kawakami, N.V. Myung, and R.C. Haddon. Magnetically assembled multiwalled carbon nanotubes on ferromagnetic contacts. *J. Phys. Chem. B*, 108(51):19818–19824, December 2004.

[72] R. Martel, T. Schmidt, H. R. Shea, T. Hertel, and Ph. Avouris. Single- and multi-wall carbon nanotube field-effect transistors. *Applied Physics Letters*, 73(17):2447–2449, 1998.

[73] Zhihong Chen, Joerg Appenzeller, Joachim Knoch, Yu-ming Lin, and Phaedon Avouris. The role of metal-nanotube contact in the performance of carbon nanotube field-effect transistors. *Nano Letters*, 5(7):1497–1502, 2005.

[74] R. Martel, V. Derycke, C. Lavoie, J. Appenzeller, K. K. Chan, J. Tersoff, and Ph. Avouris. Ambipolar electrical transport in semiconducting single-wall carbon nanotubes. *Phys. Rev. Lett.*, 87(25):256805–, December 2001.

[75] Ali Javey, Jing Guo, Qian Wang, Mark Lundstrom, and Hongjie Dai. Ballistic carbon nanotube field-effect transistors. *Nature*, 424(6949):654–657, August 2003.

[76] D. Mann, A. Javey, J. Kong, Q. Wang, and H. Dai. Ballistic Transport in Metallic Nanotubes with Reliable Pd Ohmic Contacts. *Nano Letters*, 3(11):1541–1544, 2003.

[77] Alwin R. M. Verschueren Sander J. Tans and Cees Dekker. Room-temperature transistor based on a single carbon nanotube. *Nature*, 393:49–52, 1998.

[78] Y. Zhang and Hongjie Dai. Formation of metal nanowires on suspended single-walled carbon nanotubes. *Applied Physics Letters*, 77(19):3015–3017, 2000.

[79] Y. Zhang, Nathan W. Franklin, Robert J. Chen, and Hongjie Dai. Metal coating on suspended carbon nanotubes and its implication to metal-tube interaction. *Chemical Physics Letters*, 331(1):35 – 41, 2000.

[80] Franois Léonard and J. Tersoff. Role of fermi-level pinning in nanotube schottky diodes. *Phys. Rev. Lett.*, 84(20):4693–, May 2000.

[81] J. U. Lee, P. P. Gipp, and C. M. Heller. Carbon nanotube p-n junction diodes. *Applied Physics Letters*, 85(1):145–147, 2004.

[82] Goodhew P. J., Humphreys J., and Beanland R. *Electron Microscopy and Analysis.* Taylor & Francis, 2001.

[83] T. Brintlinger, Yung-Fu Chen, T. Durkop, Enrique Cobas, M. S. Fuhrer, John D. Barry, and John Melngailis. Rapid imaging of nanotubes on insulating substrates. *Applied Physics Letters*, 81(13):2454 –2456, September 2002.

[84] F. Tuinstra and J. L. Koenig. Raman spectrum of graphite. *The Journal of Chemical Physics*, 53(3):1126–1130, 1970.

[85] M. A. Pimenta, G. Dresselhaus, M. S. Dresselhaus, L. G. Cancado, A. Jorio, and R. Saito. Studying disorder in graphite-based systems by raman spectroscopy. *Phys. Chem. Chem. Phys.*, 9:1276–1290, 2007.

[86] A. C. Ferrari, J. C. Meyer, V. Scardaci, C. Casiraghi, M. Lazzeri, F. Mauri, S. Piscanec, D. Jiang, K. S. Novoselov, S. Roth, and A. K. Geim. Raman spectrum of graphene and graphene layers. *Phys. Rev. Lett.*, 97(18):187401, Oct 2006.

[87] R. J. Nemanich and S. A. Solin. First- and second-order raman scattering from finite-size crystals of graphite. *Phys. Rev. B*, 20(2):392–401, Jul 1979.

[88] Jun Yan, Yuanbo Zhang, Philip Kim, and Aron Pinczuk. Electric field effect tuning of electron-phonon coupling in graphene. *Phys. Rev. Lett.*, 98(16):166802, Apr 2007.

[89] M.S. Dresselhaus, G. Dresselhaus, R. Saito, and A. Jorio. Raman spectroscopy of carbon nanotubes. *Physics Reports*, 409:47–99, Mar 2005.

[90] A. Jorio, R. Saito, J. H. Hafner, C. M. Lieber, M. Hunter, T. McClure, G. Dresselhaus, and M. S. Dresselhaus. Structural (n, m) determination of isolated single-wall carbon nanotubes by resonant raman scattering. *Phys. Rev. Lett.*, 86(6):1118–, February 2001.

[91] A. Jorio, G. Dresselhaus, M. S. Dresselhaus, M. Souza, M. S. S. Dantas, M. A. Pimenta, A. M. Rao, R. Saito, C. Liu, and H. M. Cheng. Polarized raman study of single-wall semiconducting carbon nanotubes. *Phys. Rev. Lett.*, 85(12):2617–2620, Sep 2000.

[92] H. Kuzmany, B. Burger, A. Thess, and R.E. Smalley. Vibrational spectra of single wall carbon nanotubes. *Carbon*, 36(5-6):709 – 712, 1998. European Materials Research Society 1997 Meeting, Symposium A: Fullernes and Carbon based Materials.

[93] S. D. M. Brown, A. Jorio, P. Corio, M. S. Dresselhaus, G. Dresselhaus, R. Saito, and K. Kneipp. Origin of the breit-wigner-fano lineshape of the tangential g-band feature of metallic carbon nanotubes. *Phys. Rev. B*, 63(15):155414, Mar 2001.

[94] A. Jorio, A. G. Souza Filho, G. Dresselhaus, M. S. Dresselhaus, A. K. Swan, M. S. nl, B. B. Goldberg, M. A. Pimenta, J. H. Hafner, C. M. Lieber, and R. Saito. G-band

resonant raman study of 62 isolated single-wall carbon nanotubes. *Phys. Rev. B*, 65(15):155412–, March 2002.

[95] M. S. Dresselhaus, A. Jorio, A. G. Souza Filho, G. Dresselhaus, and R. Saito. Raman spectroscopy on one isolated carbon nanotube. *Physica B: Condensed Matter*, 323(1-4):15–20, October 2002.

[96] Satoru Suzuki, Yoshio Watanabe, Yoshikazu Homma, Shin ya Fukuba, Stefan Heun, and Andrea Locatelli. Work functions of individual single-walled carbon nanotubes. *Applied Physics Letters*, 85(1):127–129, 2004.

[97] Masashi Shiraishi and Masafumi Ata. Work function of carbon nanotubes. *Carbon*, 39(12):1913–1917, October 2001.

[98] V. Derycke, R. Martel, J. Appenzeller, and Ph. Avouris. Carbon nanotube inter- and intramolecular logic gates. *Nano Letters*, 1(9):453–456, 2001.

[99] V. Derycke, R. Martel, J. Appenzeller, and Ph. Avouris. Controlling doping and carrier injection in carbon nanotube transistors. *Applied Physics Letters*, 80(15):2773–2775, 2002.

[100] S. J. Wind, J. Appenzeller, R. Martel, V. Derycke, and Ph. Avouris. Vertical scaling of carbon nanotube field-effect transistors using top gate electrodes. *Applied Physics Letters*, 80(20):3817–3819, 2002.

[101] J. Appenzeller, J. Knoch, V. Derycke, R. Martel, S. Wind, and Ph. Avouris. Field-modulated carrier transport in carbon nanotube transistors. *Phys. Rev. Lett.*, 89(12):126801, Aug 2002.

[102] Adrian Bachtold, Peter Hadley, Takeshi Nakanishi, and Cees Dekker. Logic circuits with carbon nanotube transistors. *Science*, 294(5545):1317–1320, November 2001.

[103] Erhan Yenilmez Chongwu Zhou, Jing Kong and Hongjie Dai. Modulated chemical doping of individual carbon nanotubes. *Science*, 290:1152–1555, 2000.

[104] Marc Bockrath, J. Hone, A. Zettl, Paul L. McEuen, Andrew G. Rinzler, and Richard E. Smalley. Chemical doping of individual semiconducting carbon-nanotube ropes. *Phys. Rev. B*, 61(16):R10606–, April 2000.

[105] W. J. M. Naber, S. Faez, and W. G. van der Wiel. Organic spintronics. *Journal Of Physics D-Applied Physics*, 40(12):R205–R228, June 2007.

[106] Luis E. Hueso, Jose M. Pruneda, Valeria Ferrari, Gavin Burnell, Jose P. Valdes-Herrera, Benjamin D. Simons, Peter B. Littlewood, Emilio Artacho, Albert Fert, and Neil D. Mathur. Transformation of spin information into large electrical signals using carbon nanotubes. *Nature*, 445(7126):410–413, January 2007.

[107] Supriyo Datta and Biswajit Das. Electronic analog of the electro-optic modulator. *Applied Physics Letters*, 56(7):665–667, 1990.

[108] S. O. Valenzuela and M. Tinkham. Direct electronic measurement of the spin hall effect. *Nature*, 442:176–179, 2006.

[109] N. Poli M. Urech, V. Korenivski and D. B. Haviland. Direct demonstration of decoupling of spin and charge currents in nanostructures. *Nano Letters*, 4:871–874, 2006.

[110] N. Tombros, S. J. van der Molen, and B. J. van Wees. Separating spin and charge transport in single-wall carbon nanotubes. *Physical Review B*, 73(23):233403, June 2006.

[111] A. Cottet, T. Kontos, S. Sahoo, H. T. Man, M. S. Choi, W. Belzig, C. Bruder, A. F. Morpurgo, and C. Schonenberger. Nanospintronics with carbon nanotubes. *Semiconductor Science And Technology*, 21(11):S78–S95, November 2006.

[112] Ane Jensen, Jonas R. Hauptmann, Jesper Nygård, and Poul Erik Lindelof. Magnetoresistance in ferromagnetically contacted single-wall carbon nanotubes. *Physical Review B (Condensed Matter and Materials Physics)*, 72(3):035419, 2005.

[113] B. Nagabhirava, T. Bansal, G. U. Sumanasekera, B. W. Alphenaar, and L. Liu. Gated spin transport through an individual single wall carbon nanotube. *Applied Physics Letters*, 88(2):023503, 2006.

[114] C. Schönenberger S. Sahoo, T. Kontos and C. Sürgers. Electrical spin injection in multiwall carbon nanotubes with transparent ferromagnetic contacts. *Applied Physics Letters.*, 86:112109, 2005.

[115] H. T. Man, I. J. W. Wever, and A. F. Morpurgo. Spin-dependent quantum interference in single-wall carbon nanotubes with ferromagnetic contacts. *Physical Review B (Condensed Matter and Materials Physics)*, 73(24):241401, 2006.

[116] Ki Kang Kim, Dong Jae Bae, Cheol-Min Yang, Kay Hyeok An, Ji Yeong Lee, and Young Hee Lee. Nanodispersion of single-walled carbon nanotubes using dichloroethane. *Journal of Nanoscience and Nanotechnology*, 5:10551059, 2005.

[117] Sangeeta Sahoo, Takis Kontos, Jurg Furer, Christian Hoffmann, Matthias Graber, Audrey Cottet, and Christian Schönenberger. Electric field control of spin transport. *Nat Phys*, 1(2):99–102, November 2005.

[118] G. Strasser, E. Bertel, and F. P. Netzer. Surface reactions on rare earth metals monitored by work function measurements. *Journal of Catalysis*, 79(2):420–430, February 1983.

[119] P. A. P. Lindberg and L. I. Johansson. Work function and reactivity of some crystal faces of substoichiometric transition-metal carbides. *Surface Science*, 194(1-2):199–204, 1988.